Interaction and confinement in nanostructures: Spin-orbit coupling and electron-phonon scattering

Dissertation
zur Erlangung des Doktorgrades
des Fachbereichs Physik
der Universität Hamburg

vorgelegt von
Stefan Debald
aus Münster

Hamburg
2005

Gutachter der Dissertation:	Prof. Dr. B. Kramer PD Dr. T. Brandes
Gutachter der Disputation:	Prof. Dr. B. Kramer Prof. Dr. G. Platero
Datum der Disputation:	01.04.2005
Vorsitzender des Prüfungsausschusses:	PD Dr. S. Kettemann
Vorsitzender des Promotionsausschusses:	Prof. Dr. G. Huber
Dekan des Fachbereichs Physik:	Prof. Dr. G. Huber

Abstract

It is the purpose of this work to study the interplay of interaction and confinement in nanostructures using two examples.

In part I, we investigate the effects of spin-orbit interaction in parabolically confined ballistic quantum wires and few-electron quantum dots. In general, spin-orbit interaction couples the spin of a particle to its orbital motion. In nanostructures, the latter can easily be manipulated by means of confining potentials. In the first part for this work, we answer the question how the spatial confinement influences spectral and spin properties of electrons in nanostructures with substantial spin-orbit coupling. The latter is assumed to originate from the structure inversion asymmetry at an interface. Thus, the spin-orbit interaction is given by the Rashba model.

For a quantum wire, we show that one-electron spectral and spin properties are governed by a combined spin orbital-parity symmetry of wire. The breaking of this spin parity by a perpendicular magnetic field leads to the emergence of a significant energy splitting at $k = 0$ and hybridisation effects in the spin density. Both effects are expected to be experimentally accessible by means of optical or transport measurements. In general, the spin-orbit induced modifications of the subband structure are very sensitive to weak magnetic fields. Because of magnetic stray fields, this implies several consequences for future spintronic devices, which depend on ferromagnetic leads.

For the spin-orbit interaction in a quantum dot, we derive a model, inspired by an analogy with quantum optics. This model illuminates most clearly the dominant features of spin-orbit coupling in quantum dots. The model is used to discuss an experiment for observing coherent oscillations in a single quantum dot with the oscillations driven by spin-orbit coupling. The oscillating degree of freedom represents a novel, composite spin-angular momentum qubit.

In part II, the interplay of mechanical confinement and electron-phonon interaction is investigated in the transport through two coupled quantum dots. Phonons are quantised modes of lattice vibration. Geometrical confinement in nanomechanical resonators strongly alters the properties of the phonon system. We study a free-standing quantum well as a model for a nano-size planar phonon cavity. We show that coupled quantum dots are a promising tool to detect phonon quantum size effects in the electron transport. For particular values of the dot level splitting Δ, piezo-electric or deformation potential scattering is either drastically reduced as compared to the bulk case, or strongly enhanced due to van–Hove singularities in the phonon density of states. By tuning Δ via gate voltages, one can either control dephasing in double quantum dot qubit systems, or strongly increase emission of phonon modes with characteristic angular distributions.

Zusammenfassung

In dieser Arbeit betrachten wir das Zusammenspiel von Wechselwirkung und räumlicher Beschränkung anhand von zwei Beispielen.

In Teil I untersuchen wir Effekte der Spin-Bahn-Wechselwirkung in ballistischen Quantendrähten und Quantenpunkten. Die Spin-Bahn-Wechselwirkung koppelt den Spinfreiheitgrad eines Teilchens an seine orbitale Bewegung, die sich in Nanostrukturen leicht durch beschränkende Potentiale beeinflussen lässt. Im ersten Teil dieser Arbeit betrachten wir, wie die spektralen und Spineigenschaften in Systemen mit substantieller Spin-Bahn-Wechselwirkung von der räumlichen Beschränkung beeinflusst werden. Wir nehmen an, dass die Spin-Bahn-Wechselwirkung durch die Raumspiegelungsasymmetrie in einer Inversionsschicht bestimmt wird und beschreiben sie daher durch das Rashba Modell.

Wir zeigen, dass in einem Quantendraht die spektralen und Spineigenschaften eines Elektrons durch eine kombinierte Spin-Raumparitätssymmetrie bestimmt werden. Das Aufheben dieser Symmetrie durch ein senkrechtes Magnetfeld führt zu einer ausgeprägten Energieaufspaltung bei $k = 0$ und Hybridisierungseffekten in der Spindichte. Es ist zu erwarten, dass beide Effekte für optische oder Transportexperimente zugänglich sind. Die von der Spin-Bahn-Wechselwirkung stammenden Modifikationen der Subbandstruktur sind sehr empfindlich gegenüber schwachen Magnetfeldern. Dies hat Konsequenzen für zukünftigen Spintronikbauteile, die von ferromagnetischen Zuleitungen abhängen (Streufelder).

Inspiriert von einer Analogie zur Quantenoptik, leiten wir am Beipiel des Quantenpunkts ein effektives Modell her, das die Hauptmerkmale der Spin-Bahn-Wechselwirkung in Quantenpunkten verdeutlicht. In diesem Modell diskutieren wir ein Experiment zur Beobachtung von spinbahngetriebenen kohärenten Oszillationen in einem einzelnen Quantenpunkt. Der oszillierende Freiheitsgrad stellt ein neues Qubit dar, das sich aus Spin und Drehimpuls zusammensetzt.

In Teil II untersuchen wir das Zusammenspiel von mechanischer Beschränkung und Elektron-Phonon-Wechselwirkung im Transport durch zwei gekoppelte Quantenpunkte. Phononen sind quantisierte Gitterschwingungen deren Eigenschaften stark von der Beschränkung in nanomechanischen Resonatoren beeinflusst werden. Am Beispiel einer ebenen Phononenkavität zeigen wir, dass gekoppelte Quantenpunkte einen vielversprechenden Detektor zum Nachweis von Phonon-„quantum-size“-Effekten im elektronischen Transport darstellen. Für gewisse Werte des Energieabstands Δ der Quantenpunkte wird die Streuung durch das piezoelektrische oder Deformationspotential entweder drastisch unterdrückt oder durch van–Hove Singularitäten in der Zustandsdichte der Phononen enorm verstärkt. Die Änderung von Δ ermöglicht es daher, Kontrolle über die Dephasierung in Doppelquantenpunkt-basierten Qubit-Systemen zu erlangen, oder die Emission in Phononmoden mit charakteristischer Winkelverteilung zu verstärken.

Publications

Some of the main results of this work have been published in the following articles

1. S. Debald and C. Emary, *Spin-orbit driven coherent oscillations in a few-electron quantum dot*, (submitted). E-print: cond-mat/0410714.

2. S. Debald and B. Kramer, *Rashba effect and magnetic field in semiconductor quantum wires*, to appear in Phys. Rev. B **71** (2005). E-print: cond-mat/0411444.

3. S. Debald, T. Brandes, and B. Kramer, *Nonlinear electron transport through double quantum dots coupled to confined phonons*, Int. Journal of Modern Physics B **17**, 5471 (2003).

4. S. Debald, T. Brandes, and B. Kramer, *Control of dephasing and phonon emission in coupled quantum dots*, Rapid Communication in Phys. Rev. B **66**, 041301(R) (2002). (This work has been selected for the 15th July 2002 issue of the Virtual Journal of Nanoscale Science & Technology.)

5. T. Vorrath, S. Debald, B. Kramer, and T. Brandes, *Phonon cavity models for quantum dot based qubits*, Proc. 26th Int. Conf. Semicond., Edinburgh (2002).

6. S. Debald, T. Vorrath, T. Brandes, and B. Kramer, *Phonons and phonon confinement in transport through double quantum dots*, Proc. 25th Int. Conf. Semicond., Osaka (2000).

Table of Contents

Introduction

With the immense technological progress in the field of nanoprocessing in the last two decades, it is feasible to fabricate high-precision nanostructured electronic devices in semiconductors. In such artificial structures, the length scales of the system may become comparable or even smaller than the dephasing distance. The latter is the average length an electron can propagate before its quantum mechanical phase becomes destroyed by some process. Therefore, the quantum mechanical behaviour of the electrons manifests itself in striking quantum interference phenomena in the properties of the nanostructures. Examples are the weak localisation quantum corrections to the conductance of disordered films [1] and the Aharonov–Bohm oscillations in the magneto-transport of tiny ring structures [2].

In addition, in clean samples electrons can propagate large distances without being scattered at imperfections. In GaAs/GaAlAs semiconductor heterostructures, a mean free path (average distance between successive scattering events) of several μm can be reached at low temperatures [3]. Thus, in such nanostructures, electron propagation is often well described in a ballistic picture. A prominent example for ballistic transport in nanostructures is the quantisation of conductance through small constrictions (quantum point contacts) [4, 5].

Recently, the observation of coherent oscillations in the time evolution of a quantum state in a Josephson junction [6] or coupled semiconductor quantum dots [7] has been achieved. These oscillations – the back and forth flopping between two states in a quantum mechanical superposition – directly show quantum mechanics at work. The observation of coherent oscillations in solid-state systems represents the frontier in our ability to control nature at a microscopic level. This effort goes hand-in-hand with the search for workable quantum bits (qubits) and dream of quantum computation.

The above examples are well described in an effective single-particle model which treats the electrons (or Cooper pairs as in case of the Josephson junction) as non-interacting particles. However, this picture has some limitations. For instance, the coherent oscillations can only be traced for times smaller than the dephasing time. In general, the quantum phase of an electron will be randomised by inelastic scattering events with e.g. other electrons or with lattice vibrations

(phonons). Therefore, the electron-electron (e-e) and electron-phonon (e-p) interactions set the limit for the observation of coherent phenomena in nanostructures at low temperatures. On the other hand, the e-e interaction itself causes profound effects like collective excitations of electrons, which in the parlance of many body physics are called plasmons. The importance of e-e interaction is determined by the electron density. In nanostructures the latter can be tuned by means of gates voltages which may draw electrons from or to the system. With increasing electron concentration the average kinetic energy is expected to become larger than the average interaction energy. In this regime, many body effects can be neglected and the electron is approximately a freely moving particle in an averaged background potential caused by the other electrons. It is this approximation that we shall apply throughout this work.

Similar to the phase information of a particle, the nature of its spin degree of freedom is purely quantum mechanical. The fundamental issue of the influence of the spin in electron transport has been a driving force in the field of magnetoelectronics in the last decades [8]. The quantum nature of spin makes it inaccessible to many of the dominating forces in a solid. Recently, this non-volatility of spin has considerably sparked interest in the emerging field of *spintronics* [9], which is an amalgamation of different areas in physics (electronics, photonics, and magnetics). Being motivated by fundamental and applicational interests, the paradigm of spintronics is either to add the spin degree of freedom to conventional charge-based electronic devices, or to use the spin alone, aiming at the advantages of its non-volatility. Such devices are expected to have an increased data processing speed and integration density, and a decreased power consumption compared to conventional semiconductor devices. From a very basic point of view, manipulating the spin requires it to be distinguishable. This implies that the spin degeneracy has to be lifted. Simple reasoning shows that single-particle states of electrons in a solid are two-fold spin degenerate if time-reversal and space-inversion symmetry are simultaneously present. Thus, there are two generic ways to address the spin: (i) Lift spin degeneracy by breaking time-reversal symmetry by e.g. magnetic fields (external or internal as in the case of ferromagnets). This corresponds to the magneto-electronic aspect of spintronics which has led to e.g. the discovery of the giant magnetoresistance (GMR) effect in 1988 [10] that is already employed in present-day hard disk drives. (ii) Lift spin degeneracy by breaking space-inversion symmetry. In semiconductor nanostructures this leads to the issue of spin-orbit coupling.

The relativistic coupling of spin and orbital motion is well known from atomic physics in the context of fine-structure corrections to the spectrum of the hydrogen atom. There, the effect of spin-orbit coupling can be estimated by the Sommerfeld fine-structure constant $\alpha_{\mathrm{FS}} \approx 1/137$ as $H_{\mathrm{SO}}/H_0 \approx \alpha_{\mathrm{FS}}^2$, being clearly a small perturbation. On the contrary, in semiconductor nanostructures, the strength of

spin-orbit coupling depends on the strong electric field which confines the motion of electrons to a plane. This is known as the *Rashba effect* [11, 12]. The application of additional external electric fields enables one to modify the strength of spin-orbit coupling, thus providing a "control knob" with which the Rashba effect can be tuned continuously from being almost zero to a regime where $H_{\mathrm{SO}}/H_0 \sim 1$. In contrast to e-e and e-p interactions, which couple two distinct (quasi-)particles, the spin-orbit coupling is an effective interaction which couples two degrees of freedom (spin and orbits) of the same particle.

Both spin-orbit coupling, and e-e interaction, serve as examples to demonstrate that interactions can be tuned in nanostructures. Moreover, the geometric definition of the device (surfaces, contacts, barriers, interfaces), which we summarise with the notion *confinement* in the following, can also be influenced by means of external gate voltages and the associated repulsive or attractive electrostatic potentials. For instance, gate voltages were used to set the width of the constriction of the quantum point contact or the diameter of the coupled quantum dots in the abovementioned experiments. Confinement has a major impact on wavefunctions and energies. It is the possibility to modify the strengths of interactions and confinement which makes the nanostructure an excellent tool to investigate effects which arise from their interplay.

In this work we study effects of interaction and confinement in two examples. In part I, we discuss the interplay of Rashba spin-orbit coupling in ballistic low-dimensional electron systems. In general, spin-orbit interaction connects the spin degree of freedom with the orbital motion of the electron. Since the latter is very sensitive to confinement, the questions arises how the interplay of spin-orbit coupling and confinement modifies the spectral and spin properties of electrons in the nanostructure. Following common experimental setups, we also include a magnetic field as a further physical quantity which separately influences the orbital motion (cyclotron orbits) and the spin (Zeeman effect). In chapter 1, we give an introduction to the Rashba effect as the dominant source of spin-orbit coupling in a certain class of semiconductor nanostructures. In chapter 2, we discuss the interplay of spin-orbit coupling, geometrical confinement, and magnetic field in quasi-one-dimensional quantum wires. In such systems, the electron is confined in two spatial directions and can only propagate freely in one direction. We show that spectral and spin properties carry signatures of spin-orbit coupling which should be experimentally accessible by means of optical or transport measurements. In chapter 3, we further reduce the dimension of the electron system by addressing the effects of spin-orbit coupling in quasi-zero-dimensional quantum dots. We derive an effective analytical model which describes the dominant influence of spin-orbit coupling on the one-electron spectral and spin properties. In addition, we propose an experiment for the observation of spin-orbit driven coherent oscillations in a single few-electron quantum dot. Here, the oscillating degree of

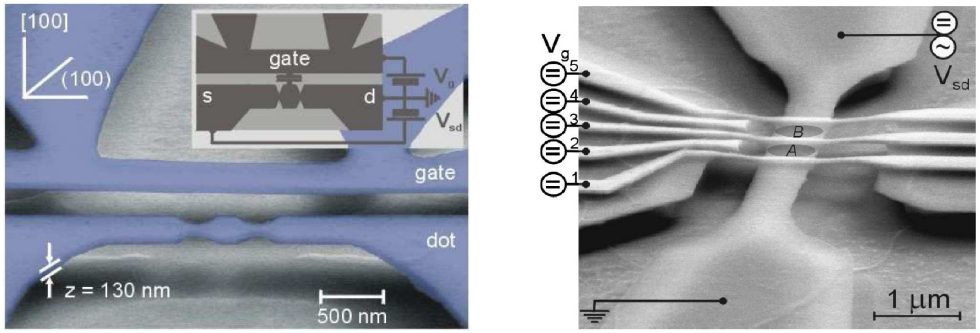

Figure 1: Scanning electron micrographs of nanoelectromechanical systems. Left: a suspended quantum dot cavity and Hall-bar formed in a 130 nm thin GaAs/GaAlAs membrane. Right: a 4 μm long, 130 nm thick free-standing beam that contains a fully tuneable low-dimensional electron system. Five equally suspended Au electrodes can be used to operate the device as two-dimensional electron gas, quantum point contact, single or double dot. Taken from [15] by kind permission of E. Weig.

freedom can be understood as a novel compound spin angular-momentum qubit.

In part II, we consider a further qubit candidate, the two-level system which is built by two coupled quantum dots. In such a device, even at zero temperatures, the dephasing time is limited by the e-p interaction via coupling to low-energy phonons as bosonic excitations of the environment. In chapter 5, we give an introduction to e-p interaction. Since phonons are quantised lattice vibrations, the acousto-mechanical properties of the nanostructure are expected to influence the e-p interaction. Recently, the fabrication of nanomechanical semiconductor resonators (tiny, freely suspended membranes, bars and strings) which contain a layer of conducting electrons was achieved [13] (see also Fig. 1). The vibrational properties of these nanostructures differ drastically from bulk material. For instance, the phonon spectrum is split into several subbands, leading to quantisation effects of e.g. the thermal conductance [14]. In chapter 6, we study the effects of phonon confinement on the electron transport through two coupled quantum dots. We show that typical peculiarities of confined phonon systems, like van–Hove singularities in the phonon density of states, manifest themselves in the non-linear electron transport, acting as clear fingerprints of phonon confinement. In addition, the confinement is shown to be an excellent tool to control phonon induced decoherence in double quantum dots. We demonstrate that the use of "phonon cavities" enables one to either strongly suppress or drastically enhance phonon induced dissipation in such systems.

Part I

Spin-orbit coupling in nanostructures

Chapter 1

The Rashba effect

Effects of spin-orbit (SO) interaction are well-known from atomic physics. The relativistic nature of this coupling can be understood by a low-velocity approximation to the Dirac equation [16]. This approach yields, among other fine-structure corrections to the non-relativistic Schrödinger equation, the Pauli SO term

$$H_{\mathrm{SO}} = -\frac{\hbar}{4m_0^2c^2}\boldsymbol{\sigma}\cdot\big(\mathbf{p}\times\boldsymbol{\nabla}V(\mathbf{r})\big), \tag{1.1}$$

where $\hbar$ is Planck's constant, m_0 the bare mass of the electron, c the velocity of light, and $\boldsymbol{\sigma}$ the vector of Pauli matrices. $V(\mathbf{r})$ is the electrostatic potential in which the electron propagates with momentum $\mathbf{p}$. In atomic physics $V(\mathbf{r})$ is the Coulomb potential of the atomic core.

In semiconductor physics, the spectral properties of electrons which move in a periodic crystal are characterised by energy bands $E_n(\mathbf{k})$. Here also, effects of SO coupling emerge in the band structure. A prominent example is the energy splitting of the topmost valence band in GaAs. This splitting can be determined up to high precision in band structure calculations [17, 18]. The microscopic origin of the energy splitting in such calculations is again given by Eq. (1.1).

In the following, we consider the effects of SO coupling in two-dimensional (2D) electron systems such as quantum wells (QWs) which can be tailored experimentally e.g. in semiconductor heterostructures [3]. Strong confining potentials at the interface of the heterostructure result in quantised energy levels of the electron for one spatial direction whereas it is free to move in the other two spatial directions [19]. Here, we focus on the introduction of the Rashba effect [11, 12] as a model for the dominating SO coupling in a certain class of 2D systems. We will need this model in the subsequent chapters to understand SO effects in electron systems with further reduced dimension (quasi-one-dimensional 'quantum wires' in chapter 1 and quasi-zero-dimensional 'quantum dots' in chapter 2).

An extensive and detailed analysis of SO coupling effects in 2D electron and hole systems can be found in the monograph by Winkler [18].

1.1 Spin-orbit coupling in two-dimensional electron systems

The spin degeneracy of electron states in a solid stems from the simultaneous effect of time-reversal and space-inversion symmetry [20]. The latter requires $E_+(\mathbf{k}) = E_+(-\mathbf{k})$ while the first symmetry operation inverts both propagation direction and spin, leading to Kramer's degeneracy $E_+(\mathbf{k}) = E_-(-\mathbf{k})$. Here, the index $\pm$ denotes the spin state for a given quantisation axis. The combined effect of both symmetries yields the spin degeneracy of single-particle energies, $E_+(\mathbf{k}) = E_-(\mathbf{k})$. Thus, a magnetic field which removes time-reversal symmetry, or any potential that breaks space-inversion symmetry may lift spin degeneracy.

In semiconductors with zinc blende crystal structure (e.g. GaAs, InAs) which lacks a centre of space inversion, the corresponding crystal field leads to a *bulk inversion asymmetry* (BIA). Furthermore, in 2D QWs and heterostructures, the potential which confines the electron in one spatial direction may lead to a *structure inversion asymmetry* (SIA). The effect of such asymmetric potentials on the electron spin is again given by the Pauli term (1.1) and was calculated in two classic papers by Dresselhaus [21] (BIA) and Bychkov & Rashba [11, 12] (SIA). The relative importance of BIA and SIA in a system varies depending on the band structure of the material, the electron density, and the actual geometry of the sample under investigation [18]. The conceptual difference between the two terms is that the BIA is essentially fixed for a given sample while the SIA term does depend on macroscopic voltages and hence can be changed for instance by external gates (see next section).

A quantitative comparison of the SO effects induced by the two sources of inversion asymmetry shows that BIA usually dominates in GaAs while in InAs SIA typically prevails [18]. In the following, we restrict ourselves to InAs based 2D systems which justifies the neglect of BIA contributions to the SO coupling. As a model for the SO coupling in such systems we introduce the Rashba model in the subsequent section.

1.2 The model

The Pauli term (1.1) connects spin and orbital motion depending on the electric field that acts on the electron. In a quantum well this field may contain contributions from built-in or external potentials, as well as the effective potential from

the position-dependent band edges of the heterostructure. We assume that the confinement potential which defines the 2D electron system shall vary in the z-direction only, $V(\mathbf{r}) \approx V_0 + eE_z z$. The SO coupling that arises from SIA then can be written in lowest order in momentum and electric field E_z as [11, 12]

$$H_{\mathrm{SO}} = -\frac{\alpha}{\hbar}(\mathbf{p} \times \boldsymbol{\sigma})_z , \tag{1.2}$$

with the parameter α being proportional to E_z. This term is often referred to as the *Rashba effect*, although the actual effect of Eq. (1.2) is the lifting of the spin degeneracy as we shall see in Sec. 1.3.

In the following two chapters of this thesis, we describe ballistic SO-interacting nanostructures in the effective mass approximation [22]. We assume that such electron systems are defined in the lowest 2D subband by means of further confining potentials V_c,

$$H = \frac{1}{2m}\left(p_x^2 + p_y^2\right) + V_c(x,y) - \frac{\alpha}{\hbar}(p_x\sigma_y - p_y\sigma_x) . \tag{1.3}$$

An introduction to the calculation of the effective mass m and the strength of the Rashba SO coupling α from the band structure can be found in Ref. [18]. Here, we understand Eq. (1.3) as an effective model with phenomenological constants m and α that are to be determined by experiment. The effective mass approximation is well established for a single band description of clean 2D systems [3]. Chen and Raikh [23] showed that exchange-correlation effects may lead to an enhancement of the Rashba SO coupling. However, for typical electron densities in InAs 2D systems such many body corrections are negligible [18].

Since α depends on the electric field which confines the electron in 2D, it is possible to modify the strength of the Rashba effect by applying external gate voltages. This was first demonstrated experimentally by Nitta *et al.* [24] who placed a gate on top of an $In_{0.53}Ga_{0.47}As$ sample and tuned continuously the α parameter by a factor of 2. In a more recent work Koga *et al.* even altered α up to a factor of 5 in one sample [25]. Papadakis *et al.* [26] and Grundler [27] have shown that by putting a front and a back gate on the sample, the Rashba effect can be changed continuously while keeping the electron density and thus a residual BIA contribution to the SO coupling constant.

By setting $V_c \equiv 0$ in Eq. (1.3), the main effect of the Rashba model in 2D can be seen from the eigenenergies and eigenstates [12, 18],

$$E_\pm(\mathbf{k}) = \frac{\hbar^2}{2m}k^2 \pm \alpha k, \tag{1.4}$$

$$|\psi_\pm\rangle = e^{i\mathbf{k}\cdot\mathbf{r}} \begin{pmatrix} 1 \\ \mp i e^{i\varphi} \end{pmatrix}, \tag{1.5}$$

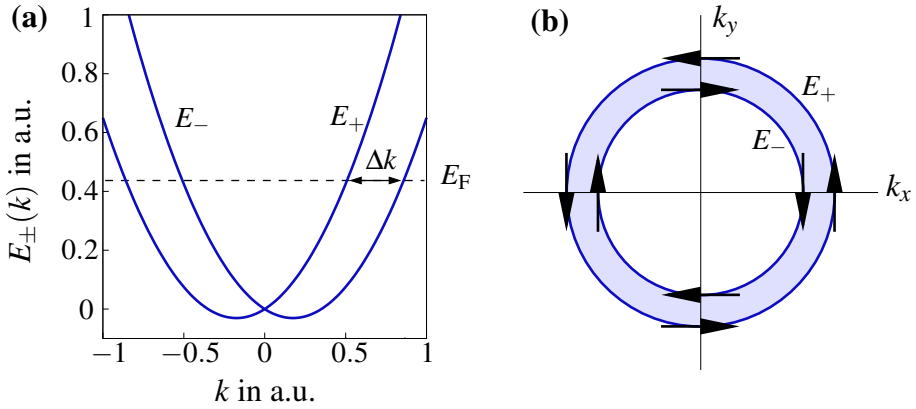

Figure 1.1: Effect of Rashba spin-orbit coupling on dispersion (a) and spin (b).

where $\mathbf{k} = k(\cos\varphi, \sin\varphi, 0)$. The dispersion (1.4) consists of two branches which are non-degenerate for $k > 0$, see Fig. 1.1a. The spin state of the electron which follows from Eq. (1.5) is given by $\langle \boldsymbol{\sigma} \rangle = \pm(\sin\varphi, -\cos\varphi, 0)$ and is shown in Fig. 1.1b. These profound effects of Rashba SO coupling can be understood by rewriting Eq. (1.2) as the Zeeman effect of a momentum dependent effective magnetic field $\mathbf{B}_{\mathrm{SO}}(\mathbf{p}) \cdot \boldsymbol{\sigma}$. The amplitude of $\mathbf{B}_{\mathrm{SO}}$ is proportional to the momentum while its orientation in the 2D plane is orthogonal to the direction of propagation. Thus, for fixed propagation direction, the spin is quantised perpendicular to $\mathbf{p}$, see Fig. 1.1b. This shows that there is no common axis of spin quantisation in 2D with Rashba SO coupling. Thus, the subscript $\pm$ only corresponds to a spin frame which is local in k space.

In experiment, the coupling parameter α is commonly determined by Shubnikov–de Haas (SdH) measurements [28] or weak antilocalisation analysis [1, 29] in weak magnetic fields. In 2D, the frequency of SdH oscillations in the magnetotransport is proportional to the electron density in the system [3]. If the spin degeneracy is broken by Rashba SO coupling the two branches of the dispersion (1.4) have different wave vectors at a given Fermi energy

$$E_{\mathrm{F}} = \frac{\hbar^2}{2m} k_{\mathrm{F}\pm}^2 \pm \alpha k_{\mathrm{F}\pm}. \tag{1.6}$$

As a consequence, the difference in Fermi wave vector is proportional to the strength of SO coupling, $\Delta k = |k_{\mathrm{F}+} - k_{\mathrm{F}-}| = 2m\alpha/\hbar^2$. The electron density depends parabolically on the Fermi wave vector in 2D. Thus, SO coupling leads to different electron populations $N_\pm \propto k_{\mathrm{F}\pm}^2$ of the two branches $E_\pm(k)$. In the context of SdH measurements, this leads to two different frequencies which result in a beating pattern in the SdH oscillations, see e.g. [30]. From the analysis of the beating frequency, the strength of SO coupling α can be determined [18]. We remark that beating patterns in magneto-oscillations are not restricted to the Rashba

effect. Any effect which leads to a $B = 0$ spin splitting (like BIA) may also result in a beating pattern.

1.3 Rashba effect in a perpendicular magnetic field

In the following, we present the effect of an additional perpendicular magnetic field which is a common tool to introduce a tuneable energy scale, i.e. the cyclotron energy $\hbar\omega_c = \hbar eB/mc$. In addition to this energy scale, which finally leads to the quantisation of the system into Landau levels, the Zeeman effect is also expected to alter the spin state of the electrons.

This system serves as an example for the interplay of the Rashba effect with a further energy scale. Furthermore, it shows an illustrative analogy to a quantum optical model which will be useful in the following chapters of the thesis when dealing with non-integrable models.

We extend the Hamiltonian (1.3) of the previous section by including a perpendicular magnetic field ($\mathbf{B} = B\,\hat{\mathbf{e}}_z$),

$$H = H_0 + H_{\mathrm{SO}}, \tag{1.7}$$

$$H_0 = \frac{1}{2m}\left(\mathbf{p} + \frac{e}{c}\mathbf{A}\right)^2 + \frac{1}{2}g\mu_{\mathrm{B}}B\sigma_z, \tag{1.8}$$

$$H_{\mathrm{SO}} = -\frac{\alpha}{\hbar}\left[\left(\mathbf{p} + \frac{e}{c}\mathbf{A}\right) \times \boldsymbol{\sigma}\right]_z, \quad \mathbf{p} = (p_x, p_y). \tag{1.9}$$

We follow the standard derivation of quantised Landau levels in symmetric gauge $\mathbf{A} = (-y, x)B/2$, by defining

$$x_\pm = \frac{1}{\sqrt{2}}(y \pm ix), \quad p_\pm = \frac{1}{\sqrt{2}}(p_y \mp ip_x), \tag{1.10}$$

and creation and annihilation operators

$$a = \frac{1}{\sqrt{\hbar m\omega_c}}\left(p_- - \frac{i}{2}m\omega_c x_+\right), \quad a^\dagger = \frac{1}{\sqrt{\hbar m\omega_c}}\left(p_+ + \frac{i}{2}m\omega_c x_-\right), \tag{1.11}$$

leading to the representation in terms of Landau levels,

$$\frac{H_0}{\hbar\omega_c} = \left(a^\dagger a + \frac{1}{2}\right) + \frac{1}{2}\delta\sigma_z, \tag{1.12}$$

with the dimensionless Zeeman splitting $\delta = mg/2m_0$, (m_0: bare mass of electron). Expressing the SO coupling in the same representation gives

$$\frac{H_{\mathrm{SO}}}{\hbar\omega_c} = \frac{1}{\sqrt{2}}\frac{l_B}{l_{\mathrm{SO}}}\left(a\sigma_+ + a^\dagger\sigma_-\right), \quad \sigma_\pm = \frac{1}{2}(\sigma_x \pm i\sigma_y), \tag{1.13}$$

with the magnetic length $l_B = (\hbar/m\omega_c)^{1/2}$ and the length scale of SO coupling $l_{\mathrm{SO}} = \hbar^2/2m\alpha$. Equation (1.13) shows that the Rashba SO interaction leads to a coupling of adjacent Landau levels with opposite spin. For strong magnetic field, this effect becomes negligible, as seen from the ratio l_B/l_{SO}. For typical InAs parameters, we find $l_{\mathrm{SO}} \sim 100\,\mathrm{nm}$. Thus, we may expect a significant effect of SO coupling for $B \leq 0.1\,\mathrm{T}$, as the prefactor in Eq. (1.13) becomes of order unity.

The diagonalisation of the Hamiltonian $H = H_0 + H_{\mathrm{SO}}$ is straightforward. The eigenenergies have been given by Bychkov & Rashba [12]. Here, we follow a different approach by noticing [31] that the Hamiltonian is formally identical to the integrable *Jaynes–Cummings model* (JCM) [32] of quantum optics. There, the JCM is used in the context of atom-light interaction where two atomic levels are described by a pseudo-spin. Transitions between the levels are induced by the electric dipole coupling to a quantised monochromatic radiation field which is modelled by a harmonic oscillator. In this language, H_{SO} describes transitions ($\sigma_\pm$) between the two atomic levels under absorption/emission of a photon of the radiation field (a, $a^\dagger$). Conversely, in the SO-interacting system, the roles of atomic pseudo-spin and light field are played by the real spin and the Landau level of the same electron. The properties of the JCM are discussed in appendix A.

The above analogy to a quantum optical model will be helpful in elucidating the effect of SO coupling in the following two chapters of the thesis when the models become non-integrable. In section 2.2, the JCM will reappear as a limit for quantum wires with Rashba SO coupling. In chapter 3, the notion of counter-rotating coupling terms (see section 2.2.4), which is closely related to definition of the JCM in quantum optics [33], leads us to the derivation of an integrable effective model for SO-interacting quantum dots.

Chapter 2

Rashba spin-orbit coupling in quantum wires

In the previous chapter, we have introduced the Rashba effect as a consequence of spin-orbit (SO) interaction in two-dimensional (2D) electron systems with dominating structure-inversion asymmetry.

In general, SO interaction couples the spin of a particle to its orbital motion. In mesoscopic systems, the latter can easily be modified by means of geometrical confinement, e. g. due to external gate voltages.

In the following, we want to illustrate how effects of SO coupling are modified by further constraining the motion of the electron in a single spatial direction by considering a quasi-one-dimensional system which is defined in the 2DEG. Similar to the Rashba effect, every electric field – and thus also the confining fields – may lead to a coupling between spin and momentum, see Eq. (1.1). These additional contributions to the SO coupling might become important when the lateral confinement is comparable to the vertical constraint that defines the 2DEG. This is the case in wires made by the *cleaved-edge overgrowth technique* [34] where both lateral and vertical confinement are typically of the order of $\sim 10\,\mathrm{nm}$. A further example where a full three-dimensional description of the SO coupling might be necessary are molecular systems like *carbon nanotubes* [35, 36].

Throughout this chapter, we restrict ourselves to ballistic quasi-one-dimensional electron systems whose lateral confinement is assumed to be much weaker than the vertical constraint of the 2DEG. This condition is usually fulfilled in quantum wires defined by external gates and etching, leading to a lateral width $\geq 100\,\mathrm{nm}$. We describe such a quantum wire by including a parabolic confining potential $V_c \propto x^2$ into the model for the 2D system [Eq. (1.3)].

In the following section, we present the scientific publication which comprises our main results for the interplay of SO coupling and lateral confinement in quan-

tum wires in perpendicular magnetic fields. In section 2.2, we provide more background information and various analytical limits for the numerical results. There, the Jaynes–Cummings model of quantum optics will reappear as the high magnetic field limit in the context of the rotating-wave approximation. In section 2.3, we give a brief introduction to ballistic transport in quasi-1D systems and demonstrate the importance of evanescent modes in the context of mode matching analysis. We give an example for this analysis in SO-interacting systems by considering the transmission properties of a strict-1D wire with a magnetic modulation. We find a commensurability effect in the spin-dependent transmission when the period of modulation becomes comparable to the SO-induced spin precession.

2.1 Rashba effect and magnetic field in semiconductor quantum wires*

Abstract: We investigate the influence of a perpendicular magnetic field on the spectral and spin properties of a ballistic quasi-one-dimensional electron system with Rashba effect. The magnetic field strongly alters the spin-orbit induced modification to the subband structure when the magnetic length becomes comparable to the lateral confinement. A subband-dependent energy splitting at $k = 0$ is found which can be much larger than the Zeeman splitting. This is due to the breaking of a combined spin orbital-parity symmetry.

2.1.1 Introduction

The quest for a better understanding of the influence of the electron spin on the charge transport in non-magnetic semiconductor nanostructures has considerably attracted interest during recent years [37]. Spin-orbit interaction (SOI) is considered as a possibility to control and manipulate electron states via gate voltages [38, 39]. This has generated considerable research activity, both in theory and experiment, motivated by fundamental physics as well as applicational aspects. Especially, SOI induced by the Rashba effect [11,40] in semiconductor heterostructures as a consequence of the lack of structure inversion symmetry [18] is important. In these two-dimensional (2D) systems the Rashba effect leads to spin precession of the propagating electrons. The possibility to manipulate the strength of the Rashba effect by an external gate voltage has been demonstrated experimentally [24, 25, 27, 41]. This is the basis of the spin dependent field-effect-transistor

*This section has been accepted for publication in Physical Review B **71** (2005). E-print: S. Debald, B. Kramer, cond-mat/0411444 at www.arxiv.org.

(spinFET) earlier discussed theoretically by Datta and Das [42]. Numerous theoretical spintronic devices have been proposed using interference [43–47], resonant tunnelling [25, 48–50], ferromagnet-semiconductor hybrid structures [51–55], multi-terminal geometries [56–61], and adiabatic pumping [62]. Magnetic field effects on the transport properties in 2D systems with SOI have been investigated theoretically [63–65] as well as experimentally [24, 25, 27, 30, 41, 66].

In order to improve the efficiency of the spinFET the angular distribution of spin precessing electrons has to be restricted [42]. Thus, the interplay of SOI and quantum confinement in quasi-1D systems [67–70] and quantum Hall edge channels [71] has been studied. First experimental results on SOI in quantum wires have been obtained [72]. The presence of a perpendicular magnetic field has been suggested to relax the conditions for the external confining potential for quantum point contacts. In these systems a Zeeman-like spin splitting at $k=0$ has been predicted from the results of numerical calculations when simultaneously SOI and a magnetic field are present [73]. The effect of an in-plane magnetic field on the electron transport in quasi-1D systems has also been calculated [74–76].

In this work, we investigate the effect of a perpendicular magnetic field on the spectral and spin properties of a ballistic quantum wire with Rashba spin-orbit interaction. The results are twofold. First, we show that transforming the one-electron model to a bosonic representation yields a systematic insight into the effect of the SOI in quantum wires, by using similarities to atom-light interaction in quantum optics for high magnetic fields. Second, we demonstrate that spectral and spin properties can be systematically understood from the symmetry properties. Without magnetic field the system has a characteristic symmetry property — the invariance against a combined spin orbital-parity transformation — which is related to the presence of the SOI. This leads to the well-known degeneracy of energies at $k=0$. The eigenvalue of this symmetry transformation replaces the spin quantum number. A non-zero magnetic field breaks this symmetry and lifts the degeneracy. This magnetic field-induced energy splitting at $k=0$ can become much larger than the Zeeman splitting. In addition, we show that modifications of the one-electron spectrum due to the presence of the SOI are very sensitive to weak magnetic fields. Furthermore, we find characteristic hybridisation effects in the spin density. Both results are completely general as they are related to the breaking of the combined spin-parity symmetry.

This general argument explains the Zeeman-like splitting observed in recent numerical results [73].

2.1.2 The model

We study a ballistic quasi-1D quantum wire with SOI in a perpendicular magnetic field. The system is assumed to be generated in a 2D electron gas (2DEG) by

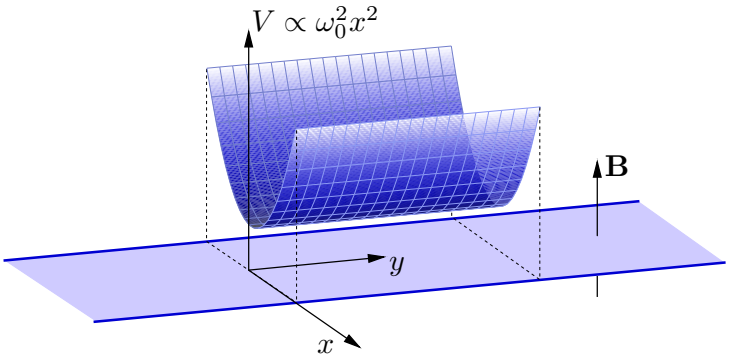

Figure 2.1: Model of the quantum wire.

means of a gate-voltage induced parabolic lateral confining potential. We assume that the SOI is dominated by structural inversion asymmetry. This is a reasonable approximation for InAs based 2DEGs [25]. Therefore, the SOI is modelled by the Rashba effect [11, 40], leading to the Hamiltonian

$$H = \frac{(\mathbf{p}+\frac{e}{c}\mathbf{A})^2}{2m} + V(x) + \frac{1}{2}g\mu_B B\sigma_z - \frac{\alpha}{\hbar}\left[(\mathbf{p}+\frac{e}{c}\mathbf{A})\times\boldsymbol{\sigma}\right]_z, \tag{2.1}$$

where m and g are the effective mass and Landé factor of the electron, and $\boldsymbol{\sigma}$ is the vector of the Pauli matrices. The magnetic field is parallel to the z-direction (Fig. 2.1), and the vector potential $\mathbf{A}$ is in the Landau gauge. Three length scales characterise the relative strengths in the interplay of confinement, magnetic field B, and SOI,

$$l_0 = \sqrt{\frac{\hbar}{m\omega_0}}, \quad l_B = \sqrt{\frac{\hbar}{m\omega_c}}, \quad l_{\mathrm{SO}} = \frac{\hbar^2}{2m\alpha}. \tag{2.2}$$

The length scale l_0 corresponds to the confinement potential $V(x) = (m/2)\omega_0^2 x^2$, l_B is the magnetic length with $\omega_c = eB/mc$ the cyclotron frequency and l_{SO} is the length scale associated with the SOI. In a 2DEG the latter is connected to a spin precession phase $\Delta\theta = L/l_{\mathrm{SO}}$ if the electron propagates a distance L.

Because of the translational invariance in the y-direction the eigenfunctions can be decomposed into a plane wave in the longitudinal direction and a spinor which depends only on the transversal coordinate x,

$$\boldsymbol{\Psi}_k(x,y) = e^{iky}\begin{pmatrix}\phi_k^{\uparrow}(x)\\ \phi_k^{\downarrow}(x)\end{pmatrix} =: e^{iky}\boldsymbol{\phi}_k(x). \tag{2.3}$$

With this and by defining creation and annihilation operators of a shifted harmonic oscillator, $a_k^\dagger$ and a_k, which describe the quasi-1D subbands in the case without

SOI, the transversal wavefunction component satisfies

$$H(k)\,\boldsymbol{\phi}_k(x) = E_k\,\boldsymbol{\phi}_k(x), \tag{2.4}$$

for k fixed with the Hamiltonian

$$\begin{aligned}\frac{H(k)}{\hbar\omega_0} =& \Omega\left(a_k^\dagger a_k + \frac{1}{2}\right) + \frac{1}{2}\frac{(kl_0)^2}{\Omega^2} \\ &+ \frac{1}{2}\begin{pmatrix}\xi_1 kl_0 + \xi_2(a_k + a_k^\dagger) \\ \xi_3(a_k - a_k^\dagger) \\ \delta\end{pmatrix}\cdot\boldsymbol{\sigma},\end{aligned} \tag{2.5}$$

the abbreviations

$$\Omega = \frac{\sqrt{\omega_0^2 + \omega_c^2}}{\omega_0} = \sqrt{1 + \left(\frac{l_0}{l_B}\right)^4}, \tag{2.6}$$

$$\xi_1 = \frac{l_0}{l_{\mathrm{SO}}}\frac{1}{\Omega}, \tag{2.7}$$

$$\xi_2 = \frac{1}{\sqrt{2}}\frac{l_0}{l_{\mathrm{SO}}}\left(\frac{l_0}{l_B}\right)^2\frac{1}{\sqrt{\Omega}}, \tag{2.8}$$

$$\xi_3 = \frac{i}{\sqrt{2}}\frac{l_0}{l_{\mathrm{SO}}}\sqrt{\Omega}, \tag{2.9}$$

and the dimensionless Zeeman splitting

$$\delta = \frac{1}{2}\left(\frac{l_0}{l_B}\right)^2\frac{m}{m_0}g, \tag{2.10}$$

(m_0 is the bare mass of the electron).

This representation of the Hamiltonian corresponds to expressing the transverse wavefunction in terms of oscillator eigenstates such that $a_k^\dagger a_k$ gives the subband index of the electron which propagate with longitudinal momentum $\hbar k$. The magnetic field leads to the lateral shift of the wavefunction and the renormalisation of the oscillator frequency Ω. Moreover, the effective mass in the kinetic energy of the longitudinal propagation is changed. The last term in Eq. (2.5) describes how the SOI couples the electron's orbital degree of freedom to its spin. Due to the operators $a_k^\dagger$ and a_k the subbands corresponding to one spin branch are coupled to the same and nearest neighbouring subbands of opposite spin, see Fig. 2.2a.

Formally, for k fixed Eq. (2.5) can be regarded as a simple spin-boson system where the spin of the electron is coupled to a mono-energetic boson field which represents the transverse orbital subbands. This interpretation leads to an analogy to the atom-light interaction in quantum optics. There, the quantised bosonic radiation field is coupled to a pseudo-spin that approximates the two atomic levels between which electric dipole transitions occur. In our model, the roles of atomic pseudo-spin and light field are played by the spin and the orbital transverse modes of the electron, respectively.

Indeed, in the limit of a strong magnetic field, $l_B \ll l_0$, and $kl_0 \ll 1$ Eq. (2.5) converges against the exactly integrable Jaynes-Cummings model (JCM) [32],

$$\frac{H_{\mathrm{JC}}}{\hbar\omega_c} = a^\dagger a + \frac{1}{2} + \frac{1}{4}\frac{m}{m_0} g\sigma_z + \frac{1}{\sqrt{2}}\frac{l_B}{l_{\mathrm{SO}}}(a\sigma_+ + a^\dagger\sigma_-)\,. \tag{2.11}$$

This system is well known in quantum optics. It is one of the most simple models to couple a boson mode and a two-level system [33]. In the case of the quantum wire with SOI one can show that in the strong magnetic field limit the rotating-wave approximation [33], which leads to the JCM, becomes exact. This is because for $l_{\mathrm{B}} \ll l_0$ and $kl_0 \ll 1$ the electrons are strongly localised near the centre of the quantum wire and thus insensitive to the confining potential. In this limit, there is a crossover to the 2D electron system with SOI in perpendicular magnetic field for which the formal identity to the JCM has been asserted previously [31].

In this context, it is important to note that the JCM is known to exhibit Rabi oscillations in optical systems with atomic pseudo-spin and light field periodically exchanging excitations. Recently, an experimentally feasible scheme for the production of coherent oscillations in a single few-electron quantum dot with SOI has been proposed [77] with the electron's spin and orbital angular momentum exchanging excitation energy. This highlights the general usefulness of mapping parabolically confined systems with SOI onto a bosonic representation as shown in Eq. (2.5). Related results have been found in a 3D model in nuclear physics where the SOI leads to a *spin-orbit pendulum* effect [78, 79].

2.1.3 Symmetry properties

Without magnetic field it has been pointed out previously that one effect of SOI in 2D is that no common axis of spin quantisation can be found, see e.g. Ref. [69,70]. Since the SOI is proportional to the momentum it lifts spin degeneracy only for $k \neq 0$. From the degeneracy at $k = 0$ a binary quantum number can be expected at $B = 0$. It can easily be shown that for any symmetric confinement potential $V(x) = V(-x)$ in Eq. (2.1) — which includes the 2D case for $V \equiv 0$ or symmetric multi-terminal junctions [56–59] — the Hamiltonian is invariant under the unitary

transformation

$$U_x = e^{i2\pi\hat{P}_x\hat{S}_x/\hbar} = i\hat{P}_x\sigma_x, \tag{2.12}$$

where $\hat{P}_x$ is the inversion operator for the x-component, $\hat{P}_x f(x,y) = f(-x,y)$. Thus, the observables H, p_y and $\hat{P}_x\sigma_x$ commute pairwise. Without SOI, $\hat{P}_x$ and σ_x are conserved separately. With SOI, both operators are combined to form the new constant of motion $\hat{P}_x\sigma_x$ which is called *spin parity*. When introducing a magnetic field with a non-zero perpendicular component the spin parity symmetry is broken and we expect the degeneracy at $k = 0$ to be lifted. As a side remark, by using oscillator eigenstates and the representation of eigenstates of σ_z for the spinor, the Hamiltonian $H(k)$ in Eq. (2.5) becomes real and symmetric. We point out that in this choice of basis the transformation $U_y = i\hat{P}_y\sigma_y$ is a representation of the time-reversal operation which for $B = 0$ also commutes with H. However, it does not commute with p_y and no further quantum number can be derived from U_y [80]. The effect of the symmetry $\hat{P}_x\sigma_x$ on the transmission through symmetric four [56] and three-terminal [57, 58] devices has been studied previously.

We recall that the orbital effect of the magnetic field leads to a twofold symmetry breaking: the breaking of the spin parity $\hat{P}_x\sigma_x$ lifts the $k = 0$ degeneracy (even without the Zeeman effect) and the breaking of time-reversal symmetry lifts the Kramers degeneracy. For $B = 0$ we can attribute the quantum numbers (k,n,s) to an eigenstate where n is the subband index corresponding to the quantisation of motion in x-direction and $s = \pm 1$ is the quantum number of spin parity. For $B \neq 0$, due to the breaking of spin parity, n and s merge into a new quantum number leading to the non-constant energy splitting at $k = 0$ which will be addressed in the next Section when treating the spectral properties.

For weak SOI ($l_{\mathrm{SO}} \gg l_0$) one finds in second order that the spin splitting at $k = 0$ for the nth subband is

$$\frac{\Delta_n}{\hbar\omega_0} = \delta + \frac{1}{2}\left(\frac{l_0}{l_{\mathrm{SO}}}\right)^2 \frac{(\Omega-\delta)\chi_1^2 - (\Omega+\delta)\chi_2^2}{\Omega^2-\delta^2}\left(n+\frac{1}{2}\right), \tag{2.13}$$

where $\chi_{1,2} = 2^{-1/2}[(l_0/l_B)^2\Omega^{-1/2} \mp \Omega^{1/2}]$. The first term is the bare Zeeman splitting and the SOI-induced second contribution has the peculiar property of being proportional to the subband index. In addition, for weak magnetic field ($l_0 \ll l_B$) the splitting is proportional B,

$$\frac{\Delta_n}{\hbar\omega_0} \approx \delta - \left(\frac{l_0}{l_{\mathrm{SO}}}\right)^2\left(\frac{l_0}{l_B}\right)^2\left(1+\frac{1}{4}\frac{m}{m_0}g\right)\left(n+\frac{1}{2}\right). \tag{2.14}$$

This is expected because by breaking the spin parity symmetry at non-zero B the formerly degenerate levels can be regarded as a coupled two-level system for which it is known that the splitting into hybridised energies is proportional to the coupling, i.e. the magnetic field B.

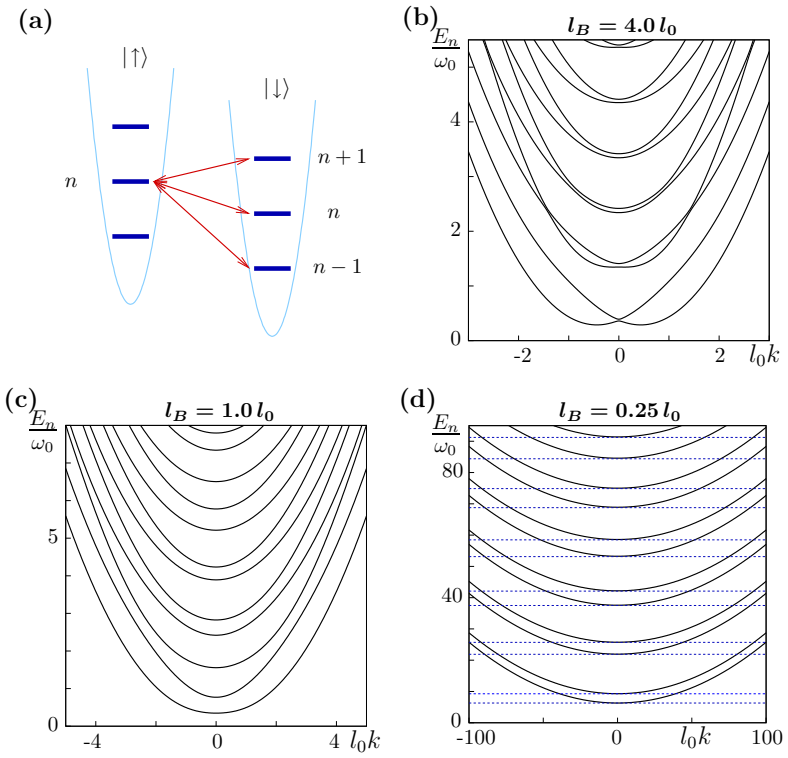

Figure 2.2: **(a)** Spin-orbit induced coupling of subbands with opposite spins in a quantum wire. **(b)-(d)** Spectra of a quantum wire with SOI for different strengths of perpendicular magnetic field for $l_{\mathrm{SO}} = l_0$ and typical InAs parameters: $\alpha = 1.0 \cdot 10^{-11}\,e\mathrm{Vm}$, $g = -8$, $m = 0.04\,m_0$. For strong magnetic field **(d)** the convergence towards the Jaynes-Cummings model (JCM) can be seen (dashed: eigenenergies of JCM).

2.1.4 Spectral properties

Due to the complexity of the coupling between spin and subbands in Eq. (2.5), apart from some trivial limits, no analytic solution of the Schrödinger equation can be expected. We find the eigenfunctions and energies of the Hamiltonian by exact numerical diagonalisation. Figures 2.2b–d show the spectra for different strengths of magnetic field and parameters typical for InAs: $\alpha = 1.0 \cdot 10^{-11}\,e\mathrm{Vm}$, $g = -8$, $m = 0.04\,m_0$. We set $l_{\mathrm{SO}} = l_0$ which corresponds to a wire width $l_0 \approx 100\,\mathrm{nm}$.

For the case without magnetic field it has been asserted previously that the interplay of SOI and confinement leads to strong spectral changes like non-parabolicities and anticrossings when l_{SO} becomes comparable to l_0 [67, 69, 70]. In Fig. 2.2b we find similar results in the limit of a weak magnetic field. However, as an effect of non-vanishing magnetic field we observe a splitting of the formerly

spin degenerate energies at $k=0$. For the Zeeman effect it is expected that the corresponding spin splitting is constant. In contrast, in Fig. 2.2b–d the splitting at $k=0$ depends on the subband. This additional splitting has been predicted in Sec. 2.1.3 in terms of a symmetry breaking effect when SOI and perpendicular magnetic field are simultaneously present.

Figure 2.3a shows the eigenenergies $E_n(k=0)$ for $l_{\mathrm{SO}}=l_0$ as a function of magnetic field in units of hybridised energies, $(\omega_0^2+\omega_c^2)^{1/2}$. Three different regimes can be distinguished. (i) For small magnetic field ($l_0/l_B \ll 1$) the energy splitting evolves from the spin degenerate case (triangles) due to the breaking of spin parity. Although the perturbative results Eq. (2.13) cannot be applied to the case $l_{\mathrm{SO}}=l_0$ in Fig. 2.3a, the energy splitting at small magnetic field and the overall increasing separation for higher subbands are reminiscent of the linear dependences on n and B found in Eqs. (2.13) and (2.14). (ii) For $l_0/l_B \approx 1$, the energy splitting is comparable to the subband separation which indicates the merging of the quantum numbers of the subband and the spin parity into a new major quantum number. For higher subbands, the SOI-induced splitting even leads to anticrossings with neighbouring subbands. (iii) Finally, the convergence to the JCM implies that the splittings should saturate for large B (Fig. 2.2d). The dashed lines in Fig. 2.3a show the energies of the spin-split Landau levels, $E_n/\hbar\omega_0=(l_0/l_B)^2(n+1/2)\pm\delta/2$ for $l_0=4l_B$, indicating that the SOI-induced energy splitting is always larger than the bulk Zeeman splitting. At $l_0\approx l_B$ the SOI-induced splitting exceeds the Zeeman effect by a factor 5. This is remarkable because of the large value of the g-factor in InAs.

For our wire parameters the sweep in Fig. 2.3a corresponds to a magnetic field $B\approx 0-1\,\mathrm{T}$. Considering the significant spectral changes due to breaking of spin parity at $l_B\approx l_0$ ($B\approx 70\,\mathrm{mT}$) we conclude that the SOI-induced modifications in the wire subband structure are very sensitive to weak magnetic fields (Fig. 2.2b, c). This may have consequences for spinFET designs that rely on spin polarised injection from ferromagnetic leads because stray fields can be expected to alter the transmission probabilities of the interface region.

The SOI-induced enhancement of the spin splitting should be accessible via optical resonance or ballistic transport experiments. The magnitude of the splitting suggests that this effect is robust against possible experimental imperfections like a small residual disorder. In a quasi-1D constriction the conductance is quantised in units of ne^2/h where n is the number of transmitting channels [81]. In the following, we neglect the influence of the geometrical shape of the constriction and that for small magnetic fields ($l_0/l_B<0.5$) the minima of the lowest subbands are not located at $k=0$ (Fig. 2.2b). In this simplified model we expect the conductance G to jump up one conductance quantum every time the Fermi energy passes through the minimum of a subband. Thus, in the case of spin degenerate subbands, G increases in steps with heights $2e^2/h$ (triangles in Fig. 2.3b).

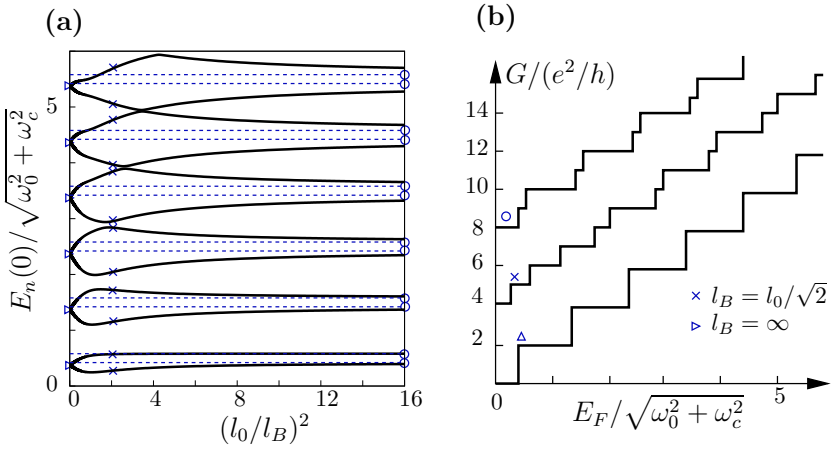

Figure 2.3: **(a)** Magnetic field evolution of $E_n(k=0)$ for $l_{\mathrm{SO}} = l_0$ in units of $\sqrt{\omega_0^2+\omega_c^2}$. Three different regimes of spin splitting can be distinguished (see text). Dashed lines correspond to Zeeman split Landau levels. **(b)** Simplified sketch of the ballistic conductance as a function of Fermi energy for $(l_0/l_B)^2 = 0$ (triangles), $(l_0/l_B)^2 = 2$ (crosses), and Zeeman-split Landau levels (circles). (Curves vertically shifted for clarity).

In principle, by sweeping the magnetic field the different regimes discussed in Fig. 2.3a can be distinguished in the ballistic conductance. For high magnetic field, the spin degeneracy is broken due to the Zeeman effect. This leads to a sequence of large steps (Landau level separation) interrupted by small steps (spin splitting) (circles in Fig. 2.3b). As a signature of the SOI we expect increasing spin splitting for higher Landau levels due to converging towards the JCM (Fig. 2.2d). Decreasing the magnetic field enhances the effects of SOI until at $l_B \approx l_0$ subband and spin splitting are comparable whereas the Zeeman effect becomes negligible (crosses in Fig. 2.3b).

2.1.5 Spin properties

Not only the energy spectra of the quantum wire are strongly affected by the breaking the spin parity $\hat{P}_x\sigma_x$. The latter symmetry has also profound consequences for the spin density,

$$\mathbf{S}_{n,k}(x) := \psi^{\dagger}_{n,k}\,\boldsymbol{\sigma}\,\psi_{n,k}. \tag{2.15}$$

To elucidate this in some detail we start with considering the case $B = 0$.

Without magnetic field, the spin parity is a constant of motion. The corresponding symmetry operation Eq. (2.12) leads to the symmetry property for the

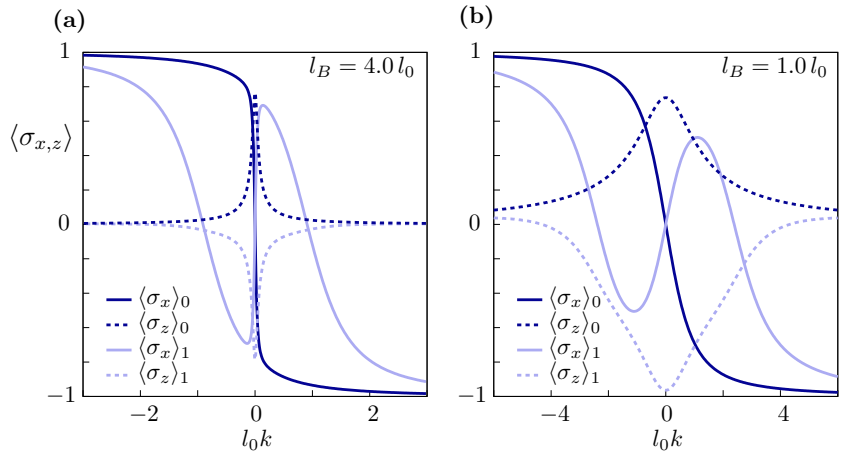

Figure 2.4: Expectation values of spin for the two lowest eigenstates for $l_{\mathrm{SO}} = l_0$. Solid: $\langle\sigma_x\rangle_n$, dashed: $\langle\sigma_z\rangle_n$. **(a)** weak magnetic field, $l_B = 4.0\,l_0$. Hybridisation of wavefunction at $k \approx 0$ leads to finite $\langle\sigma_z\rangle_n$ component. **(b)** Strong magnetic field, $l_B = 1.0\,l_0$.

wavefunction,

$$\psi^{\uparrow}_{n,k,s}(x) = s\,\psi^{\downarrow}_{n,k,s}(-x), \quad s = \pm 1, \tag{2.16}$$

where s denotes the quantum number of the spin parity. This symmetry requires the spin density components perpendicular to the confinement to be antisymmetric, $S^{y,z}_{n,k,s}(x) = -S^{y,z}_{n,k,s}(-x)$, leading to vanishing spin expectation values, $\langle\sigma_{y,z}\rangle_{n,k,s} = \int dx S^{y,z}_{n,k,s}(x) = 0$. We note that using the σ_z-representation for spinors even leads to zero longitudinal spin *density* $S^{y}_{n,k,s}(x) \equiv 0$ because the real and symmetric Hamiltonian $H(k)$ implies *real* transverse wavefunctions independent of the spin parity. Therefore, it is sufficient to consider the x- and z-components of the spin, only.

For zero magnetic field, it has been pointed out that for large k the spin is approximately quantised in the confinement direction [69, 70]. This is due to the so-called *longitudinal-SOI approximation* [68] which becomes valid when the term linear in k in the SOI [Eq. (2.5)] exceeds the coupling to the neighbouring subbands.

The perpendicular magnetic field breaks spin parity and thereby leads to a hybridisation of formerly degenerate states for small k. In addition, the breaking of the symmetry of the wavefunction Eq. (2.16) leads to modifications of the spin density.

In Fig. 2.4 the expectation value of spin is shown as a function of the longitudinal momentum for the two lowest subbands. For weak magnetic field (Fig. 2.4a) results similar to the zero magnetic field case [69, 70] are found. For large k

the spinor is effectively described by eigenstates of σ_x which concurs with the longitudinal-SOI approximation. However, for $k \approx 0$ the hybridisation of the wavefunction leads to a finite value of $\langle\sigma_z\rangle$. This corresponds to the emergence of the energy splitting at $k = 0$ in Fig. 2.2b which can be regarded as an additional effective Zeeman splitting that tilts the spin into the σ_z-direction — even without a real Zeeman effect. This effect becomes even more pronounced for large magnetic field (Fig. 2.4b). Here, for small k, the spin of the lowest subband is approximately quantised in σ_z direction. The spin expectation values in Fig. 2.4 depend only marginally on the strength of the Zeeman effect. No qualitative difference is found for $g = 0$.

2.1.6 Conclusion

In summary, the effect of a perpendicular magnetic field on a ballistic quasi-1D electron system with Rashba effect is investigated. It is shown that the spectral and spin features of the system for small k are governed by a compound spin orbital-parity symmetry of the wire. Without magnetic field this *spin parity* is a characteristic property of symmetrically confined systems with Rashba effect and leads to a binary quantum number which replaces the quantum number of spin. This symmetry is also responsible for the well-known degeneracy for $k = 0$ in systems with Rashba effect. A non-zero magnetic field breaks the spin-parity symmetry and lifts the corresponding degeneracy, thus leading to a magnetic field induced energy splitting at $k = 0$ which can become much larger than the Zeeman splitting. Moreover, we find that the breaking of the symmetry leads to hybridisation effects in the spin density.

The one-electron spectrum is shown to be very sensitive to weak magnetic fields. Spin-orbit interaction induced modifications of the subband structure are strongly changed when the magnetic length becomes comparable to the lateral confinement of the wire. This might lead to consequences for spinFET designs which depend on spin injection from ferromagnetic leads because of magnetic stray fields.

For the example of a quantum wire, we demonstrate that in the case of a parabolical confinement it is useful to map the underlying one-electron model onto a bosonic representation which shows for large magnetic field many similarities to the atom-light interaction in quantum optics. In Ref. [77] this mapping is utilised to predict spin-orbit driven coherent oscillations in single quantum dots.

This work was supported by the EU via TMR and RTN projects FMRX-CT98-0180 and HPRN-CT2000-0144, and DFG projects Kr 627/9-1, Br 1528/4-1. We are grateful to T. Brandes, T. Matsuyama and T. Ohtsuki for useful discussions.

2.2 Spectral properties, various limits

Geometrical confinement leads to quantisation of the orbital motion. Therefore, the natural language to describe the wavefunction in a quasi-1D electron system is in terms of confined transverse subbands. In Sec. 2.1.2, the effective mass Hamiltonian of the spin-orbit (SO) interacting quantum wire (QWR) [Eq. (2.1) on page 18] is rewritten in the basis of transverse subbands corresponding to parabolic confinement. Formally, this leads to a bosonic representation [Eq. (2.5) on page 19] in which the SO interaction leads to a coupling between nearest-neighbouring subbands of opposite spin, see Fig. 2.2a. In Eq. (2.5) the operators $a_k^\dagger$ and a_k act on the transverse eigenstates such that $a_k^\dagger a_k$ gives the subband number of the electron that propagates with longitudinal momentum $\hbar k$. Clearly, electrons are fermions. We use the notion "bosonic" because the oscillator operators have a commutator $[a_k, a_k^\dagger] = 1$. Here, $a_k^\dagger$ and a_k describe transitions between transverse subbands – not particle creation and annihilation. In this form, the Hamiltonian resembles models of matter-light interaction of quantum optics like the *Rabi Hamiltonian* [82], where, in the simplest case, two atomic levels – representing a pseudo-spin – are coupled to a monochromatic radiation mode, see Fig. 2.5. In quantum optics such pseudo-spin boson models consist of distinct physical subsystems (atom and light) whereas in the case of QWR two degrees of freedom of the same particle are coupled.

Due to the complexity of the coupling between spin and orbitals in Eq. (2.5), in general, no analytical solution of the Hamiltonian is feasible. We apply an exact numerical diagonalisation to find the spectral properties of the wire. Figure 2.6 shows the low-energy spectra of the QWR for various strengths of confinement, SO coupling and perpendicular magnetic field. For a better physical understanding we summarise analytical limits and approximations in the following.

2.2.1 Zero magnetic field

For $B = 0$ the Hamiltonian (2.5) reduces to

$$\frac{H(k)}{\hbar\omega_0} = a_k^\dagger a_k + \frac{1}{2} + \frac{1}{2}(kl_0)^2 + \frac{1}{2}\frac{l_0}{l_{\mathrm{SO}}}\left(kl_0\sigma_x + \frac{i}{\sqrt{2}}\left(a_k - a_k^\dagger\right)\sigma_y\right), \tag{2.17}$$

$$=: H_0 + H_{\mathrm{mix}}, \tag{2.18}$$

with $H_{\mathrm{mix}} = 2^{-3/2} i (l_0/l_{\mathrm{SO}})(a_k - a_k^\dagger)\sigma_y$. This limit was studied in detail by Moroz & Barnes [67], and Governale & Zülicke [69, 70]. H_0 represents the maxi-

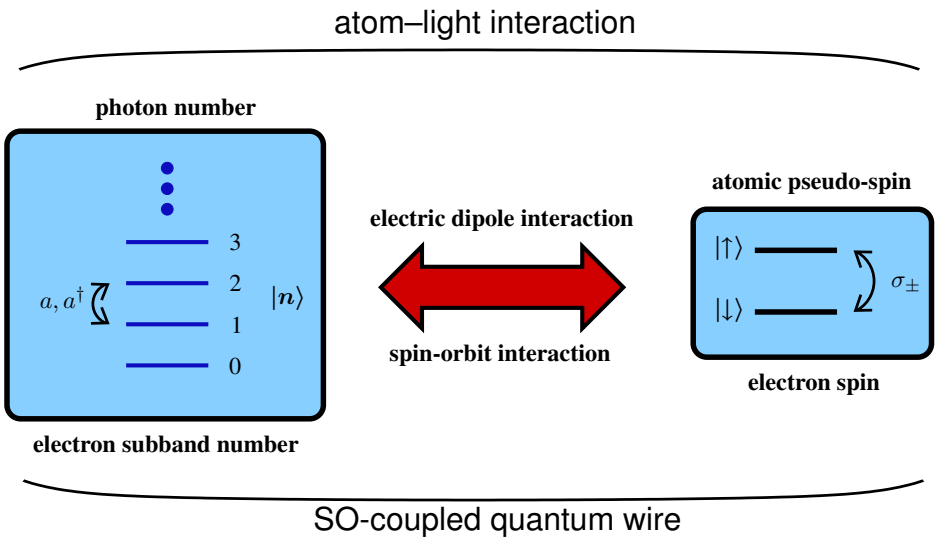

Figure 2.5: Analogy between spin-orbit interacting quantum wire and atom-light interaction in quantum optics.

mally commuting subsystem with energies of shifted parabolic subbands [69],

$$\frac{E^{\pm}_{0,n}}{\hbar\omega_0} = n + \frac{1}{2} + \frac{1}{2}\left(kl_0 \pm \frac{1}{2}\frac{l_0}{l_{\mathrm{SO}}}\right)^2 - \frac{1}{8}\left(\frac{l_0}{l_{\mathrm{SO}}}\right)^2, \tag{2.19}$$

where $\pm$ denotes eigenstates with spin (anti)parallel to σ_x. The shift of the dispersion depends on the spin and the strength of the SO coupling $k_{\mathrm{SO}} = \pm 1/2l_{\mathrm{SO}}$.

H_{mix} symmetrically couples adjacent subbands of H_0. In the limit of $|kl_0| \gg 1$ and $l_0/l_{\mathrm{SO}} \ll 1$ (corresponding to weak SO coupling) the H_{mix} term can be neglected, leading to the so-called *longitudinal-SO approximation* [68]. Within this approximation, spinors are given by eigenstates of σ_x, where the spin is fixed by the propagation direction of the electron due to k-linear prefactor of σ_x in H_0. Thus, for large momenta, right(left)-moving electrons have approximately spin-down(up) polarisation with respect to σ_x. The shifted parabolic subbands of the longitudinal-SO approximation are also seen in the result for weak magnetic field, Fig. 2.6 (left panel in upper row).

The transversal part of the SO coupling H_{mix} becomes important in the regime where neighbouring subbands of H_0 become degenerate, leading to anticrossings as seen in Fig. 2.6 (central panel in upper row). In general, no common spin quantisation axis can be found. This can also be seen in the spin properties for weak magnetic field, Fig. 2.4a. The zero-B result is given by the envelope of the hysteresis-like solid curves. For finite momenta, the tilt of the spin does depend on k. Only for large momenta, $l_0 k \gg 1$, the spin is approximately quantised in σ_x direction.

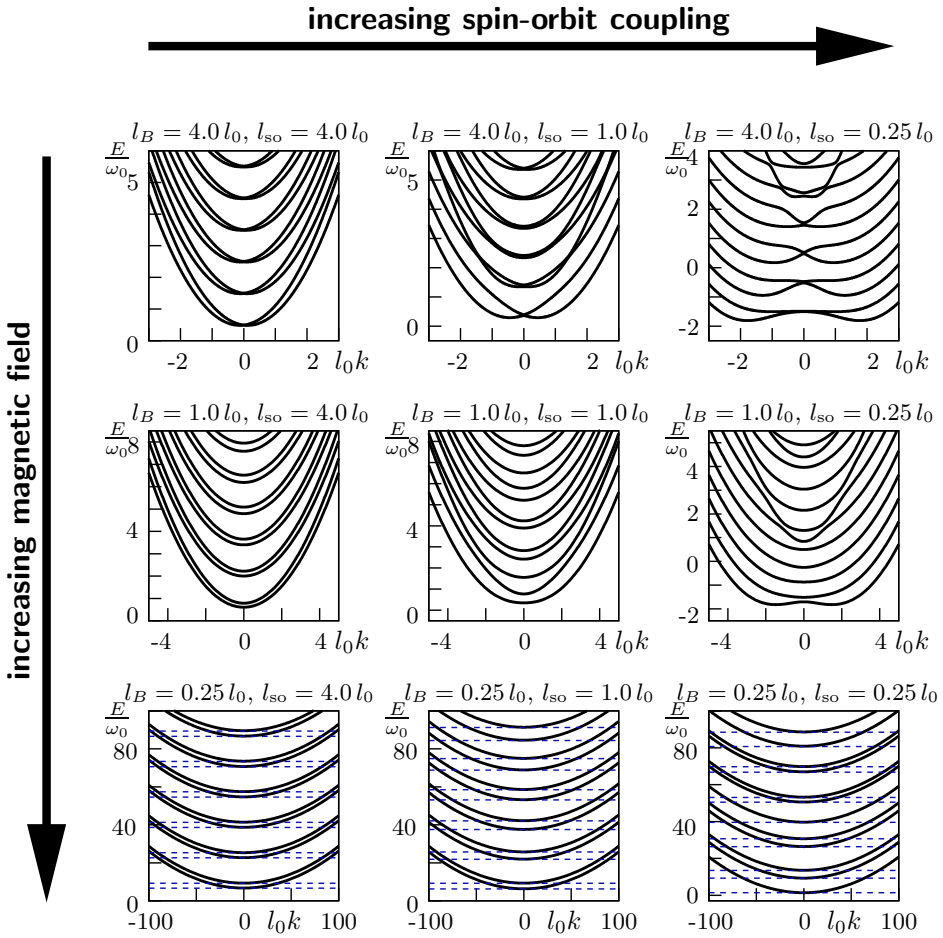

Figure 2.6: Low-energy spectra of an SO-interacting quantum wire found by numerical diagonalisation. Various regimes in the interplay of SO coupling and perpendicular magnetic field are shown. For strong magnetic field (lower row) the spectrum of the Jaynes–Cummings model are shown (dashed lines).

2.2.2 Two-band model

In the low-energy limit with a strong lateral confinement and a low electron density, Fermi points exist for the lowest subbands, only. Governale and Zülicke introduced a *two-band model* by truncating the Hilbert space to the two lowest spin-split subbands [69]. The corresponding matrix representation of dimension 4×4 is simple enough to be solved analytically but it goes beyond the longitudinal-SO approximation by showing an anticrossing. This model has been applied to calculate the transmission through an SO-interacting wire of finite length which was attached to perfect leads [69]. If the Fermi energy is placed between the two subband – making the lowest one a transmitting channel whereas the upper

band is evanescent – the scattering to the evanescent modes is shown to lead to spin-accumulation at the interface region with the leads.

However, since the Hilbert space is drastically truncated in this model, only the lowest subband resembles the exact solution whereas evanescent modes show deviations due to the missing coupling to higher bands. In Sec. 2.3, we briefly outline the importance of evanescent modes in quasi-1D transport.

2.2.3 Non-zero magnetic field

Perpendicular magnetic fields affect both, the electron's orbitals (via introduction of cyclotron energy, lateral shift of wavefunction, renormalisation of effective mass) and the spin degree of freedom (via Zeeman effect). In addition, the Hamiltonian (2.5) shows that the SO coupling is also affected by a magnetic field.

We now extend the longitudinal-SO approximation to include the effect of a weak magnetic field.[†] In analogy with Sec. 2.2.1, we decompose the Hamiltonian (2.5) into $H(k)/\hbar\omega_0 = H_0 + H_{\rm mix}$ where

$$H_0 = \Omega\left(a_k^\dagger a_k + \frac{1}{2}\right) + \frac{1}{2}\frac{(kl_0)^2}{\Omega^2} + \frac{1}{2}\left(\xi_1 kl_0 + \xi_2(a_k + a_k^\dagger)\right)\sigma_x, \tag{2.20}$$

$$H_{\rm mix} = \frac{1}{2}\left[\xi_3\left(a_k - a_k^\dagger\right)\sigma_y + \delta\sigma_z\right], \tag{2.21}$$

where we use the same abbreviations as in Sec. 2.1.2. Choosing eigenstates of σ_x, denoted by $|\uparrow\downarrow\rangle$, H_0 becomes diagonal in spin,

$$H_0^{\uparrow\downarrow} = \Omega\left(a_k^\dagger a_k + \frac{1}{2}\right) + \frac{1}{2}\left(\frac{kl_0}{\Omega} \pm \frac{1}{2}\frac{l_0}{l_{\rm SO}}\right)^2 - \frac{1}{8}\left(\frac{l_0}{l_{\rm SO}}\right)^2 \pm \frac{1}{2}\xi_2\left(a_k^\dagger + a_k\right). \tag{2.22}$$

A comparison with the zero-magnetic field solution Eq. (2.19) shows that, apart from a trivial energy renormalisation, the effect of the magnetic field solely enters through the rightmost term in Eq. (2.22). This term can be interpreted as being caused by a *spin-dependent* effective electric field pointing in x-direction, $\mathbf{E}_\sigma = \pm E\hat{\mathbf{e}}_x$. Having this analogy in mind, it is straightforward to diagonalise Eq. (2.22) by defining displaced boson operators [83],

$$A_{\uparrow\downarrow} = a_k \pm \frac{1}{2}\frac{\xi_2}{\Omega}, \quad A_{\uparrow\downarrow}^\dagger = a_k^\dagger \pm \frac{1}{2}\frac{\xi_2}{\Omega}, \tag{2.23}$$

leading to

$$H_0^{\uparrow\downarrow} = \Omega\left(A_{\uparrow\downarrow}^\dagger A_{\uparrow\downarrow} + \frac{1}{2}\right) + \frac{1}{2}\left(\frac{kl_0}{\Omega} \pm \frac{1}{2}\frac{l_0}{l_{\rm SO}}\right)^2 - \frac{1}{8}\left(\frac{l_0}{l_{\rm SO}}\right)^2 - \frac{1}{4}\frac{\xi_2^2}{\Omega}, \tag{2.24}$$

[†] Strong magnetic fields lead to a significant Zeeman splitting and a pronounced asymmetry in the coupling between adjacent subbands (see next section).

with eigenstates

$$|n,\uparrow\downarrow\rangle = |n\rangle_{\uparrow\downarrow}\,|\uparrow\downarrow\rangle, \quad |n\rangle_{\uparrow\downarrow} = \frac{1}{\sqrt{n!}}\left(A^\dagger_{\uparrow\downarrow}\right)^n |0\rangle_{\uparrow\downarrow}. \tag{2.25}$$

Thus, at the level of this *extended longitudinal-SO approximation*, the simultaneous effect of weak SO coupling and magnetic field leads to a spin-dependent shift of the wavefunction. In comparison with the zero-B result Eq. (2.19), however, the spectral properties are only affected by a constant shift of the ground state energy by $-\xi_2^2/4\Omega$, as one might have expected from the analogy with the electric field.

Remark: Equation (2.25) gives good insight into the approximate properties of eigenfunctions and energies in the low-coupling limit. However, in the context of a numerical diagonalisation of the full Hamiltonian $H_0 + H_{\rm mix}$, the basis $\{|n,\uparrow\downarrow\rangle\}$ is of little practical use. This is because the *orbital* wavefunctions $|n\rangle_{\uparrow\downarrow}$ correspond to differently displaced oscillators for opposite spin, hence not fulfilling orthogonality, ${}_{\uparrow\downarrow}\langle n|m\rangle_{\downarrow\uparrow} \neq \delta_{nm}$.

2.2.4 High-field limit

For the zero magnetic field case, the coupling of adjacent subbands is symmetric, see Eq. (2.17). With increasing field this coupling becomes more and more asymmetric due to ξ_2 and ξ_3 in Eqs. (2.20) and (2.21). This amounts to the convergence of the Hamiltonian against the *Jaynes–Cummings model* (see appendix A) in the high field limit: By introducing $\sigma_\pm = (\sigma_x \pm i\sigma_y)/2$, the Hamiltonian (2.5) can be rewritten as

$$\begin{aligned}\frac{H(k)}{\hbar\omega_0} = \Omega\left(a_k^\dagger a_k + \frac{1}{2}\right) + \frac{\delta}{2}\sigma_z + \frac{1}{2}\xi_1 k l_0 \sigma_x + \frac{1}{2}\frac{(kl_0)^2}{\Omega^2} \\ + \frac{1}{2}\frac{l_0}{l_{\rm SO}}\left[\gamma_r\left(a_k\sigma_+ + a_k^\dagger\sigma_-\right) + \gamma_c\left(a_k\sigma_- + a_k^\dagger\sigma_+\right)\right],\end{aligned} \tag{2.26}$$

where $(l_0/l_{\rm SO})\gamma_{r,c} = \xi_2 \mp i\xi_3$. In quantum optics, terms preceded by $\gamma_{r(c)}$ are called *(counter)-rotating*. This distinction becomes apparent when transforming into the interaction picture and comparing the time evolution of these terms. The first two terms on the right hand side of Eq. (2.26), $H_0 := \Omega(a_k^\dagger a_k + 1/2) + \delta\sigma_z/2$, correspond to the free evolution of the boson field of subbands and the spin. Thus, in the interaction picture with respect to H_0, boson and spin operators evolve as

$$\hat{a} = a\,e^{-i\Omega\tau}, \quad \hat{a}^\dagger = a^\dagger\,e^{i\Omega\tau}, \quad \hat{\sigma}_\pm = \sigma_\pm\,e^{\pm i\delta\tau}, \quad \tau := \omega_0 t. \tag{2.27}$$

Close to resonance $\Omega \approx \delta$ in Eq. (2.26), counter-rotating terms are rapidly oscillating in time as $\exp(2i\Omega\tau)$ whereas rotating terms become almost stationary. In

quantum optics, the neglect of the counter-rotating contributions with respect to the near-resonant ones is known as the *rotating-wave approximation* (RWA).

In our system, with increasing magnetic field, the relative weight of these terms becomes

$$\frac{\gamma_c}{\gamma_r} = \frac{\left(\frac{l_0}{l_B}\right)^2 - \Omega}{\left(\frac{l_0}{l_B}\right)^2 + \Omega} \longrightarrow 0, \quad \text{for } \frac{l_0}{l_B} \gg 1, \quad \text{by Eq. (2.6).} \tag{2.28}$$

Thus, in the high magnetic field limit the RWA of quantum optics becomes exact. For $\Omega \gg 1$, the system then converges against the Jaynes–Cummings model (JCM) (see also appendix A)

$$\frac{H_{\mathrm{JC}}}{\hbar\omega_c} = a^\dagger a + \frac{1}{2} + \frac{1}{4}\frac{m}{m_0} g\sigma_z + \frac{1}{\sqrt{2}}\frac{l_B}{l_{\mathrm{SO}}}(a\sigma_+ + a^\dagger\sigma_-)\,. \tag{2.29}$$

In high magnetic fields, the semiclassical trajectory of electrons is confined to cyclotron orbits. Thus, in the limit of $l_B \ll l_0$, the external parabolic confinement of the wire becomes negligible, leading to a crossover to a 2D SO-interacting system in perpendicular magnetic field for which the formal identity to the JCM was noted in Sec. 1.3.

In the high magnetic field regime of Fig. 2.6 (lower row) the solution of the JCM (see App. A) is shown in comparison with the exact solution of the full Hamiltonian, showing perfect agreement for $kl_0 \ll \Omega$.

2.2.5 Energy splitting at $k = 0$

In the last sections, we have introduced analytical limits for several regimes in the interplay of confinement, magnetic field, and SO coupling in QWRs. For weak SO coupling and magnetic field the extended longitudinal-SO approximation Eq. (2.22) gives good estimates for eigenstates and energies. Beyond this approximation, the two-band model is shown to demonstrate the appearance of anticrossings for stronger SO coupling. In addition, for high magnetic fields the Jaynes–Cummings model shows excellent agreement with the numerical data.

Due to the dominance of the cyclotron energy, an increasing magnetic field tends to suppress the SO-induced modifications on the spectra like anticrossings and non-parabolicities. Without magnetic field, these become important when the SO coupling is stronger than the confinement.

One further effect of the magnetic field becomes evident from the spectra in Fig. 2.6. Fir $B \neq 0$, the degeneracy at $k = 0$ is broken. In Sec. 2.1.3, this is explained in terms of the breaking of a combined spin orbital-parity symmetry when

SO coupling and perpendicular magnetic field act simultaneously. This energy splitting at $k = 0$ can also be calculated perturbatively.

We start from the unperturbed spectrum at $k = 0$ of the Hamiltonian (2.26), which is equivalent to Eq. (2.5), $E^{(0)}_{n,\uparrow\downarrow} = \Omega(n+1/2) \pm \delta/2$. The perturbation is given by

$$H_1 = \frac{1}{2}\frac{l_0}{l_{\mathrm{SO}}}\left[\left(\gamma_r a + \gamma_c a^\dagger\right)\sigma_+ + \left(\gamma_c a + \gamma_r a^\dagger\right)\sigma_-\right]. \tag{2.30}$$

Since H_1 is non-diagonal in spin, first order corrections vanish. Second order non-degenerate perturbation theory straightforwardly gives for the limit $|\Omega \pm \delta| > 1$ (far from resonance)

$$E^{(2)}_{n,\uparrow} = \frac{1}{4}\left(\frac{l_0}{l_{\mathrm{SO}}}\right)^2\left(\frac{\gamma_c^2 n}{\Omega+\delta} - \frac{\gamma_r^2(n+1)}{\Omega-\delta}\right), \tag{2.31}$$

$$E^{(2)}_{n,\downarrow} = \frac{1}{4}\left(\frac{l_0}{l_{\mathrm{SO}}}\right)^2\left(\frac{\gamma_r^2 n}{\Omega-\delta} - \frac{\gamma_c^2(n+1)}{\Omega+\delta}\right). \tag{2.32}$$

This leads to the $k = 0$ energy splitting $\Delta_n := E_{n,\uparrow} - E_{n,\downarrow}$ given by Eq. (2.13) which is discussed on page 21.

2.3 Electron transport in one-dimensional systems with Rashba effect

In low-dimensional systems which arise from quantum confinement, the theoretical treatment of transport depends on how it is driven through a system. When describing transport *parallel* to the barriers of the nanostructure (e.g. along the axis of a quantum wire), in many cases, kinetic Boltzmann equation formalisms can be used, thus, ignoring the phase information of the particles [3]. Effects of quantum mechanics solely enter through the appropriate quantum states in the presence of confinement and by transitions between them induced by scattering potentials. On the contrary, if transport is driven *through* barriers, quantum interference can be expected to become important when the particle traverses regions in which the medium changes on a length scale comparable to the phase coherence length of the particle. This condition is typically fulfilled in mesoscopic systems.

In the following, we are interested in transport through *open ballistic systems* where particles are injected from leads and where the transport properties of the system are determined by the transmission and reflection amplitudes. The quantum mechanical derivation of the transport properties of such systems generally involves the solution of the Schrödinger equation. Numerical approaches for

one-dimensional systems often employ discretised lattice models. In such single-particle tight-binding formulations, numerical techniques like the transfer-matrix or the recursive Green's function method are used to calculate the exact quantum coherent solution of the system for a given energy. Then, for instance, the conductance can be calculated after coherently connecting the system to leads [3]. These methods have extensively been applied to study localisation problems in disordered systems [84]. Recently, with increasing interest in spin-dependent transport, various spintronic devices have been addressed with tight-binding approaches. For instance, Bulgakov *et al.* [56] studied the spin-dependent transmission properties of a ballistic cross-junction structure. They found a SO-induced Hall-like effect when driving a spin polarised current through a four-terminal device (without magnetic field). Kiselev & Kim [57, 58] investigated ballistic T-shaped structures with SO interacting intersection region. They found that the device may redirect electrons with opposite spins from an unpolarised current, thus acting as a spin filter. Such behaviour is similar to the Stern-Gerlach experiment where the motion of paramagnetic atoms in a inhomogeneous magnetic field is altered depending on the spin.

In addition to such atomistic lattice calculations, continuum formulations of the transfer-matrix method (mode matching analysis) have also been applied to study e.g. the influence of scattering at impurities [85] and conductance fluctuations [86] in quasi-1D systems. The generalisation of this approach to include the effect of spin-orbit (SO) coupling, whilst straightforward in principle, is technically rather difficult because of the imperative determination of evanescent modes.

In the following we briefly formulate the necessity to treat evanescent modes in quasi-1D transport and the associated technical complications caused by SO coupling. As an example of the mode matching analysis, in Sec. 2.3.2, we discuss the interplay of SO coupling and an external magnetic modulation in the integrable strict-1D limit of a quantum wire. We find a commensurability effect in the spin-dependent transport characteristics when the modulation period is comparable to the SO-induced spin precession length.

2.3.1 Transmission in quasi-1D systems

When applying numerical tight-binding models to the problem of transmission through quasi-1D systems (e.g. in quantum waveguide structures as shown in Fig. 2.7) the discretisation of the lattice sets the dimension of the Hilbert space. Within this space the numerical solution of the Schrödiger equation is exact.

On the contrary, when utilising a continuum formulation of the transfer-matrix method, the *mode matching analysis* [3] may be used to derive the solution. The basic idea is to split a given geometry into sections and to calculate the solution of the Schrödinger equation by connecting the solutions of the individual sections.

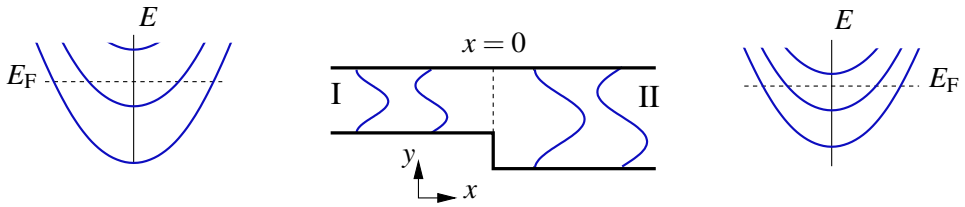

Figure 2.7: Sketch of interface between two quasi-1D wires with different widths (centre) and their dispersion relations (left and right). At the Fermi energy (dashed) only the lowest two subbands are propagating.

This is done by "matching" the transverse modes (and their probability flux[‡]) at the boundaries between the sections. We illustrate this with the basic example of a discontinuity of a quantum waveguide which is shown in Fig. 2.7. In contrast to Sec. 2.1 and 2.2, in the following, we change the geometry such that the quasi-1D system is parallel to the x-axis. We are looking for the stationary-state solution for the energy E_F. Expansion into transverse modes yields

$$\psi_\mathrm{I}(x,y) = \sum_{n=0}^{\infty} \left(A_n\, e^{ik_n^\mathrm{I} x} + B_n\, e^{-ik_n^\mathrm{I} x} \right) \phi_n^\mathrm{I}(y), \tag{2.33}$$

$$[1ex]\psi_\mathrm{II}(x,y) = \sum_{n=0}^{\infty} \left(C_n\, e^{ik_n^\mathrm{II} x} + D_n\, e^{-ik_n^\mathrm{II} x} \right) \phi_n^\mathrm{II}(y), \tag{2.34}$$

with modes $\{\phi_n^{\mathrm{I(I)}}\}$ of region I(I), resp. The wave vectors follow from the energy dispersions, $E_n^\mathrm{I}(k_n^\mathrm{I}) = E_n^\mathrm{II}(k_n^\mathrm{II}) = E_\mathrm{F}$. Depending on E_F, modes are either propagating if $\min(E_n) < E_\mathrm{F}$ with real k_n, or *evanescent* if $\min(E_n) > E_\mathrm{F}$, leading to imaginary k_n and thus to exponentially decaying (or growing) wavefunctions. At the interface ($x=0$) the usual boundary conditions have to be satisfied *for all* y,

$$\psi_\mathrm{I}(x=0,y) = \psi_\mathrm{II}(x=0,y), \tag{2.35}$$

$$\hat{v}_x\, \psi_\mathrm{I}(x,y)\big|_{x=0} = \hat{v}_x\, \psi_\mathrm{II}(x,y)\big|_{x=0}, \tag{2.36}$$

requiring a continuous wavefunction and the continuity equation for the probability density, $\partial_t \rho = -\partial_x J_x$, to be fulfilled. The probability current is given by

$$J_x = \frac{1}{2}\left[\psi^* \hat{v}_x \psi + \psi (\hat{v}_x \psi)^*\right], \tag{2.37}$$

[‡]Note that for SO-interacting systems the continuity condition at the interface affects the probability flux; only without SO coupling this reduces to the continuity of the derivative of the wavefunction.

with the velocity operator $\hat{v}_x = \partial H/\partial p_x$ which becomes *non-diagonal* in systems with SO coupling [87].

In a quasi-1D system the continuity conditions (2.35) and (2.36) – which finally give the solution of the Schrödinger equation of the whole system – cannot be fulfilled for all y when the set of transverse modes is restricted to propagating ones only (clearly seen for the two modes sketched in Fig. 2.7). Evanescent modes (EM) have to be included to obtain a sufficiently complete set of transverse wave functions.[§]

Once the solution is found, meaning $\{A_n, B_n, C_n, D_n\}$ in Eq. (2.33) and (2.34) are known, the transmission properties of the system can be derived from the *transfer-matrix* $\hat{T}$, which relates amplitudes on the left to those on right,

$$\begin{pmatrix} \mathbf{A} \\ \mathbf{B} \end{pmatrix} = \hat{T} \begin{pmatrix} \mathbf{C} \\ \mathbf{D} \end{pmatrix}, \quad \text{or equivalently} \quad \begin{pmatrix} \mathbf{B} \\ \mathbf{C} \end{pmatrix} = \hat{S} \begin{pmatrix} \mathbf{A} \\ \mathbf{D} \end{pmatrix}, \tag{2.38}$$

defining the *scattering* or $\hat{S}$*–matrix* which connects incoming and outgoing fluxes.

When addressing the effect of SO coupling on the transmission properties of quasi-1D systems, like the parabolically confined quantum wire in the previous sections, the ansatz for the wavefunctions in (2.33) has to be generalised (i) to include the spin, and (ii) to allow for the peculiarities due the SO coupling like transverse modes depending explicitely on the longitudinal momentum $\hbar k$, making $\phi_{k,n}(y) \neq \phi_{-k,n}(y)$, and the multitude of possible wave vectors for a given energy due to non-parabolicities of the dispersion (Fig. 2.6). The real inconvenience, however, is the determination of EM. The parabolic QWR with SO coupling in the previous sections exemplifies the general non-integrability of the transverse Schrödinger equation, $H(k)\,\phi_k = E_k\,\phi_k$, see Eq. (2.5). Therefore, the determination of *propagating modes* for energy E_F corresponds to numerically finding those *real* k_n such that E_F is contained in the spectrum of $H(k_n)$. On the contrary, *EM* have in general *complex* wave vectors, thus drastically complicating the numerical evaluation of the spectrum of $H(k)$. Although challenging, but technically still feasible, in the context of spintronics to our knowledge no exact investigation of the properties of EM has been performed within the above scheme yet.

Evanescent modes are localised close to the interface between adjacent sections of the quasi-1D system due to their exponential character. Therefore they do not extend over the whole system, leading one to naively believe they have no influence on the transmission characteristics. However, in confined systems the boundary conditions couple propagating and EM which aquire a non-zero amplitude in the superposition (2.33) at the expense of the propagating ones; thus they do affect the transmission properties indirectly.

[§] We remark that the diagonalisation of a tight-binding model is exact within the dimension of the lattice, the solution naturally includes evanescent modes.

This influence of EM has been highlighted in quasi-1D systems without SO coupling by e.g. showing that the localisation of EM around defects may lead to perfect transparency or opaqueness as a function of Fermi energy [85]. Since EM are a basic wave phenomenon, their influence also appears in other fields of physics like microwave waveguides and near-field optics [88, 89].

Because of the complications in finding EM in SO-coupled systems, normally approximations are being applied to make the Hamiltonian integrable. In Sec. 2.2.1 the longitudinal-SO approximation and the two-band model are presented as examples. Within the latter approximation, Governale & Zülicke [69] showed that in a quasi-1D hybrid system of waveguides with different strengths of SO coupling, scattering to EM leads to spin accumulation close to the interface, thus highlighting the general importance of EM.

The results which are derived by the mode matching analysis so far depend very much on the applied approximation. For instance, Wang *et al.* studied periodically stubbed waveguides as an extension of the Datta & Das [42] spin-FET design. They applied the longitudinal-SO approximation for single [44] and multi-subband [90] transmission, and found a tuneable spin current modulation similar to the original spin-FET. Later, Wang & Vasilopoulos [45] extended the calculation by applying the two-band model and found that the previously neglected subband mixing leads to drastic changes of the transmission properties.

2.3.2 Strict-1D limit of a quantum wire

In this section, we treat the strict-1D limit of a ballistic QWR (1D-QWR) by truncating the Hilbert space to its lowest transverse subband. This is a reasonable approximation for the case of strong lateral confinement where the subband separation is the dominating energy scale and the SO coupling is weak.

In this limit, the Hamiltonian of a 1D-QWR is given by

$$H_{1\mathrm{D}} - E_0 = \begin{pmatrix} \frac{1}{2m}p_x^2 + \frac{1}{2}g\mu_{\mathrm{B}}B & \frac{i}{\hbar}\alpha p_x \\ -\frac{i}{\hbar}\alpha p_x & \frac{1}{2m}p_x^2 - \frac{1}{2}g\mu_{\mathrm{B}}B \end{pmatrix}, \tag{2.39}$$

where the effect of a constant electrostatic background potential is absorbed into the energy offset E_0.

In the following, we will demonstrate for the basic example of the 1D-QWR how the electronic transport is influenced when magnetic field and SO coupling act simultaneously in the wire. In this strict-1D limit there is no problem associated with the finding of EM. For the case of a periodic magnetic modulation, we show that a commensurability effect appears in the spin-dependent conductance when the modulation period becomes comparable with the SO-induced spin precession length.

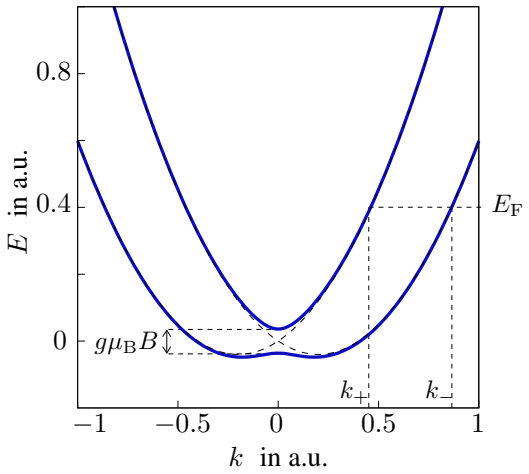

Figure 2.8: Dispersion relation for the spin-orbit interacting Zeeman-split strict-1D quantum wire. Dashed curves correspond to the zero magnetic field case.

Constant magnetic field

For further simplification, we start with the eigenfunctions when all parameters (magnetic field B, SO coupling α, and electrostatic potential E_0) are constant,

$$\psi_{ks}(x) = N_{ks}\, e^{ikx} \begin{pmatrix} \xi_{ks} \\ 1 \end{pmatrix}, \quad s = \pm 1, \tag{2.40}$$

with normalisation constant N_{ks} and

$$\xi_{ks} = \frac{i}{k}\left(\kappa + s\sqrt{k^2+\kappa^2}\right), \quad \kappa := \frac{g\mu_B B}{2\alpha}. \tag{2.41}$$

The corresponding eigenenergies are

$$E_{ks} - E_0 = \frac{\hbar^2}{2m}\left(k^2 + 4s\,k_{SO}\sqrt{k^2+\kappa^2}\right), \quad k_{SO} := \frac{m\alpha}{2\hbar^2}. \tag{2.42}$$

In Fig. 2.8 the dispersion (2.42) is shown. The wavenumber of an electron with Fermi energy E_F in branch s is given by

$$k_s = \pm\sqrt{2}\sqrt{k_F^2 + 4k_{SO}^2 - 2sk_{SO}\sqrt{2k_F^2 + 4k_{SO}^2 + \kappa^2}}, \tag{2.43}$$

where $k_F^2 := (E_F - E_0)m/\hbar^2$. Depending on the Fermi energy, electrons are either propagating (k_s real) or evanescent (k_s imaginary).

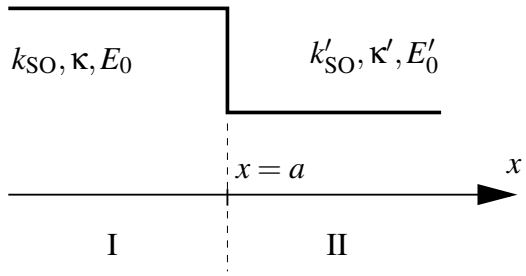

Figure 2.9: Stepwise constant external fields which change at a single interface.

We mention that neither the eigenenergy nor the wavenumber depend on the sign of the magnetic field. Solely the representation of the spinor in the basis of σ_z changes. For a sign change of the magnetic field ($\kappa \to -\kappa$), from (2.41) follows

$$\xi_{k,+}(-\kappa) = -\xi_{k,-}(\kappa) = \xi^*_{k,-}(\kappa), \tag{2.44}$$

$$\xi_{k,-}(-\kappa) = -\xi_{k,+}(\kappa) = \xi^*_{k,+}(\kappa). \tag{2.45}$$

Transport in the presence of a magnetic modulation

We now address the question how the transport properties of the 1D-QWR is affected by a modulation of the external parameters (B, α, E_0). Experimentally this could be done by e.g. magnetic superlattices [91,92] which modulate periodically the strength of the magnetic field. We will concentrate on system parameters corresponding to such an experimental situation with weak magnetic modulation and SO coupling compared to Fermi energy. Generalisation to other parameter regimes is straightforward. Although results will be presented only for magnetic modulation, the formulation of the transmission problem will be outlined for arbitrary changes of external parameters. In a ballistic 1D system which is connected to leads the conductance is related to the transmission properties of the system via the Landauer formular [93,94].

$$G = G_0 \sum_{nn',\sigma\sigma'} \left| t_{n\sigma\to n'\sigma'} \right|^2, \quad G_0 = \frac{e^2}{h}, \tag{2.46}$$

where $t_{n\sigma\to n'\sigma'}$ is the probability amplitude for transmission from state $(n\sigma)$ in the source lead to state $(n'\sigma')$ in the drain lead. In the following, we will restrict ourselves to calculating these transmission amplitudes.

We start with considering the transport through a single interface (located at $x = a$) between regions with different parameters k_{SO}, κ, E_0, see Fig. 2.9. The transmission properties of the interface can be calculated analogously to textbook

quantum mechanics. Nevertheless, here, we go through the basic calculation to illustrate peculiarities arising from the SO coupling.

The solution of the Schrödinger equation can be obtained by using the ansatz

$$\begin{aligned} \text{I:} \qquad \psi_{\mathrm{I}}(x) =& A_+\psi_{k_+}(x) + A_-\psi_{k_-}(x) \\ &+ B_+\psi_{-k_+}(x) + B_-\psi_{-k_-}(x), \end{aligned} \tag{2.47}$$

$$\begin{aligned} \text{II:} \qquad \psi_{\mathrm{II}}(x) =& C_+\psi_{k'_+}(x) + C_-\psi_{k'_-}(x) \\ &+ D_+\psi_{-k'_+}(x) + D_-\psi_{-k'_-}(x), \end{aligned} \tag{2.48}$$

with the wave vectors of the left and right region, $k_\pm = k_\pm(\kappa, k_{\mathrm{SO}}, E_0)$ and $k'_\pm = k_\pm(\kappa', k'_{\mathrm{SO}}, E'_0)$, respectively. At the interface the conditions (2.35) and (2.36) have to be satisfied which for a strict-1D system reduce to

$$\psi_{\mathrm{I}}(x=a) = \psi_{\mathrm{II}}(x=a), \tag{2.49}$$

$$\hat{v}_x\psi_{\mathrm{I}}(x)\big|_a = \hat{v}_x\psi_{\mathrm{II}}(x)\big|_a, \tag{2.50}$$

with the *non-diagonal* velocity operator

$$\hat{v}_x = \frac{\partial H}{\partial p_x} = \frac{1}{m}\begin{pmatrix} p_x & 2i\hbar k_{\mathrm{SO}} \\ -2i\hbar k_{\mathrm{SO}} & p_x \end{pmatrix}. \tag{2.51}$$

In transport calculations it is customary to normalise the wavefunctions with respect to the probability current. Therefore, we require

$$\left|\langle\psi_{ks}|\hat{v}_x|\psi_{ks}\rangle\right| = 1, \tag{2.52}$$

leading to the normalisation constant

$$N_{ks} = \frac{1}{\sqrt{L}}\sqrt{\frac{m|k|/2\hbar}{\left(k^2+\kappa^2+2k_{\mathrm{SO}}\kappa + s(\kappa+2k_{\mathrm{SO}})\sqrt{k^2+\kappa^2}\right)}}, \tag{2.53}$$

where the length of the wire is denoted by L. Equations (2.49) and (2.50) lead to the transfer matrix $M(a)$ through the magnetic step,

$$\mathcal{N}\begin{pmatrix} A_+ \\ A_- \\ B_+ \\ B_- \end{pmatrix} = \underbrace{\Psi(-a)\hat{m}^{-1}\hat{m}'\Psi'(a)}_{=:M(a)}\mathcal{N}'\begin{pmatrix} C_+ \\ C_- \\ D_+ \\ D_- \end{pmatrix}, \tag{2.54}$$

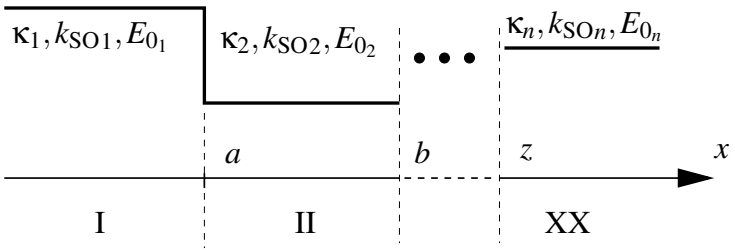

Figure 2.10: System of stepwise constant external fields with multiple interfaces.

with the normalisation matrix

$$\mathcal{N} = \begin{pmatrix} N_{k_+} & 0 & 0 & 0 \\ 0 & N_{k_-} & 0 & 0 \\ 0 & 0 & N_{k_+} & 0 \\ 0 & 0 & 0 & N_{k_-} \end{pmatrix}, \tag{2.55}$$

and the matrix of phase coefficients

$$\Psi_\kappa(a) = \begin{pmatrix} e^{ik_+a} & 0 & 0 & 0 \\ 0 & e^{ik_-a} & 0 & 0 \\ 0 & 0 & e^{-ik_+a} & 0 \\ 0 & 0 & 0 & e^{-ik_-a} \end{pmatrix}, \tag{2.56}$$

$$\hat{m} = \begin{pmatrix} \xi_{k_+} & \xi_{k_-} & -\xi_{k_+} & -\xi_{k_-} \\ 1 & 1 & 1 & 1 \\ \phi_{k_+} & \phi_{k_-} & \phi_{k_+} & \phi_{k_-} \\ \theta_{k_+} & \theta_{k_-} & -\theta_{k_+} & -\theta_{k_-} \end{pmatrix}, \tag{2.57}$$

where $\phi_{ks} = k\xi_{ks} + 2ik_{SO}$ and $\theta_{ks} = k - 2ik_{SO}\xi_{ks}$.

In the case of multiple interfaces between regions of stepwise constant parameters (see Fig. 2.10), one obtains the transfer matrix $\hat{T}$ of the entire system by connecting the transfer matrices $M_i(x_i)$ of the separate interfaces,

$$\mathcal{N} \begin{pmatrix} A_+ \\ A_- \\ B_+ \\ B_- \end{pmatrix} = \underbrace{M_1(a)M_2(b)\ldots M_n(z)}_{=:\hat{T}} \mathcal{N}_n \begin{pmatrix} X_+ \\ X_- \\ Y_+ \\ Y_- \end{pmatrix}. \tag{2.58}$$

From this matrix the transmission coefficients for the different spin polarisations are derived easily. We now restrict ourselves to the assumption that all *incoming* electrons are right-moving in state ψ_{k_+} (i.e. $A_- = Y_+ = Y_- = 0$). Because

of our condition of normalisation (2.52), the transmission and reflection coefficients, $T := |J_{\text{trans}}/J_{\text{inc}}|$ and $R := |J_{\text{refl}}/J_{\text{inc}}|$, directly follow from the expansion coefficients in Eq. (2.47) and (2.48). For instance, the probability for an incoming electron in state ψ_{k_+} to pass the interfaces of the modulated region without changing its spin state is given by $T_{++} = |t_{++}|^2$, where the transmission amplitude is given by

$$t_{++} = \frac{X_+}{A_+} = \frac{N_{k_+}}{N_{k'_+}} \frac{T_{22}}{T_{11}T_{22} - T_{12}T_{21}}, . \tag{2.59}$$

Analogously follows for the probability amplitude to flip the incoming spin while passing the modulation region

$$t_{+-} = \frac{X_-}{A_+} = -\frac{N_{k_+}}{N_{k'_-}} \frac{T_{21}}{T_{11}T_{22} - T_{12}T_{21}}, \tag{2.60}$$

the reflection without spin flip

$$r_{++} = \frac{B_+}{A_+} = \frac{T_{31}T_{22} - T_{32}T_{21}}{T_{11}T_{22} - T_{12}T_{21}}, \tag{2.61}$$

and the reflection with spin flip

$$r_{+-} = \frac{B_-}{A_+} = \frac{N_{k_+}}{N_{k_-}} \frac{T_{41}T_{22} - T_{42}T_{21}}{T_{11}T_{22} - T_{12}T_{21}}. \tag{2.62}$$

For incoming electrons which are "$-$"-polarised follows

$$t_{-+} = \frac{X_+}{A_-} = -\frac{N_{k_-}}{N_{k'_+}} \frac{T_{12}}{T_{11}T_{22} - T_{12}T_{21}}, \tag{2.63}$$

$$t_{--} = \frac{X_-}{A_-} = \frac{N_{k_-}}{N_{k'_-}} \frac{T_{11}}{T_{11}T_{22} - T_{12}T_{21}}, \tag{2.64}$$

$$r_{-+} = \frac{B_+}{A_-} = \frac{N_{k_-}}{N_{k_+}} \frac{T_{32}T_{11} - T_{31}T_{12}}{T_{11}T_{22} - T_{12}T_{21}}, \tag{2.65}$$

$$r_{--} = \frac{B_-}{A_-} = \frac{T_{42}T_{11} - T_{41}T_{12}}{T_{11}T_{22} - T_{12}T_{21}}. \tag{2.66}$$

Numerical results

In principle, the transmission properties of a 1D-QWR with arbitrarily changing external parameters (B, α, E_0) can be calculated by discretisation and the application of Eq. (2.58).

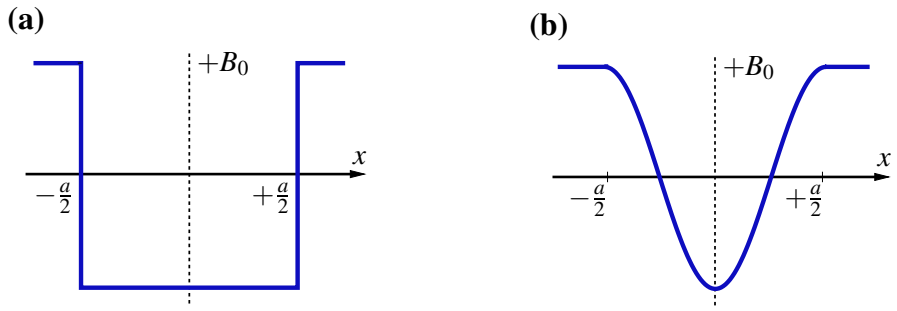

Figure 2.11: Models of magnetic barriers: rectangular (a) and sinusoidal (b).

In the following, we show results for the transport through magnetic barriers with rectangular and sinusoidal modulation. Both cases show a commensurability effect when the modulation period becomes comparable to the SO-induced spin precession length. Here, we restrict ourselves to Fermi energies much higher than the gap in the dispersion in Fig. 2.8. Following the experimental motivation of magnetic superlattices, we assume weak magnetic modulation ($\sim 25\,\mathrm{mT}$).

First, we consider a simple rectangular barrier (Fig. 2.11a) of width a where

$$\mathbf{B} = \begin{cases} +B_0\,\hat{\mathbf{e}}_z & \text{for } |x| > a/2, \\ -B_0\,\hat{\mathbf{e}}_z & \text{for } |x| < a/2. \end{cases} \tag{2.67}$$

(The SO coupling strength and electrostatic potential is assumed to be constant.)

Although the flip of the magnetic field direction in the barrier does not change eigenenergies and wave vectors, it does change the eigenstates, see Eq. (2.44). Therefore, when injecting right-moving electrons with spin σ, in perfect analogy to the standard spinFET [42], the probability to find the same spin directly behind the barrier is a periodic function of the barrier width, corresponding to spin precession with period $a_0 = 2\pi/|k_+ - k_-|$, by Eq. (2.47) and (2.48). If the parameters κ and k_{SO} are small at the scale of Fermi energy this period becomes $a_0 \approx \pi/2k_{\mathrm{SO}}$.

In Fig. 2.12 the numerically calculated coefficients for spin-dependent transmission are shown for a single barrier and a modulation with 10 rectangular periods in series. For the used parameters with weak SO coupling the spin precession period corresponds to $a_0 \approx 0.33\,\mu\mathrm{m}$, being within range of state-of-the-art experimental technique. For the case a of single barrier (panel a+b) the effect of spin precession is seen as a reduction of the spin conserving transmission $T_{\sigma\sigma}$ when the barrier width becomes commensurate with half of the spin precession length.

This commensurability effect is most clearly seen in the narrow dip in the spin-conserving transmission. At a barrier width such that $ak_{\mathrm{SO}}/\pi = 1/4$ injected electrons with polarisation "$\pm$" are rotated to "$\mp$" while propagating through the barrier and thus not matching the wavefunction of the region behind the barrier.

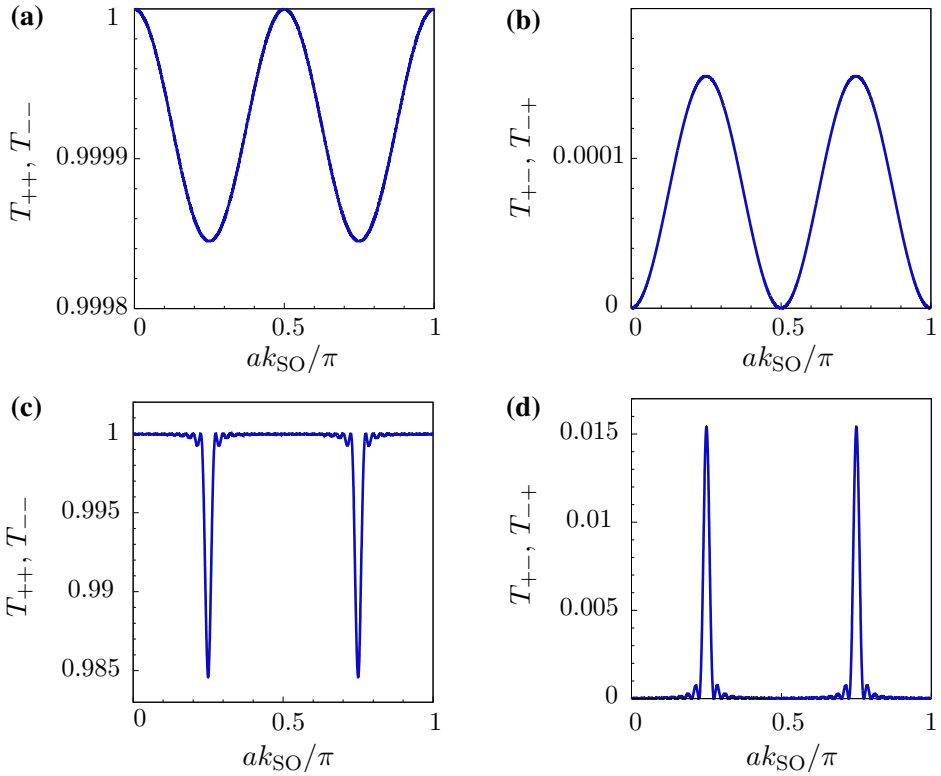

Figure 2.12: Transmission coefficients for a rectangular magnetic barrier [**(a)**+**(b)**] and 10 barriers in series [**(c)**+**(d)**] for weak spin-orbit coupling as a function of the barrier width a. System parameters: $E_{\mathrm{F}} = 48\,\mathrm{meV}$, $B_0 = 25\,\mathrm{mT}$, $\alpha = 1.6 \times 10^{-11}\,\mathrm{eVm}$, $g = -15$, $m = 0.042 m_0$.

Thus, the spin-conserved transmission channel $T_{\sigma\sigma}$ is reduced. In the original spinFET design with ferromagnetic leads [42], only majority spin carriers are injected to and absorbed from the SO interacting region, leading to a strong modulation of the current as a function of the SO coupling. In our model of a 1D-QWR with a periodic magnetic modulation, this selection of carriers is relaxed. Since the amplitude of modulation is chosen to be small ($B = 25\,\mathrm{mT}$), the reduction of spin-conserving transmission through a single barrier is also small. However, successive transmission through multiple periods enhances the signal. Figure 2.12c+d show the spin-dependent transmission coefficients for 10 periods of rectangular modulation, clearly showing a commensurability effect of $\sim 2\,\%$. By using magnetic superlattices the number of periods can easily exceed a few hundreds, leading to the expectation of a significant reduction of transmission at commensurability $ak_{\mathrm{SO}}/\pi = 1/4$.

For weak SO coupling the dominating Fourier component of the transmission coefficients can be approximated in lowest order by

$$T_{++} \approx T_{--} \approx 1 - \bar{\kappa}^2 \left[1 - \cos a(k_- - k_+)\right], \tag{2.68}$$

$$T_{+-} \approx T_{-+} \approx \bar{\kappa}^2 \left[1 - \cos a(k_- - k_+)\right], \tag{2.69}$$

where $\bar{\kappa} := \kappa / k_{\mathrm{F}}$. The oscillations in the reflection probabilities $R_{\sigma\sigma'}$ (not shown here) are orders of magnitude smaller and carry also higher Fourier components (e.g. periods π/k_σ) as a signal of standard Fabry–Perot like interference of the *orbital* wavefunction. In the chosen regime with weak SO coupling and magnetic field, apart from the small deviations due to reflection, the barrier is almost perfectly conducting since $T_{++} + T_{+-} = T_{--} + T_{-+} \approx 1$ by Eq. (2.68) and (2.69). The oscillating features in the *spin-resolved* transmission in Fig. 2.12a+b clearly originate from the interference of the spinors which is driven by the spin precession.

We remark that in order to actually resolve the commensurability effect in the transmission a *spin-dependent measurement* is needed. Without being sensitive to the spin, the *total* transmission $T := \sum_{\sigma\sigma'} T_{\sigma\sigma'}$ shows only standard Fabry–Perot like interference on the scale of the Fermi wavelength, $1/k_{\mathrm{F}} \ll a_0$.

We point out that due symmetry properties of the scattering matrix of the system no polarisation effect in the transmitted electron flux can be expected. For a detailed symmetry analysis see Ref. [58].

In the context of magnetic superlattices, a sinusoidal modulation matches more realistically the experimental situation. Figure 2.13a+b shows the spin-dependent transmission coefficients for a cosine-shaped magnetic barrier (see Fig. 2.11b) of width a where the magnetic field is

$$\mathbf{B} = \begin{cases} +B_0\,\hat{\mathbf{e}}_z & \text{for } |x| > a/2, \\ -B_0\,\hat{\mathbf{e}}_z \cos 2\pi \dfrac{x}{a} & \text{for } |x| < a/2. \end{cases} \tag{2.70}$$

In contrast to the result for a rectangular barrier, the reduction of the spin-conserving transmission is not a periodic feature with increasing barrier width due to the non-constant modulation. In panel c+d the results for transmission through 10 sinusoidal periods are shown. Again, the reduction of $T_{\sigma\sigma}$ is strongly enhanced by cumulating a small effect when successively passing consecutive barriers.

2.4 Summary

In this chapter, the interplay of spin-orbit (SO) coupling and geometrical confinement in quasi-one-dimensional quantum wires (QWRs) in perpendicular magnetic

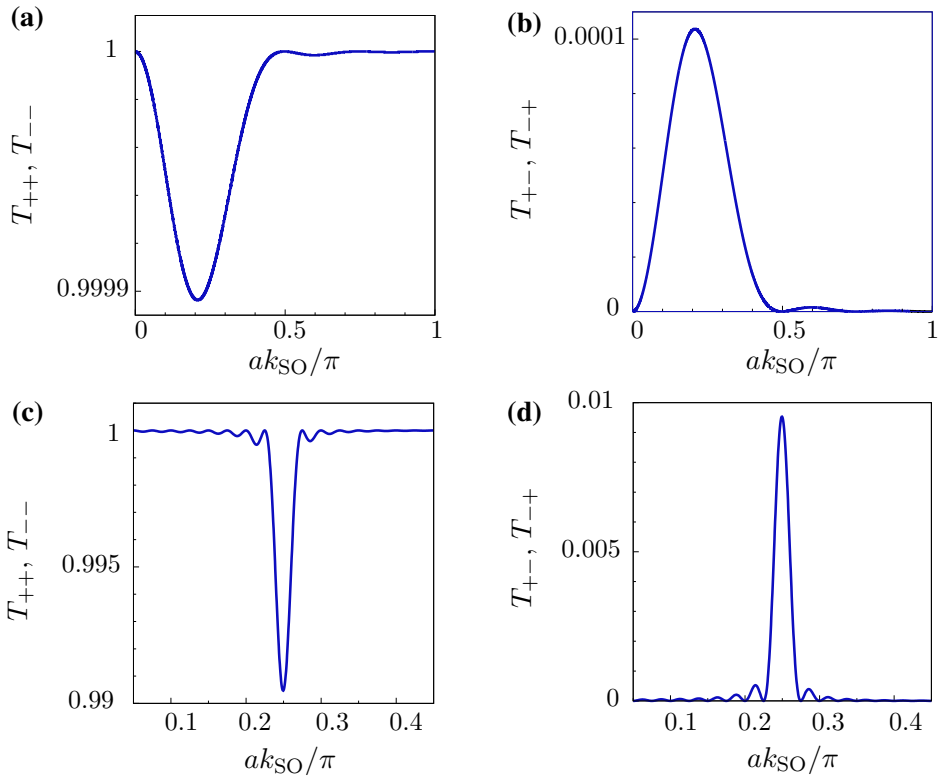

Figure 2.13: Transmission coefficients for a sinusoidal magnetic barrier [**(a)+(b)**] and 10 barriers in series [**(c)+(d)**] for weak spin-orbit coupling as a function of the barrier width a. System parameters: $E_{\mathrm{F}} = 48\,\mathrm{meV}$, $B_0 = 25\,\mathrm{mT}$, $\alpha = 1.6 \times 10^{-11}\,\mathrm{eVm}$, $g = -15$, $m = 0.042 m_0$.

field has been investigated. In general, SO interaction couples the spin of an electron to its orbital motion. Thus, confinement induced quantisation of motion is expected to influence the spin properties. A magnetic field which is perpendicular to the plane of motion is a further quantity, affecting both orbitals and spin.

In Sec. 2.1 and 2.2, we have presented a detailed analysis of the one-electron spectral and spin properties of the QWR for various regimes in the interplay of confinement, SO coupling and magnetic field. Spectra and spin densities show features which are governed by a compound spin orbital-parity symmetry of the QWR. Without magnetic field, this *spin parity* – which is a characteristic property of any symmetrically confined quasi-1D system with Rashba effect – is shown to replace the quantum number of spin. It is also responsible for the well-known degeneracy at $k = 0$ in symmetrically confined systems with Rashba effect. A non-vanishing magnetic field breaks the spin-parity symmetry, thus lifting the corresponding degeneracy at $k = 0$. We show that this magnetic field induced energy

splitting can become much larger than the Zeeman splitting and should be accessible experimentally by means of optical or transport measurements. In addition, hybridisation effects of the spin density go along with the symmetry breaking.

The one-electron spectrum is shown to be very sensitive to weak magnetic fields. SO-induced modifications of the subband structure of the QWR are strongly altered when the magnetic length becomes comparable to the confinement. This might imply consequences for spin transistor designs which depend on spin injection from ferromagnetic contacts because of magnetic stray fields.

In Sec. 2.3 we have outlined the method of mode matching analysis for the evaluation of transport properties in quasi-1D system with SO coupling. In this context we have shown that the inclusion of evanescent modes is crucial to end up with reliable results. In SO-interacting quasi-1D systems, the determination of evanescent modes is complicated due to the structure of Hamiltonian. To our knowledge, a detailed treatment of this problem is still lacking despite its importance for assessing the approximations which are usually employed.

In Sec. 2.3.2 we analysed the spin-dependent transmission properties of a strict-1D QWR with a single transverse subband in the interplay of SO coupling and external magnetic modulation. A commensurability effect is found when the period of modulation is comparable to the SO-induced spin precession.

For the example of the QWR we have demonstrated that in the case of parabolic confinement it is useful to map the underlying one-electron model onto a bosonic representation, which highlights the effects of SO coupling in confined systems. For large magnetic fields this representation shows many similarities to matter-light interaction in quantum optics. In the next chapter of this thesis a similar mapping will be applied to the model of a parabolically confined quantum dot.

Chapter 3

Rashba spin-orbit coupling in quantum dots

In the previous chapter we have derived an analogy between parabolically confined spin-orbit (SO) interacting quantum wires and quantum optics. This analogy amounts to the exact correspondence between the two-dimensional (2D) SO-coupled system and the Jaynes-Cummings model (JCM) that was introduced in Sec. 1.3. Apart from being integrable, this model is known to exhibit a number of striking quantum optical phenomena like Rabi oscillations and the collapse and revival of wavefunctions [33]. The origin of these effects is the periodic flux of excitation energy between atom and light field.

With this analogy in mind, one could ask whether it is possible to observe similar phenomena in a SO-coupled system? Clearly, it is not feasible to coherently manipulate the vast number of electrons in a 2D system to exhibit synchronous Rabi oscillations. This is in contrast to quantum optics where stimulated emission in active media can lead to collective effects by coupling to the same light field (laser). In the solid-state counterpart, the electrons do not share a common boson field. Therefore, the number of carriers has to be reduced drastically, e.g. by using quantum dots. In these quasi-zero-dimensional systems the number of electrons can be reduced to the single particle limit – making it the optimal object to study SO-induced effects on the single-electron spectra and dynamics.

It is the purpose of this chapter to elucidate the effects of SO coupling on few-electron quantum dots. Motivated by the quest for SO-driven Rabi oscillations we show that for weak SO coupling the dot can effectively be described by the JCM with the roles of atomic pseudo-spin and light field played by the spin and orbital angular momentum of the electron, respectively. This effective model leads to characteristic anticrossings in the single-particle spectra, any of which can be interpreted as a two-level system (TLS) which describes the periodic exchange of energy between spin and orbital degree of freedom, thus forming a novel compos-

ite spin-angular momentum qubit. The experimental observation of anticrossings would be a verification of the JCM and would allow the determination of the strength of the SO coupling in quantum dots. In addition, we propose an experimentally feasible scheme to observe genuine Rabi oscillations in any of the TLS by simply measuring the electronic transport through the dot.

This chapter is organised as follows: In the next section the scientific publication which comprises the main results of our studies of the SO driven coherent oscillations is presented. In Sec. 3.2 we provide more background information by giving an introduction to few-electron quantum dots and reviewing the effects of SO coupling therein in Sec. 3.2.1 and 3.2.2, presenting the rigorous derivations of the published results, and discussing the effects of relaxation on the coherent evolution of the dot in Sec. 3.3.

3.1 Spin-orbit driven coherent oscillations in a few-electron quantum dot*

Abstract: We propose an experiment to observe coherent oscillations in a single quantum dot with the oscillations driven by spin-orbit interaction. This is achieved without spin-polarised leads, and relies on changing the strength of the spin-orbit coupling via an applied gate pulse. We derive an effective model of this system which is formally equivalent to the Jaynes–Cummings model of quantum optics. For parameters relevant to a InGaAs dot, we calculate a Rabi frequency of 2 *GHz.*

Motivated by the desire for a closer understanding of quantum coherence and by the drive to develop novel quantum computing architecture, a number of breakthrough solid-state experiments have focused on coherent oscillations — the back and forth flopping of that most fundamental of quantum objects, the two-level system [6,7,95,96]. The pioneering work of Nakamura *et al.* with the coherent superposition of charge states of a Cooper-pair box [6] first demonstrated the possibility of observing such oscillations in a wholly solid-state device; thus sparking the remarkable progress in qubit development in super-conducting systems [95, 96].

The important double quantum dot experiment of Hayashi and co-workers [7] showed that coherent oscillations could also be observed in normal semiconductor systems. It is the purpose of this paper to propose an experiment in which coherent oscillations are observed in a *single quantum dot* (QD), with these oscillations being driven by the spin-orbit (SO) interaction.

*This section has been submitted to publication. E-print: S. Debald and C. Emary, cond-mat/0410714 at www.arxiv.org.

The SO interaction in semiconductor heterostructures has its origin in the breaking of inversion symmetry, and is increasingly coming to be seen as a tool with which to manipulate electronic states, see e.g. [38, 39]. The grandfather of these ideas is the spin-transistor of Datta and Das [42], in which the SO interaction causes electron spins to precess as they move through a two-dimensional electron gas (2DEG). In materials where the structural inversion asymmetry dominates, e.g. InGaAs, the SO interaction can be described by the Rashba Hamiltonian [11, 12]

$$H_{\mathrm{SO}} = -\frac{\alpha}{\hbar}\left[(\mathbf{p}+\frac{e}{c}\mathbf{A})\times\boldsymbol{\sigma}\right]_z . \tag{3.1}$$

In this letter we consider the effects of H_{SO} on electrons in a small, few-electron lateral quantum dot. Although such dots are yet to be realised in materials with strong SO coupling, there is currently a considerable effort to develop nanostructures in such materials [37]. Our interest here is not in open or chaotic QDs [97–100], but rather in small dots in the Coulomb blockade regime.

Such dots have been studied by a number of authors [101–107], but our analysis differs in a crucial respect: by making an analogy with quantum optics, we are able to derive an approximate Hamiltonian that captures the essential physics of the dot. This model is formally identical to the Jaynes–Cummings (JC) model [32], first derived in the context of the atom-light interaction. Here, the roles of the atomic pseudo-spin and light field are played by the spin and orbital angular momentum of the electron respectively. The system then naturally decomposes into a set of two-level systems (TLS), any of which may be considered as the qubit degree of freedom within which coherent oscillations can occur. These oscillations are genuine Rabi oscillations [33], with orbital and spin degrees of freedom exchanging excitation. This "spin-orbit pendulum" behaviour has been noted in three-dimensional models in nuclear physics [78, 79].

Having elucidated the origin and properties of the TLS, we then describe an experimental scheme through which the coherent oscillations can be investigated. The key problem here is that of injecting into, and reading out from, states which are not eigenstates of the SO coupled system. In the Hayashi experiment [7], this was achieved through the spatial separation of the two dots, which makes the leads couple to the localised left and right states, rather than to the bonding and antibonding eigenstates. In our single dot system, the direct analogy of this would be the injection of spin-polarised electrons. Given the difficulty of interfacing ferromagnetic leads with semiconductors [37], we avoid their use by exploiting the fact that the strength of the SO interaction can be controlled by external gates [24, 25, 27].

Our starting point is the Fock-Darwin theory of a single electron in a 2DEG

with parabolic confinement of energy $\hbar\omega_0$ [108],

$$H_0 = \frac{(\mathbf{p}+\frac{e}{c}\mathbf{A})^2}{2m} + \frac{m}{2}\omega_0^2(x^2+y^2), \tag{3.2}$$

where m is the effective mass of the electron. Applying a perpendicular magnetic field in the symmetric gauge, in second quantised notation we have

$$H_0 = \hbar\widetilde{\omega}(a_x^\dagger a_x + a_y^\dagger a_y + 1) + \frac{\hbar\omega_c}{2i}(a_y a_x^\dagger - a_x a_y^\dagger), \tag{3.3}$$

with $\omega_c \equiv eB/mc$ and $\widetilde{\omega}^2 \equiv \omega_0^2 + \omega_c^2/4$. Introduction of $a_\pm = 2^{-1/2}(a_x \mp i a_y)$ decouples the system into eigenmodes of frequency $\omega_\pm = \widetilde{\omega} \pm \omega_c/2$.

We now include the Rashba interaction of Eq. (3.1), for which the coupling strength α is related to the spin precession length $l_{\rm SO} \equiv \hbar^2/2m\alpha$. With magnetic length $l_B \equiv \sqrt{\hbar/m\omega_c}$, we have

$$H_{\rm SO} = \frac{\alpha}{\tilde{l}}\left[\gamma_+(a_+\sigma_+ + a_+^\dagger\sigma_-) - \gamma_-(a_-\sigma_- + a_-^\dagger\sigma_+)\right], \tag{3.4}$$

with coefficients $\gamma_\pm \equiv 1 \pm \frac{1}{2}\left(\tilde{l}/l_B\right)^2$ and $\tilde{l} \equiv \sqrt{\hbar/m\widetilde{\omega}}$.

Adding the Zeeman term, in which we take g to be negative as in InGaAs, performing a unitary rotation of the spin such that $\sigma_z \to -\sigma_z$ and $\sigma_\pm \to -\sigma_\mp$, and rescaling energies by $\hbar\omega_0$ we arrive at the Hamiltonian

$$\begin{aligned} H = {} & \omega_+ a_+^\dagger a_+ + \omega_- a_-^\dagger a_- + \frac{1}{2}E_z\sigma_z \\ & + \frac{l_0^2}{2\tilde{l}\,l_{\rm SO}}\left[\gamma_-(a_-\sigma_+ + a_-^\dagger\sigma_-) - \gamma_+(a_+\sigma_- + a_+^\dagger\sigma_+)\right], \end{aligned} \tag{3.5}$$

where $l_0 = \sqrt{\hbar/m\omega_0}$ is the confinement length of the dot and $E_z = |g|m/2m_{\rm e}(l_B/l_0)^2$ is the Zeeman energy with $m_{\rm e}$ the bare mass of the electron.

This single-particle picture is motivated by the good agreement between Fock-Darwin theory and experiment in the non-SO case [108], and by studies which have shown that many-body effects in QDs play only a small role at the magnetic fields we consider here [101, 102, 109].

We now derive an approximate form of this Hamiltonian by borrowing the observation from quantum optics that the terms preceded by γ_+ in Eq. (3.5) are counter-rotating, and thus negligible under the rotating-wave approximation [33] when the SO coupling is small compared to the confinement. This decouples the ω_+ mode from the rest of the system, giving $H = \omega_+ n_+ + H_{\rm JC}$ where

$$H_{\rm JC}(\alpha) = \omega_- a_-^\dagger a_- + \frac{1}{2}E_z\sigma_z + \lambda(a_-\sigma_+ + a_-^\dagger\sigma_-), \tag{3.6}$$

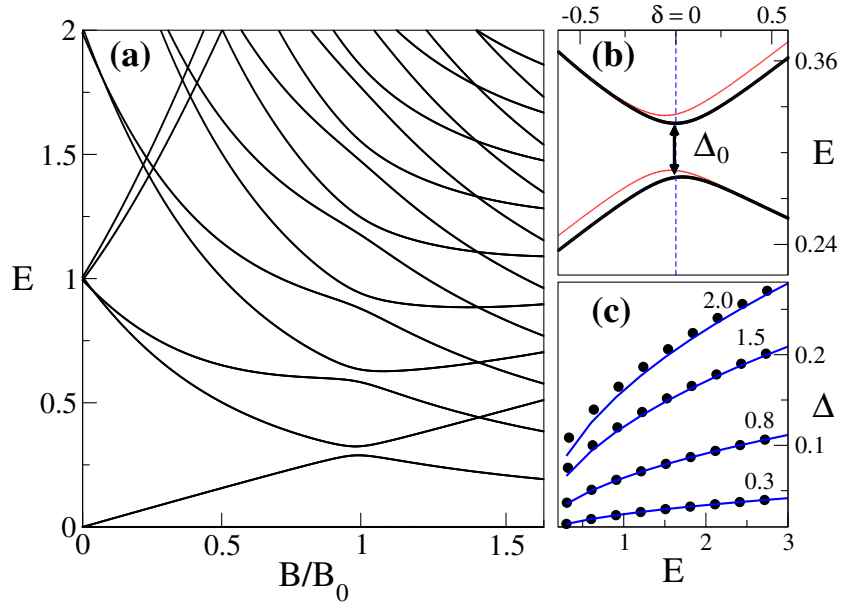

Figure 3.1: Spectral features of Rashba–coupled quantum dot as function of magnetic field. The parameters used are typical of InGaAs: $g=-4$, $m/m_e=0.05$ with dot size $l_0=150\,\mathrm{nm}$. Resonance occurs at $B_0=90\,\mathrm{mT}$. **(a)** Low-lying excitation spectrum for spin-orbit coupling $\alpha=0.8\times10^{-12}\,\mathrm{eVm}$. **(b)** Lowest lying anticrossing. Thick line is JC model showing anticrossing width Δ_0 at $\delta=0$, and thin line is exact numerical result. **(c)** Plot of width Δ_n against central energy of anticrossing with the dot on resonance for different α in the range $0.3-2.0\times10^{-12}\,\mathrm{eVm}$. The exact numerical results (circles) show excellent agreement with the square-root behaviour predicted by the JC model in this α range.

with $\lambda=l_0^2\gamma_-/2\tilde{l}\,l_{\mathrm{SO}}$. This is the well-known Jaynes-Cummings model (JCM) of quantum optics. It is completely integrable, and has ground state $|0,\downarrow\rangle$ with energy $E_{\mathrm{G}}=-E_z/2$ independent of coupling. The rest of the JCM Hilbert space decomposes into two-dimensional subspaces $\{|n,\uparrow\rangle,|n+1,\downarrow\rangle;\quad n=0,1,\ldots\}$. Diagonalisation in each subspace gives the energies $E_\alpha^{(n,\pm)}=(n+1/2)\,\omega_-\pm\Delta_n/2$ with detuning $\delta\equiv\omega_--E_z$ and $\Delta_n\equiv\sqrt{\delta^2+4\lambda^2(n+1)}$. The eigenstates are

$$|\psi_\alpha^{(n,\pm)}\rangle=\cos\theta_\alpha^{(n,\pm)}|n,\uparrow\rangle+\sin\theta_\alpha^{(n,\pm)}|n+1,\downarrow\rangle, \tag{3.7}$$

with $\tan\theta_\alpha^{(n,\pm)}=(\delta\pm\Delta_n)/2\lambda(n+1)^{1/2}$.

Figure 3.1a shows a portion of the excitation spectrum obtained by exact numerical diagonalisation for a typical dot in InGaAs. The approximate H_{JC} de-

scribes the energy levels of the system to within 10% of the typical anticrossing width and 1% of ω_0. This small discrepancy is visible in Fig. 3.1b. In the following, we are only concerned with the lowest-lying energy states in the dots. Without SO interaction, these states are described by $n_+ = 0$ – indicating that the states converge to the lowest Landau level in the high-field limit, and by n_- corresponding to the quantum number of angular momentum. The SO interaction thus couples two states of adjacent angular momentum and opposite spin. The detuning δ uniquely identifies ω_c for fixed material parameters and dot size.

Under the assumptions of the constant interaction model [108], the most important prediction of this model for linear transport is that, with the dot on resonance, the addition-energy spectrum for the first few electrons (up to 18 here) is described by a sequence of well-separated anticrossings, the width of which increases as $\alpha\sqrt{n+1}$. This behaviour is shown in Fig. 3.1c, and its observation would be confirmation of our JC model, and would permit a determination of α in quantum dots.

We now describe the procedure for observing spin-orbit driven Rabi oscillations. Our proposal is somewhat similar to that of Nakamura [6] with a voltage pulse driving the system, but with the crucial difference that the oscillations here are induced, not by a change in the detuning, but by a change in the SO coupling strength. We operate in the non-linear transport regime and address a single two-level system by being near resonance and by tuning the chemical potentials of the leads close to the n-th anticrossing. The SO coupling is set to α_1 and the states taking part in the oscillation are eigenstates of $H_{\mathrm{JC}}(\alpha_1)$, namely $\psi^{\pm}_{\alpha_1}$, which are situated symmetrically around the chemical potential of the right lead μ_R, see Fig. 3.2a. The temperature is taken smaller than the detuning $k_{\mathrm{B}}T \ll \delta$ to avoid the effects of thermal broadening. Assuming Coulomb blockade and considering first-order sequential tunnelling only, electrons can either tunnel from the left lead into the dot via state $\psi^{+}_{\alpha_1}$ and subsequently leave to the right or, alternatively, tunnel to state $\psi^{-}_{\alpha_1}$ blockading the dot, see Fig. 3.2b. Assuming tunnelling through the left/right barrier at a constant rate $\Gamma_{L/R}$, we set $\Gamma_L > \Gamma_R$ to assure that the dot is preferentially filled from the left; thus maximising the current. On average then, the dot will be initialised in state $\psi^{-}_{\alpha_1}$ for times $t_i > \Gamma_R^{-1}$.

Having trapped an electron in this state, we apply a voltage pulse to the gate. This has two effects. Firstly, this change in voltage alters the SO coupling to a new value α_2. Since this change is performed non-adiabatically, the electron remains in the initial eigenstate $\psi^{-}_{\alpha_1}$ until Rabi oscillations begin between this state and $\psi^{+}_{\alpha_1}$ under the influence of the new Hamiltonian $H_{\mathrm{JC}}(\alpha_2)$. Secondly, the TLS is drawn below both chemical potentials, assuring that oscillations can occur without tunnelling out of the dot, see Fig. 3.2c.

After a time t_p, the gate voltage is returned to its initial value, and the TLS resumes both to its original position and coupling α_1, as in Fig. 3.2d. Tunnelling

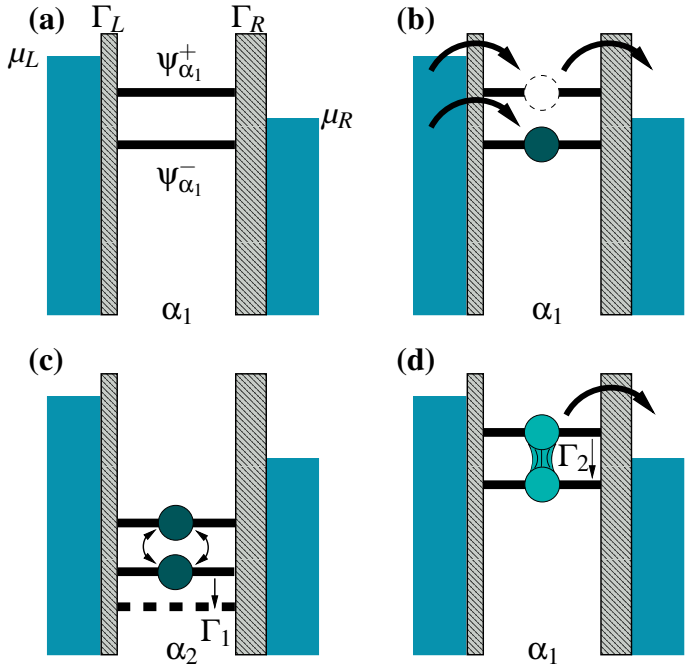

Figure 3.2: Configuration of the dot in the various stages of the cycle. **(a)** The positions of the dot levels $\psi^{\pm}_{\alpha_1}$, chemical potentials $\mu_{L,R}$, and the tunnelling rates $\Gamma_L > \Gamma_R$. **(b)** The coupling is initially α_1. On average, for times $t_i > \Gamma_R^{-1}$ the dot will be initialised in state $\psi^-_{\alpha_1}$. **(c)** The applied voltage pulse lowers the dot levels and non-adiabatically changes the coupling to $\alpha_2 \neq \alpha_1$, thus inducing Rabi oscillations. **(d)** Pulse is switched off after time t_p and the levels return to their initial places. Tunnelling to right occurs when the electron has oscillated into upper state. Relaxation rates $\Gamma_{1,2}$ are also shown.

out of the dot can now occur, provided that the electron is found in the upper state, which happens with a probability given by the overlap of the oscillating wave function at time t_p with the upper level,

$$P(t_p) = |\langle \psi^+_{\alpha_1} | \Psi(t_p) \rangle|^2 = |\langle \psi^+_{\alpha_1} | e^{-iH(\alpha_2)t_p} | \psi^-_{\alpha_1} \rangle|^2. \tag{3.8}$$

This process is operated as a cycle and the current is measured. From probability arguments we see that $I \approx e\Gamma_R P(t_p)$, where we have used the simplification that $\Gamma_R^{-1} > t_p, \Gamma_L^{-1}$. Thus, by sweeping t_p we are able to image the time evolution of Rabi oscillations, just as in the previous experiments of Nakamura and Hayashi.

The singular case of a non-adiabatic change in α from zero to a finite value produces oscillations with the maximum possible amplitude, $P_{\max} = 1$. However, in realistic systems only changes between finite values of α are feasible. This leads to a reduction in the amplitude, and achieving a significant oscillation signal

requires a suitably large change in α. In experiments with 2DEGs, changes in α of a factor of 2 are reported, and in a recent Letter by Koga *et al.*, α was shown to vary in the range $\approx (0.3-1.5)\times 10^{-12}\,\mathrm{eVm}$ (a factor of 5) in one InGaAs sample [25]. Grundler [27] has shown that the large back-gate voltages usually used to change α can be drastically reduced by placing the gates closer to the 2DEG. Thus, it is conceivable that changes in α of a factor between 2 and 5 could be produced with voltages small enough to be pulsed with rise times substantially shorter than a typical coherent oscillation period.

In Fig. 3.3a we plot time-traces of the transition probability $P(t_p)$ calculated for the first anticrossing as a function of magnetic field. We have used the values $\alpha_1 = 1.5\times 10^{-12}$ and $\alpha_2 = 0.3\times 10^{-12}\,\mathrm{eVm}$ from the Koga experiment [25]. The amplitude of the oscillations $P_{\max}$ for different ratios of α_2/α_1 is presented in Fig. 3.3b, which shows a node at $B = B_0$ ($\delta = 0$). This is because, for $\delta = 0$, the eigenstates of JCM are $2^{-1/2}(|n,\uparrow\rangle \pm |n+1,\downarrow\rangle)$ for all $\alpha \neq 0$. Therefore, a finite detuning is required to obtain the maximum amplitude, which concurs with $\delta > k_B T, \Gamma_R$ to overcome broadening effects. Both the amplitude $P_{\max}$ and frequency Ω show non-trivial dependencies on α_1 and α_2 as well as on the magnetic field. This latter behaviour stems from the parametric dependence on B of all three parameters in H_{JC}.

For our model parameters with $\alpha_2/\alpha_1 = 1/5$ and with the detuning set such that the amplitude is maximised, we have $P_{\max} \approx 0.45$ with a Rabi frequency of $\Omega = 2\,\mathrm{GHz}$, which corresponds to a period of about 3 ns. This is within accessible range of state-of-the-art experimental technique. Note that the period can be extended by using weaker confinement and SO coupling.

For both the observation of coherent oscillations, and the operation as a qubit, it is essential that the lifetime of state ψ_α^+ is long. This is the case for a pure electronic spin in a QD [37, 110], and we now show that the hybridisation of the spin with the orbitals, and the ensuing interaction phonons, does not affect this. We assume a piezo-electric coupling to acoustic phonons via the potential $V_{ep} = \lambda_{\mathbf{q}} e^{i\mathbf{q}\cdot\mathbf{r}}(b_{\mathbf{q}} + b^\dagger_{-\mathbf{q}})$, with phonon operators $b_{\mathbf{q}}$ and $|\lambda_{\mathbf{q}}|^2 = \hbar P/2\rho c q \mathcal{V}$, with coupling P, mass density ρ, speed of sound c, and volume $\mathcal{V}$ [111]. For $n = 0$, a Golden Rule calculation yields the rate

$$\Gamma_{ep}/\omega_0 = \frac{mP}{8\pi(\hbar\omega_s)^2\rho l_0}\frac{\sqrt{2}l_0}{\tilde{l}}\sin^2\theta_+\sin^2\theta_-\,\xi^5 I(\xi), \tag{3.9}$$

with $\omega_s = c/l_0$, $\xi = 2^{-1/2}(\tilde{l}/l_0)(\Delta/\hbar\omega_s)$, and $I(\xi) \leq 8/15$. Close to B_0, $\xi \ll 1$, and thus the rate is extremely small $\Gamma_{ep} \approx 10^4\,\mathrm{s}^{-1}$ (Fig. 3.3c). Therefore, the robustness of spin qubits is not significantly weakened by the SO hybridisation.

In general, residual relaxation affects our measurement scheme in two ways. During the oscillation (Fig. 3.2c), the system may relax to the eigenstate $\psi_{\alpha_2}^-$. This

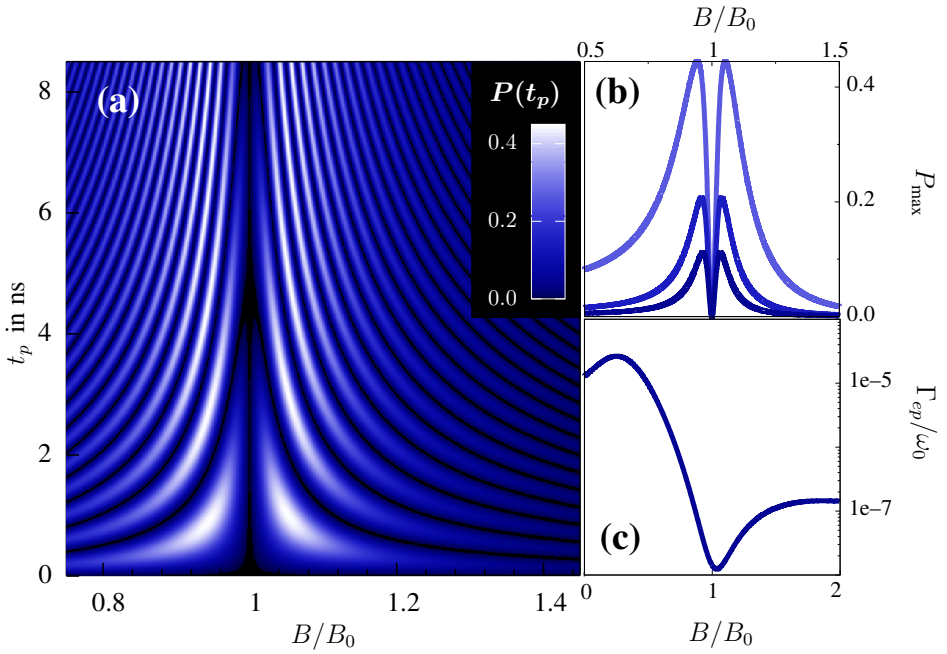

Figure 3.3: Characteristics of the Rabi oscillation. **(a)** Probability $P(t_p)$ of finding electron in upper level after time t_p following the non-adiabatic change $\alpha_1 = 1.5 \rightarrow \alpha_2 = 0.3 \times 10^{-12}$ eVm as function of magnetic field. **(b)** Amplitude of oscillation as function of B/B_0 for changing from $\alpha_1 = 1.5$, 0.8, 0.6 to $\alpha_2 = 0.3 \times 10^{-12}$ eVm (top to bottom). **(c)** Phonon-induced relaxation rate for InAs parameters $\alpha = 1.5 \times 10^{-12}$ eVm, $P = 3.0 \times 10^{-21}$ J^2/m^2, $\rho = 5.7 \times 10^3$ Kg/m^3, $c = 3.8 \times 10^3$ m/s. Close to B_0 the rate is suppressed to $\Gamma_{ep} < 10^{-7}\omega_0$.

damps the oscillation by a factor $\exp(-\Gamma_1 t_p)$ to the constant value $I = e\Gamma_R P_{\max}/2$. Relaxation during the read-out phase (Fig. 3.2d) simply reduces the overall amplitude of the signal by a factor $\exp(-\Gamma_2/\Gamma_R)$. Clearly then, to observe oscillations, we require $\Gamma_1 < \Omega$ and $\Gamma_2 < \Gamma_R$.

In summary, we have outlined a proposal for the observation of spin-orbit driven coherent oscillations in a single quantum dot. We have derived an approximate model, inspired by quantum optics, that shows the oscillating degree of freedom to represent a novel, composite spin-angular momentum qubit.

This work was supported by the EU via TMR/RTN projects, and the German and Dutch Science Foundations DFG, NWO/FOM. We are grateful to T. Brandes, C.W.J. Beenakker and D. Grundler for discussions, and to B. Kramer for guidance and hospitality in Hamburg.

3.2 Introduction to quantum dots and various derivations

3.2.1 Introduction to few-electron quantum dots

Quantum dots (QDs) are small structures in a solid typically with sizes ranging from nanometres to a few microns. The enormous progress in the field of nanotechnology has facilitated to precisely control the shape and size of such structures and thus to manipulate the number of electrons in the dot to range typically between zero and several thousands.[†] Technologically most interesting are QDs that are lithographically built in semiconductor heterostructures where it is possible to define QDs by means of lateral voltage gates and etching [3]. Such QDs show similar electronic properties to atoms, e.g. the confinement in all spatial directions leads to a discrete spectrum which even can show shell structures and the effect of Hund's rule in highly symmetric QDs [108]. Therefore, QDs are regarded as *artificial atoms*.[‡]

In addition to the similarities to atomic physics, QDs offer the fascinating possibility to investigate fundamental effects by contacting the dot with external leads and measuring transport through the system. Since it is possible in principle not only to change the confinement of the dot, but also the coupling parameters within the dot, and between the dot and the environment, a wide range of fundamental effects can be identified in the transport. By transport spectroscopy, the effect of e.g. exchange-interaction on the shell filling of QDs (Hund's rule in artificial 2D atoms) [114], and many body effects like the spin-singlet spin-triplet transition have been measured [115, 116]. Due to the coupling to leads, the QD acts as an open dissipative quantum system exhibiting e.g. the Kondo effect in the strong coupling limit [117–120]. In particular, magnetic field effects can be investigated in regimes which are inaccessible for real atoms. For example, to confine a single magnetic flux quantum in atomic size volume, magnetic fields of $\sim 10^6\,\mathrm{T}$ are required – closer to the fields of neutron stars than to those in lab conditions. Moreover, QDs are proposed as possible qubit realisations in future quantum computing architectures, either utilising the charge [121] or spin [122] degree of freedom.

In the following, we describe the spectral and transport properties of few-electron QDs by pursuing the presentation of Ref. [108]. First, we introduce the single-particle spectrum in a magnetic field in the framework of *Fock–Darwin*

[†] Of course this number denotes the freely moving conduction electrons only. The number of electrons tightly bound to the nuclei of the atoms which the solid is made of is *many* orders of magnitude larger.

[‡] Introductory reviews on quantum dots are given in Ref. [112, 113].

theory. Then, we treat the charging properties by extending the theory to the few-electron case using the *constant interaction model*. This simple but powerful model provides a basic understanding of a few-electron dot and enables one to comprehend the effects of SO interaction which are reviewed later in this chapter.

The one-electron spectra of a QD are well described by means of the *Fock–Darwin theory*. This exactly solvable model assumes a parabolically confined QD in two dimensions with perpendicular magnetic field ($\mathbf{B} = B\hat{\mathbf{e}}_z$),

$$H_0 = \frac{\left(\mathbf{p} + \frac{e}{c}\mathbf{A}\right)^2}{2m} + \frac{m}{2}\omega_0^2\left(x^2 + y^2\right), \quad \mathbf{p} = (p_x, p_y, 0). \tag{3.10}$$

To understand the effect of SO coupling which we shall present in Sec. 3.2.3, we derive the spectrum of Hamiltonian (3.10) in some detail. By choosing symmetric gauge for the vector potential, $A = (-y, x, 0)B/2$, we can rewrite Eq. (3.10) as

$$H_0 = \frac{p_x^2 + p_y^2}{2m} + \frac{m}{2}\widetilde{\omega}^2\left(x^2 + y^2\right) + \frac{\omega_c}{2}(xp_y - yp_x), \tag{3.11}$$

with $\omega_c = eB/mc$ and $\widetilde{\omega}^2 = \omega_0^2 + \omega_c^2/4$. We now define oscillator operators,

$$a_x = \frac{1}{\sqrt{2}}\left(\frac{x}{\tilde{l}} + i\frac{\tilde{l}}{\hbar}p_x\right), \quad a_x^\dagger = \frac{1}{\sqrt{2}}\left(\frac{x}{\tilde{l}} - i\frac{\tilde{l}}{\hbar}p_x\right), \quad [a_i, a_j^\dagger] = \delta_{ij}, \tag{3.12}$$

where $\tilde{l} = (\hbar/m\widetilde{\omega})^{1/2}$ (y-component is analogously defined). This leads to

$$H_0 = \hbar\widetilde{\omega}\left(a_x^\dagger a_x + a_y^\dagger a_y + 1\right) + \frac{\hbar\omega_c}{2i}\left(a_y a_x^\dagger - a_x a_y^\dagger\right). \tag{3.13}$$

The introduction of

$$a_\pm = 2^{-\frac{1}{2}}(a_x \mp i a_y) \tag{3.14}$$

decouples x and y oscillators into eigenmodes of frequency $\omega_\pm = \widetilde{\omega} \pm \omega_c/2$,

$$H_0 = \hbar\omega_+\left(n_+ + \frac{1}{2}\right) + \hbar\omega_-\left(n_- + \frac{1}{2}\right), \quad n_\pm = a_\pm^\dagger a_\pm. \tag{3.15}$$

Although this representation of the Hamiltonian is convenient to discuss the effect of SO coupling in the next section, it is customary to rewrite the decoupled modes in terms of radial and angular momentum quantum numbers,

$$n := \min(n_+, n_-), \quad l := n_- - n_+, \tag{3.16}$$

leading to a spectrum known as the Fock–Darwin states [123, 124],

$$E_{nl} = (2n + |l| + 1)\,\hbar\widetilde{\omega} - \frac{1}{2}l\,\hbar\omega_c. \tag{3.17}$$

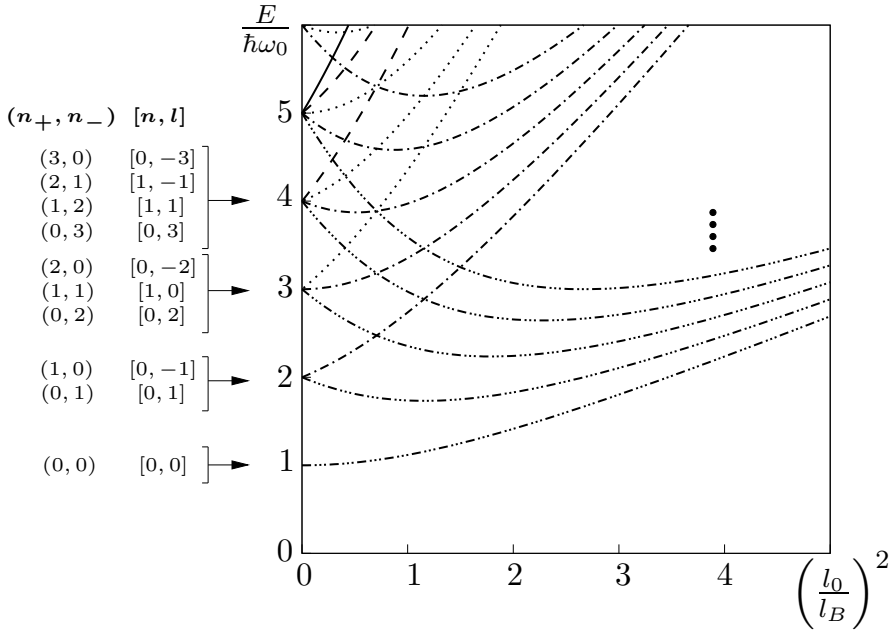

Figure 3.4: Magnetic field evolution of the low-lying Fock–Darwin spectrum (for clarity only modes $n_\pm \leq 4$ are shown). The different parametrisation in quantum numbers (n_+,n_-) and $[n,l]$ are marked for the 10 lowest modes. Curves which converge towards to same Landau level in the high field limit share a common style of line.

Figure 3.4 shows the low-lying spectrum of Hamiltonian (3.10) as a function of the magnetic field which is expressed as a dimensionless ratio of the confinement length $l_0 = (\hbar/m\omega_0)^{1/2}$ and magnetic length $l_B = (\hbar/m\omega_c)^{1/2}$. For clarity, only the lowest modes for $n_\pm \leq 4$ are shown together with their parametrisation in radial and angular momentum quantum numbers. For $B = 0$ ($l_B \to \infty$) the system is a simple two-dimensional harmonic oscillator with two degenerate modes $\omega_\pm = \omega_0$. For high magnetic field, corresponding to the limit $\omega_0 \to 0$, the eigenenergies degenerate into two-dimensional Landau levels, $\omega_+ \to \omega_c$, $\omega_- \to 0$. Thus, n_+ describes the Landau level index for large B. Modes which converge into the same Landau level share a common style of lines in Fig. 3.4.

This model with parabolic confinement is an appropriate estimate for conventional quantum dots which are defined by metal gates on top of the quantum well [108]. In the following, we consider basic transport properties of QDs. Therefore, we have to extend the model to a QD with many electrons.

Insight into the spectral properties of QDs can be gained by attaching metallic leads to it and performing transport spectroscopy by simply measuring the current through the dot [125]. Here, we restrict ourselves to the case of weak coupling

to the leads where the number of electrons in the dot is a well defined integer and the discrete nature of charge determines the single electron transport through the system in a mostly classical way. A current through the QD is given by a sequence of tunnelling events of single electrons. The Coulomb repulsion between electrons leads to a considerable energy cost when adding an extra electron charge to the QD. Current can only flow if this energy is supplied by external voltages – a phenomenon known as *Coulomb blockade* [126]. The energy threshold which is to be overcome when adding an electron to a QD that already contains N electrons is the *addition energy* $E_{\text{add}} := \mu(N+1) - \mu(N)$ where $\mu(N)$ is the chemical potential of the QD with N electrons. Exact calculation of E_{add} is a formidable task, since it requires the solution of the full many body problem of a few dozen electrons.

An estimate for the addition energy is given by the *constant interaction (CI) model* [125, 126] which assumes that the Coulomb interaction between the electrons in the dot is independent of N. Thus, the addition energy is approximated by $E_{\text{add}} = e^2/C + \Delta E$, where ΔE is the energy difference between subsequent single-electron states (calculated e.g. in the Fock–Darwin framework) and the Coulomb interactions are represented as a single capacitance C, which leads to the classical charging energy $E_c = e^2/C$ for a charge e. This approximation for E_{add} requires that the Coulomb interaction does not mix up the single electron wavefunctions. A condition which is generally fulfilled in vertical GaAs dots where the confinement induced single electron energy scale is comparable or larger than the interaction energies, $\Delta E \geq E_c$ [108].

Despite its simplicity, the CI model is remarkably successful in providing a basic understanding of experiments on few-electron QDs [108]. The implication that when adding electrons to a QD they will successively occupy consecutive single-particle levels – while the energy cost of E_c has to be paid for each electron – is sufficient to explain the shell structure which is found in the addition energy spectra [125]. For zero magnetic field the two-dimensional oscillator states at $E = (M+1)\hbar\omega_0$ with $M = 2n + |l|$ are $(M+1)$-fold degenerate, see Fig. 3.4. Therefore, in the CI model, each single-particle level can take up to $2(M+1)$ electrons due to spin degeneracy. This leads to the magic numbers $2, 6, 12, \ldots$ in the shell structure. Many magnetic field effects in QD spectra can be explained by the crossover from degenerate two-dimensional harmonic oscillator states for $B = 0$ to the lowest Landau level in the high field limit. The CI model can be extended to include effects of exchange interaction such as Hund's rule, which obliges the dot shells to be filled with electrons of parallel spin first [108].

Not included in the CI model are effects which violate the assumption of constant interaction. In the presence of a magnetic field the characteristic length $\tilde{l}$ decreases for larger B, indicating that the confinement becomes stronger. Thus, two electrons which occupy the same state will be pushed closer together, significantly increasing the Coulomb interaction. Therefore, at some magnetic fields it

might become favourable that one electron undergoes a transition to a state with higher angular momentum, and thus reducing the overlap of wavefunctions. Such a crossover leads to the singlet-triplet transition for $N = 2$ [116]. This indicates that the CI model fails at large B. Moreover, when adding a large number of electrons to the dot the extension of the electron density increases and alters the shape of the dot, thus making it impossible to describe the dot with a constant capacitor C.

In spite of these limitations, the CI model provides an excellent description for few-electron QDs in weak magnetic field (typically $B \leq 1\,\mathrm{T}$ in GaAs) when the number of electrons is only slightly varied.

In Sec. 3.2.4 we apply the CI model to describe coherent oscillations in a single spin-orbit interacting QD made in InGaAs. The number of electrons in the dot changes only by one and typical magnetic fields are $\sim 0.1\,\mathrm{T}$, perfectly within the applicability of the CI model. Effects of exchange can also be neglected because spin degeneracy is lifted by the strong Zeeman effect in InGaAs.

3.2.2 Spin-orbit effects in quantum dots

In the previous treatment, the spin of the electron simply led to a twofold degeneracy of quantum dot levels at $B = 0$. In general, this degeneracy is expected to be affected by the presence of spin-orbit (SO) coupling. In the following, we will introduce the impact of SO coupling on the electron spectrum of Coulomb blockaded QDs. As in the previous chapter, we restrict ourselves to the case of Rashba SO coupling by assuming QDs made in a InAs heterostructure.

The effects of SO coupling on QDs have been investigated by a number of authors, treating both non-interacting and interacting few-electron dots [102–107]. In particular, Governale [105] showed by using spin-density functional theory that the SO coupling in the QD may lead to an appearance of spin textures and a suppression of Hund's rule due to a competition of Rashba effect and exchange interaction. Chakraborty & Pietiläinen [102] showed by using exact numerical diagonalisation that the singlet-triplet transition, as a prominent feature of Coulomb interaction in a two-electron dot, is shifted towards lower magnetic fields due SO coupling. Recently, the same authors showed that SO coupling leads to new modes in the optical absorption spectrum of QDs with up to four electrons [127].

Our analysis differs in a crucial respect: motivated by the analogy between parabolically confined SO systems and quantum optics that we found in the previous chapter, we derive an effective model for the SO-interacting QD in the next section. This model is formally identical to the Jaynes-Cummings model of quantum optics and provides systematic insight into the effects of SO coupling in QDs.

3.2.3 Derivation of the effective model

We start from the Fock–Darwin description that was introduced in the Sec. 3.2.1. In contrast to GaAs, where the Zeeman effect is normally negligible, it has a significant influence in InAs. The change in orbital energy due to a magnetic field is roughly $\hbar\omega_c = \hbar eB/mc$ which is as much as $1.76\,\mathrm{meV\,T^{-1}}$ in GaAs due to small effective mass $m_{\mathrm{GaAs}} = 0.06\,m_0$ [108]. On the other hand, the effect on the Zeeman spin splitting $g\mu_{\mathrm{B}}B$ is only $\sim 0.025\,\mathrm{meV\,T^{-1}}$ in GaAs. This is due to the small effective g factor, $g_{\mathrm{GaAs}} = -0.44$. Thus in GaAs, a magnetic field is about 70 times more effective in changing the orbital energy than the Zeeman spin splitting. In contrast, in InAs the effective mass is comparable to that in GaAs ($m_{\mathrm{InAs}} = 0.05\,m_0$) but the g-factor can vary from -4 in InGaAs to about -9 in InAs [128] (bulk value -15), making the Zeeman effect up to 30 times larger than in GaAs. Therefore, we extend the Fock–Darwin Hamiltonian (3.15) to take the Zeeman effect into account,

$$H_0 = \hbar\omega_+\left(n_+ + \frac{1}{2}\right) + \hbar\omega_-\left(n_- + \frac{1}{2}\right) + \frac{1}{2}g\mu_{\mathrm{B}}B\sigma_z. \tag{3.18}$$

Following the line of calculation of Sec. 3.2.1, we can rewrite the Rashba Hamiltonian

$$H_{\mathrm{SO}} = -\frac{\alpha}{\hbar}\left[\left(\mathbf{p} + \frac{e}{c}\mathbf{A}\right)\times\boldsymbol{\sigma}\right]_z, \tag{3.19}$$

by introducing oscillator operators Eq. (3.14) as

$$\begin{aligned} H_{\mathrm{SO}} = \frac{\alpha}{\sqrt{2}\tilde{l}}\Bigg[&\left\{\frac{1}{2}\left(\frac{\tilde{l}}{l_B}\right)^2\left(a_x + a_x^\dagger\right) - i\left(a_y - a_y^\dagger\right)\right\}\sigma_x \\ &+ \left\{\frac{1}{2}\left(\frac{\tilde{l}}{l_B}\right)^2\left(a_y + a_y^\dagger\right) + i\left(a_x - a_x^\dagger\right)\right\}\sigma_y\Bigg]. \end{aligned} \tag{3.20}$$

Transforming into $\omega_\pm$ modes, this reduces to

$$H_{\mathrm{SO}} = \frac{\alpha}{\tilde{l}}\left[\gamma_+\left(a_+\sigma_+ + a_+^\dagger\sigma_-\right) - \gamma_-\left(a_-\sigma_- + a_-^\dagger\sigma_+\right)\right], \tag{3.21}$$

where

$$\gamma_\pm = 1 \pm \frac{1}{2}\left(\frac{\tilde{l}}{l_B}\right)^2, \quad \sigma_\pm = \frac{1}{2}(\sigma_x \pm i\sigma_y). \tag{3.22}$$

Taking account of the negative sign of the g-factor in InAs we perform a unitary rotation of the spin such that $\sigma_z \to -\sigma_z$ and $\sigma_\pm \to -\sigma_\mp$ to return to the customary

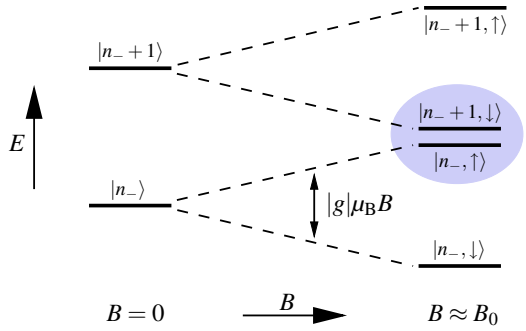

Figure 3.5: Resonance condition for Zeeman split ω_- modes at $B = B_0$ (n_+ fixed).

spin sequence of the Zeeman effect where electrons with spin up have a larger energy than those with spin down. Doing this we arrive at the Hamiltonian

$$H = \hbar\omega_+\left(n_+ + \frac{1}{2}\right) + \hbar\omega_-\left(n_- + \frac{1}{2}\right) + \frac{1}{2}|g|\mu_B B\sigma_z + \frac{\alpha}{\tilde{l}}\left[\gamma_-\left(a_-\sigma_+ + a_-^\dagger\sigma_-\right) - \gamma_+\left(a_+\sigma_- + a_+^\dagger\sigma_+\right)\right]. \tag{3.23}$$

In analogy to quantum optics we can understand the above Hamiltonian in terms of a spin which is coupled to two boson modes with energies $\omega_\pm$. Here, the coupling is mediated by the SO interaction. The spectral properties of the two boson modes alone has been discussed in Sec. 3.2.1, leading to the Fock–Darwin states (Fig. 3.4). In Eq. (3.23) the presence of the spin leads to two effects. (i) Every state becomes spin split due to the Zeeman effect and (ii) the additional coupling between boson modes and spin leads to anticrossings in the spectrum. In the representation in terms of $\omega_\pm$ modes we see that the SO interaction leads to a coupling between adjacent $\omega_\pm$ modes with opposite spin due to the operators $a_\pm$ and $a_\pm^\dagger$ in the last term of the Hamiltonian. There are no direct transitions between ω_+ and ω_- modes.

From the last term in Eq. (3.23) we see that the SO coupling has only non-zero matrix elements for

$$\langle n_+ + 1, n_-, \downarrow|H_{\mathrm{SO}}|n_+, n_-, \uparrow\rangle, \quad \langle n_+ + 1, n_-, \uparrow|H_{\mathrm{SO}}|n_+, n_-, \downarrow\rangle, \tag{3.24}$$

$$\langle n_+, n_- + 1, \downarrow|H_{\mathrm{SO}}|n_+, n_-, \uparrow\rangle, \quad \langle n_+, n_- + 1, \uparrow|H_{\mathrm{SO}}|n_+, n_-, \downarrow\rangle. \tag{3.25}$$

Therefore, from a perturbative point of view, the SO coupling becomes most import when adjacent $\omega_\pm$ modes with opposite spin are almost degenerate. The strategy to reach such a resonance is different for ω_+ and ω_- modes. As a function of magnetic field, resonances of neighbouring ω_- modes can easily occur

due to the Zeeman effect, since for fixed n_+ these modes converge into the same Landau level at large B (Fig. 3.4 and 3.5). Adjacent ω_+ modes, however, converge towards different Landau levels, and the Zeeman spin splitting is generally not large enough to match this energy separation. Thus, to reach coincidence of spin split ω_+ modes an additional in-plane magnetic field may be applied, enabling the independent manipulation of Landau level separation (determined by the perpendicular field) and Zeeman splitting (given by total field). Such coincidence technique is utilised experimentally in SO-interacting 2D systems, see e.g. Ref. [129].

In the following, we concentrate on the low-lying part of the dot spectrum which is most important for the transport properties in the few-electron regime. In Fig. 3.1a on page 53, the numerical result of a part of the excitation spectrum of Hamiltonian (3.23) is shown for typical InGaAs parameters. The energy is measured is units of $\hbar\omega_0$ and the zero-point energy is omitted. Also not shown is the energy of the ground state $|n_+ = 0, n_- = 0, \downarrow\rangle$. In contrast to the spin degenerate Fock–Darwin spectrum in GaAs, shown in Fig. 3.4, the spectrum for InGaAs shows the Zeeman spin splitting and anticrossings as a consequence of SO coupling when adjacent ω_- modes become degenerate. This situation is sketched schematically in Fig. 3.5. Close to $B = B_0$, the SO interaction leads to hybridisation of $|n_- + 1, \downarrow\rangle$ and $|n_-, \uparrow\rangle$ which results in the anticrossing shown in Fig. 3.1.

The effect of SO coupling on the spectrum is most strikingly seen in this anticrossing. This marks the different physical relevance of the terms in Eq. (3.24) and (3.25). The terms on the left correspond to SO-induced transitions where an up spin is flipped downwards and the index of $\omega_\pm$ modes is excited by one additional quantum, corresponding to a change of the orbital state in the language of the quantum dot. Close to resonance $B = B_0$ these transitions are energy conserving; the energy which is gained from the spin flip is transferred into a orbital excitation. On the contrary, the terms on the right of Eqs. (3.24) and (3.25) correspond to transitions where the spin and orbital degree of freedom are excited simultaneously, thus being "energy non-conserving" with respect to the total excitation operator $\hat{N} = \hat{n}_- + \hat{n}_+ + J_z$ which counts to the number of boson and spin excitations in the system.

A similar situation appeared in Sec. 2.2.4 in the high magnetic field limit of a SO-interacting quantum wire. There, in the context of Eq. (2.26), the notion of rotating and counter-rotating terms was introduced. Following the same line of reasoning, we can identify terms in H_{SO} which lead to the left hand side of Eqs. (3.24) and (3.25) as rotating, whereas terms on the right are counter-rotating. From quantum optics we know that the *rotating-wave approximation* (RWA), and thus the neglect of counter-rotating terms, is well justified if the coupling strength is weak. Transferring this idea to the SO-coupled QD, we can neglect terms preceeded by γ_+ in Eq. (3.23) when the SO coupling is small compared to the con-

finement. This decouples the ω_+ modes from the rest of the system, giving

$$H = \omega_+ n_+ + H_{\rm JC}, \tag{3.26}$$

with energies rescaled by $\hbar\omega_0$ and the *Jaynes–Cummings model* (JCM) $H_{\rm JC}$ given by Eq. (3.6),

$$H_{\rm JC} = \omega_- a_-^\dagger a_- + \frac{1}{2}E_z\sigma_z + \lambda\left(a_-\sigma_+ + a_-^\dagger\sigma_-\right), \tag{3.27}$$

with $\lambda = l_0^2\gamma_-/2\tilde{l}\,l_{\rm SO}$. This model is completely integrable (see appendix. A) has ground state $|0,\downarrow\rangle$ with energy $E_{\rm G} = -E_z/2$ and excited energies

$$E_\alpha^{(n,\pm)} = \left(n+\frac{1}{2}\right)\omega_- \pm \frac{\Delta_n}{2}, \tag{3.28}$$

with detuning $\delta \equiv \omega_- - E_z$ and $\Delta_n \equiv \sqrt{\delta^2 + 4\lambda^2(n+1)}$, corresponding to the eigenstates

$$|\psi_\alpha^{(n,\pm)}\rangle = \cos\theta_\alpha^{(n,\pm)}|n,\uparrow\rangle + \sin\theta_\alpha^{(n,\pm)}|n+1,\downarrow\rangle, \tag{3.29}$$

with $\tan\theta_\alpha^{(n,\pm)} = (\delta\pm\Delta_n)/2\lambda\sqrt{n+1}$. For our parameters, this model describes the energy levels of the SO-interacting QD to within 10% of the typical anticrossing width (given by Δ_n in the JCM) and 1% of ω_0. This small discrepancy is shown in Fig. 3.1b. As a characteristic measure of the quality of the RWA we can use the prediction of the JCM that the anticrossing width increases with $\alpha\sqrt{n+1}$. In Fig. 3.1c this width Δ is plotted against its central energy. The JCM (solid line) is compared with the exact numerical result (circles). For a QD of size $l_0 = 150\,$nm, almost perfect coincidence is found for α between $(0.3\ldots1.5)\times 10^{-12}\,$eVm, corresponding to experimentally found values in InGaAs [25]. For larger values the anticrossing width is underestimated in the JCM, as indicated in uppermost curve in Fig. 3.1c for the value $\alpha = 2.0\times10^{-12}\,$eVm. Therefore, we can conclude that the JCM is a reasonable approximation for SO-interacting QDs where the confinement is stronger than the SO coupling. In this regime the integrability of the JCM provides us with the analytical eigenstates and energies which we use in the following to discuss coherent oscillations in a QD.

3.2.4 Coherent oscillations

In this section we investigate coherent oscillations (CO) in a SO-coupled QD system. This illustrates the fruitfulness of the analogy with quantum optics. Although the origin of coherent oscillations is simply the fact that the time evolution of a

quantum system is generally non-stationary when the system is initialised in a non-eigenstate, the experimental observation of such oscillations highlights our ability to manipulate nature on a microscopic level.

Whenever we instantaneously change the parameters δ, λ, ω of the system we may expect CO because, after the change, the system is generally not in a stationary state. In the following, we omit the '$-$' index for the frequency in Eqs. (3.27) and (3.28) and include the explicit $\sqrt{n+1}$ dependence by setting $\tilde{\lambda} := \lambda\sqrt{n+1}$. To prepare the system in a non-eigenstate we propose a non-adiabatic change of λ, simply by altering the strength of the SO coupling by means of an additional gate voltage pulse. In terms of the JCM such a pulse leads to oscillations in the $\{|n,\uparrow\rangle, |n+1,\downarrow\rangle\}$ subspace of the Hilbert space for fixed ω. In contrast, every change in ω would destroy the strict decomposition of the Hilbert space, leading to a mixing of different ω_- modes. A change of magnetic field would lead to a simultaneous modification of *all* parameters ω, δ, λ.

This relation between the parameters due to an external magnetic field is a significant difference to the JCM in quantum optics where all parameters can be tuned individually.

In the following, we solve the time-dependent Schrödinger equation for the experimental scheme which has been proposed in chapter 3.1. To prepare a non-stationary state we perform the following: (i) Assume the system is in the eigenstate of $H_{\mathrm{JC}}(\alpha_1)$, $|\psi^-_{\alpha_1}\rangle$, for times $t < 0$. (ii) At $t = 0$ we instantaneously switch from $\alpha_1 \to \alpha_2$ while keeping all other parameters fixed. Thus, in the basis of eigenstates of $H_{\mathrm{JC}}(\alpha_2)$ we have

$$|\psi^-_{\alpha_1}\rangle = \cos\theta^-_{\alpha_1}|n,\uparrow\rangle + \sin\theta^-_{\alpha_1}|n+1,\downarrow\rangle = c_+|\psi^+_{\alpha_2}\rangle + c_-|\psi^-_{\alpha_2}\rangle \tag{3.30}$$

where

$$c_\pm = \langle\psi^\pm_{\alpha_2}|\psi^-_{\alpha_1}\rangle = \cos\left(\theta^\pm_{\alpha_2} - \theta^-_{\alpha_1}\right) =: \cos\Delta\theta_\pm. \tag{3.31}$$

The probability to find the system in state $|\psi^+_{\alpha_1}\rangle$ after pulse time $t_p > 0$ is

$$P(t_p) = |\langle\psi^+_{\alpha_1}|\Psi(t_p)\rangle|^2 = |\langle\psi^+_{\alpha_1}|e^{-iH(\alpha_2)t_p/\hbar}|\psi^-_{\alpha_1}\rangle|^2 \tag{3.32}$$

$$= 1 - |\cos^2\Delta\theta_+ e^{-2i\Omega t_p} + \cos^2\Delta\theta_-|^2, \tag{3.33}$$

where $\Omega := (E^+_{\alpha_2} - E^-_{\alpha_2})/2$ is the frequency of CO (in units of $\hbar\omega_0$).
From Eq. (3.28) follows

$$\Omega = \frac{1}{2}\tilde{\lambda}_2\sqrt{\left(\frac{\delta}{\tilde{\lambda}_2}\right) + 4}\,. \tag{3.34}$$

For zero detuning we find $\Omega = \Omega_0 := \tilde{\lambda}_2$. In quantum optics Ω_0 is called *Rabi frequency*. It describes the periodic energy exchange between an atomic pseudo-spin and the *resonant* radiation field. In our model we will call the frequency of CO Rabi frequency – even for finite detuning.

From Eq. (3.34) we see that the frequency of oscillation is only determined by the coupling strength which is present during the coherent evolution ($\tilde{\lambda}_2$). The amplitude of oscillation, however, depends on the ratio $\tilde{\lambda}_1/\tilde{\lambda}_2$ *and* the detuning δ. In Eq. (3.33) completeness yields

$$c_+^2 + c_-^2 = \cos^2\Delta\theta_+ + \cos^2\Delta\theta_- = 1. \tag{3.35}$$

The maximum amplitude in $P(t_p)$ is found for t_p such that $\exp(-2i\Omega t_p) = -1$, leading to

$$P_{\max} = 1 - |\cos^2\Delta\theta_+ - \cos^2\Delta\theta_-|^2. \tag{3.36}$$

If $\cos^2\Delta\theta_\pm \approx 1/2$ we expect probability oscillations of order 100%. To translate this into a condition for δ, $\tilde{\lambda}_1$ and $\tilde{\lambda}_2$ we express

$$\tan\theta^\pm_{\alpha_1,\alpha_2} =: \chi^\pm_{1,2}, \tag{3.37}$$

leading to

$$\Delta\theta_\pm = \arctan\chi_2^\pm - \arctan\chi_1^- \tag{3.38}$$

$$= \arctan\frac{\chi_2^\pm - \chi_1^-}{1+\chi_2^\pm\chi_1^-} =: \arctan\gamma_\pm, \tag{3.39}$$

by using Eq. (4.4.34) in Ref. [130]. To find probability oscillation of $\approx 100\%$ we need

$$c_\pm^2 \approx \frac{1}{2} \;\Rightarrow\; \Delta\theta \approx \pm\left\{\frac{1}{4}\pi, \frac{5}{4}\pi\right\} \;\Rightarrow\; \gamma \approx \pm 1. \tag{3.40}$$

Trivially, we have $\gamma \approx \pm 1$ in the limit

$$\tilde{\lambda}_1 \ll \delta \ll \tilde{\lambda}_2 \;\Rightarrow\; P(t_p) \approx \cos^2\Omega t_p, \tag{3.41}$$

corresponding to CO in the resonant JCM limit in quantum optics. However, for the QD condition (3.41) corresponds to the limit of non-adiabatic switching between almost zero and strong SO coupling. Unfortunately, in real physical systems this limit is unlikely to be fulfilled. Thus, in contrast to optical systems, only probability oscillations with amplitudes less than 100% are feasible in SO-interacting QDs.

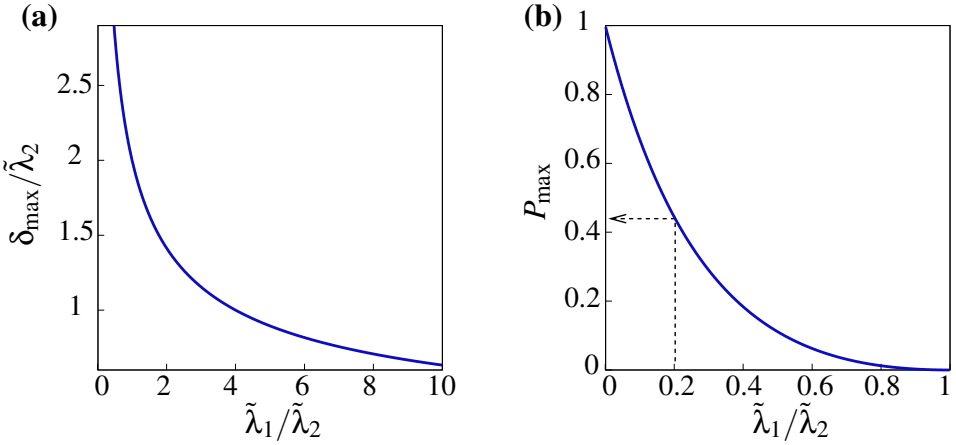

Figure 3.6: **(a)** Optimal detuning $\delta_{max}/\tilde{\lambda}_2$ to find maximum in amplitude of probability oscillations as a function of $\tilde{\lambda}_2/\tilde{\lambda}_1$. **(b)** Maximal amplitude of oscillation P_{max} as a function of $\tilde{\lambda}_2/\tilde{\lambda}_1$. For a change in λ by a factor 5 the maximal amplitude of oscillation is $\sim 45\,\%$.

From Eq. (3.36) and (3.39) we see that the *amplitude* of oscillation does not depend on the sequence, i.e. whether we change from $\alpha_1 \to \alpha_2$ or vice versa. However, the sequence is important for the *frequency*, see Eq. (3.34). In addition, the detuning plays an important role concerning the amplitude and frequency of oscillations. For $\delta = 0$ (resonant JCM) eigenfunctions are independent of α [Eq. (3.29)],

$$|\psi^{\pm}\rangle = \frac{1}{\sqrt{2}}(|n,\uparrow\rangle \pm |n+1,\downarrow\rangle)\,. \tag{3.42}$$

Thus, for $\delta = 0$, a non-adiabatic change of α does not lead to any oscillations because the system stays in a stationary state. Conversely, for $\delta \gg \omega, \tilde{\lambda}_1, \tilde{\lambda}_2$ the amplitude is also strongly suppressed because

$$\delta \gg \omega, \tilde{\lambda}_1, \tilde{\lambda}_2 \quad \Rightarrow \gamma_+ \to \delta,\ \gamma_- \to \frac{1}{\delta} \tag{3.43}$$

$$\Rightarrow \Delta\theta_+ \to \frac{\pi}{2},\ \Delta\theta_- \to 0 \tag{3.44}$$

$$\Rightarrow P_{max} = 0 \text{ by Eq. (3.36).} \tag{3.45}$$

Thus, for a given sequence $\alpha_1 \to \alpha_2$ the maximum amplitude of probability oscillations can be found at a non-zero detuning δ_{max}. The evolution of $\delta_{max}/\tilde{\lambda}_2$ as function of $\tilde{\lambda}_2/\tilde{\lambda}_1$ is shown in Fig. 3.6a.

The maximal amplitude of probability oscillation at $\delta = \delta_{max}$ as a function of $\tilde{\lambda}_2/\tilde{\lambda}_1$ is shown in Fig. 3.6b. Since the amplitude does not depend on the sequence

$\alpha_1 \leftrightarrow \alpha_2$, all possible ratios are shown in the figure. For the ratios of $\tilde{\lambda}_2/\tilde{\lambda}_1 = 2$ and 5, as in chapter 3.1, we find amplitudes of the order of 12% and 45%, respectively.

In a possible experimental setup, the magnetic field is used to change the detuning δ. Unlike the JCM in quantum optics, the parameters δ, ω and $\tilde{\lambda}$ are connected via the magnetic field. Thus, changing B effectively alters the coupling between the pseudo-spin states in the JCM. The non-linear dependence of δ/λ as function of B leads to non-trivial features in the oscillation pattern.

In the following, we calculate how the characteristics of the oscillation depend on B. Whenever material parameters are needed we use InGaAs values [25], $|g| = 4$, $m/m_0 = 0.05$, $\alpha_{1,2} = (0.3 \ldots 1.5) \times 10^{-12}\,\mathrm{eVm}$. The confinement length is set to $l_0 = 150\,\mathrm{nm}$, corresponding to an energy scale $\hbar\omega_0 \approx 0.1\,\mathrm{meV}$. With these numbers we have $l_{\mathrm{SO},2,1} = (500 \ldots 2500)\,\mathrm{nm}$. Compared to bulk InAs the InGaAs parameter for the strength of the SO coupling is rather small. This is to make sure that the period of Rabi oscillations is in a technologically accessible range of $> 100\,\mathrm{ps}$. Although, a large *ratio* of $\tilde{\lambda}_2/\tilde{\lambda}_1$ is needed to get a significant oscillation *amplitude* – a small value for $\tilde{\lambda}_2$ is needed to have a low Rabi frequency.

We now evaluate the oscillation in $P(t_p)$ as a function of magnetic field. The frequency of coherent oscillations Eq. (3.34) depends non-trivially on B. Rewriting the frequency in units of the resonance Rabi frequency yields

$$\frac{\Omega(B)}{\Omega_0} = \frac{1}{2}\frac{\tilde{\lambda}_2(B)}{\tilde{\lambda}_2(B_0)}\sqrt{\left[\frac{\delta}{\tilde{\lambda}_2}(B)\right]^2 + 4}, \quad \Omega_0 = \Omega(B_0). \tag{3.46}$$

This non-linear function leads to the result that away from resonance ($B \neq B_0$), an increase of λ_2 by a factor 5 does not translate into a 5 times larger frequency. Only at resonance a linear λ_2-dependence is recovered.

In Fig. 3.3a the probability of finding an electron in the upper state after a pulse time t_p as a function of the detuning is shown. The asymmetric course of the oscillation amplitude (Fig. 3.3b) is a consequence of the parametric dependence on the magnetic field.

3.2.5 The current

We now establish a relation between oscillations in the occupation probability and the transport properties via sequential tunnelling by rate equation arguments. The time scales in the different steps of the operation scheme (as shown in Fig. 3.2 on

page 55) fulfil the conditions

1. initialisation time (panel Fig. 3.2b) $t_i \sim \Gamma_R^{-1} > \Gamma_L^{-1}$,
2. pulse time (panel Fig. 3.2c) $t_p < \Omega^{-1}$,
3. read-out time (panel Fig. 3.2d) $t_o \sim \Gamma_R^{-1}$.

The time to initialise the dot in state Ψ^- is limited by the time it takes to get rid of an electron which by chance occupies the state Ψ^+. Requiring $\Gamma_L > \Gamma_R$ leads to a preferential filling of the dot from the left lead. In addition, the pulse time needs to be smaller than the inverse Rabi frequency to observe oscillation behaviour. The read-out time is given by Γ_R^{-1}. Thus, the period for one cycle is $T_{\text{cycle}} = 2\Gamma_R^{-1} + t_p$ and the transferred charge is $2eP(t_p)$. The factor $2e$ corresponds to the fact that if $P(t_p) = 1$ then two electrons are transferred per cycle on average; every electron which undergoes the oscillation is accompanied by an additional electron simply tunnelling through the dot via state Ψ^+. Thus, the current can be estimated as

$$I(t_p) = \frac{2eP(t_p)}{2\Gamma_R^{-1} + t_p} \approx e\Gamma_R P(t_p), \quad \text{for } \Gamma_R \ll \Omega. \tag{3.47}$$

By measuring the current as a function of the pulse length t_p one can map the oscillation in the occupation probability onto a transport quantity.

3.3 Effects of relaxation

Phase coherence is essential for the observation of probability oscillations which is outlined above. However, in every real physical system decoherence is always present due to coupling to the environment. Even if the system is prepared in the ground state the phase will be randomised after times longer than the dephasing time. Our scheme for the observation of coherent oscillations requires the systems to remain in an excited state for a rather long time. Thus, any relaxation from the excited state to the ground state will lead to dephasing and destroy the CO signal.

The relevant mechanisms for relaxation and dephasing of spin states in QDs are still being investigated [37]. A lower bound for the relaxation time of $50\,\mu$s has been measured at 20 mK in a one-electron GaAs dot with an in-plane field of 7.5 T [131]. This time is orders of magnitude larger than in a 2D system. Notably, the measurement was limited by the signal-to-noise ratio and thus, the real value of the relaxation time may even be larger, substantiating the proposal to consider the spin state of quantum dots as a possible physical realisation of a quantum computing architecture [122].

The theoretical understanding of spin-flip transitions in QDs is important in order that one can estimate spin coherence times which need to be sufficiently long

for quantum computation. In contrast to the situation in a 2D electron gas, and although electron-electron (e-e) interaction may become important for the spectral properties of a QD, the localised electrons in the dot do not experience substantial e-e *scattering* [110, 132]. Thus, the dominant source of dissipation in dots is the interaction with phonons whose effect on spin relaxation has been calculated for QDs [110, 133, 134]. In these references, the spin-orbit coupling due to the lack of inversion symmetry is treated perturbatively as one mechanism leading to *spin admixture* and thus allowing transitions between states of (previously) opposite spin. The dissipation to phonons is needed to comply with energy conservation. This spin-flip mechanism is believed to dominate the relaxation between spin-split Zeeman sublevels in GaAs QDs for large magnetic fields, whereas at smaller fields (typically $< 0.5\,\mathrm{T}$ in GaAs) the hyperfine coupling to nuclear spins prevails [135–137]. In InAs, which also yields a non-zero nuclear field, the situation is expected to be similar. Secondary processes are direct spin-phonon interactions like the spin-orbit coupling of the electron spectrum due to the strain field produced by acoustic phonons employed by Frenkel [138], and the dependence of the effective g-factor on lattice deformations.

In contrast to the situation in GaAs QDs mentioned above where a pure spin state is considered as a possible quantum bit, in our treatment of SO-interacting InGaAs QDs, the qubit degree of freedom is spanned by the two states in a JCM subspace. Since the SO coupling is included in our calculation of the quantised dot states, it is incorporated into the coherence of the system. Therefore, one might naively assume that this may suppress the SO-induced relaxation channel. However, the hybridisation within every JCM subspace couples the spin to the orbitals which are sensitive to electron-phonon scattering. Thus, the question arises as to whether this hybridisation might nullify the robustness of the qubit. In the next section, the general effect of relaxation on the current signal of the coherent oscillations is treated by phenomenologically introducing relaxation rates at the most sensitive states of the operating cycle. In Sec. 3.3.2 we microscopically calculate the phonon-induced relaxation rate for a given JCM two-level system, showing that the hybridisation with the orbital degree of freedom indeed opens a new relaxation channel. However, the calculated relaxation rates are small enough not to prevent our proposed measurement scheme from operating.

3.3.1 Effects of relaxation on coherent oscillations

In this section we phenomenologically introduce the effect of relaxation at those steps of the cycle where the electron occupies an excited state for a long time, i.e. the coherent evolution during the pulse time t_p and the following read-out phase, see Fig. 3.2 on page 55. The rates to relax to the ground state in these phases are denoted by Γ_1 and Γ_2, respectively.

The relaxation during read-out phase corresponds to the transition $\Psi^+_{\alpha_1} \rightarrow \Psi^-_{\alpha_1}$ and this occurs with probability $[1-\exp(-\Gamma_2 t_o)]P(t_p)$. Thus, the current [Eq. (3.47)] is reduced to

$$I = e\Gamma_R \left[1 - \left(1 - e^{-\frac{\Gamma_2}{\Gamma_R}}\right)\right] P(t_p) \tag{3.48}$$

$$= e\Gamma e^{-\frac{\Gamma_2}{\Gamma_R}} P(t_p) \approx e\Gamma_R \left(1 - \frac{\Gamma_2}{\Gamma_R}\right) P(t_p), \quad \text{for } \Gamma_2 \ll \Gamma_R. \tag{3.49}$$

This type of relaxation simply reduces the amplitude of oscillation. To obtain a significant oscillation signal in the current we require $\Gamma_2 \ll \Gamma_R$.

The effect of the relaxation during the coherent evolution (Fig. 3.2c) has more serious consequences because it leads to dephasing. Although the relaxed ground state $\Psi^-_{\alpha_2}$ is an eigenstate of $H_{\mathrm{JC}}(\alpha_2)$, when flipping back to α_1 after the pulse time t_p the system starts Rabi oscillations – this time during the read-out phase – and thus effectively scrambling the signal. The probability to relax during the pulse is $[1-\exp(-\Gamma_t t_p)]$. When returning to the original coupling strength $\alpha_2 \rightarrow \alpha_1$ the relaxation induced coherent oscillations have the same amplitude as the wanted ones but a different frequency $\Omega_2 \approx \Omega_1 \alpha_1/\alpha_2$ (for $\delta \approx 0$). During the long read-out phase ($t_o \sim \Gamma_R^{-1}$) this oscillation cycles through many periods because $\Gamma_R \ll \Omega$. Thus, the average probability to find the system in state $\Psi^+_{\alpha_1}$ after relaxation (Γ_1) took place is $P_{\max}/2$, leading to the total probability

$$P = \underbrace{e^{-\Gamma_1 t_p} P(t_p)}_{\text{no relax.}} + \underbrace{\left(1 - e^{-\Gamma_1 t_p}\right) \frac{P_{\max}}{2}}_{\text{relax.}}. \tag{3.50}$$

Therefore, the dephasing during the rotation phase leads to an exponential damping of the oscillation features in the current towards the average value $e\Gamma_R P_{\max}/2$. Since $P(t_p)$ is a periodic function of frequency Ω, oscillations should be observable for $\Gamma_1 \ll \Omega$.

3.3.2 Phonon induced relaxation rates

Due to the hybridisation of spin and orbital wavefunction in the JCM, the question arises whether dissipation to phonons which couple to the orbital wavefunction might lead to relaxation from the excited state Ψ^+ to the ground state Ψ^-, and thus cancelling the robustness of pure spin qubits. We now show that the hybridisation indeed leads to an addition relaxation channel, but that the corresponding rate is small enough that coherent oscillation still may be observed.

The potential which is induced by a bulk acoustic phonon with (three-dimensional) wave vector $\mathbf{q}$ is given by [139]

$$V_{\mathrm{ep}}(\mathbf{q}) = \lambda_{\mathbf{q}}\, e^{i\mathbf{q}\cdot\mathbf{r}}\left(b_{\mathbf{q}} + b^{\dagger}_{-\mathbf{q}}\right), \tag{3.51}$$

with the phonon operators $b_{\mathbf{q}}$ and $b^{\dagger}_{\mathbf{q}}$, and the coupling parameter $\lambda_{\mathbf{q}}$ depending on the mechanism of electron-phonon interaction, e.g. deformation potential or piezo-electric coupling.[§]

In the following, we are interested in phonon-induced transitions from the upper to the lower eigenstate within a JCM subspace, representing excited and ground state of the qubit under consideration, $\Psi^{+} \to \Psi^{-}$, with $\Psi^{\pm}$ given by Eq. (3.29). Since the electron-phonon interaction does not depend on the spin, only transition matrix elements which are diagonal in spin space contribute,

$$\begin{aligned}\langle\Psi^{+}|V_{\mathrm{ep}}(\mathbf{q})|\Psi^{-}\rangle = {}& \cos\theta_{+}\cos\theta_{-}\,\langle n_{+}, n_{-}, \uparrow |V_{\mathrm{ep}}(\mathbf{q})| n_{+}, n_{-}, \uparrow\rangle \\ & + \sin\theta_{+}\sin\theta_{-}\,\langle n_{+}, n_{-}+1, \downarrow |V_{\mathrm{ep}}(\mathbf{q})| n_{+}, n_{-}+1, \downarrow\rangle. \end{aligned} \tag{3.52}$$

In appendix B, matrix elements of the electron-phonon interaction are calculated in the Fock–Darwin basis $\{|n_{+}, n_{-}, \sigma\rangle\}$, leading to

$$\begin{aligned}\langle\Psi^{+}|V_{\mathrm{ep}}(\mathbf{q})|\Psi^{-}\rangle = {}& \lambda_{\mathbf{q}}\,\mathrm{L}_{n_{+}}\!\left(|\alpha^{+}_{\mathbf{q}}|^2\right)\, e^{-\frac{1}{2}\left(|\alpha^{+}_{\mathbf{q}}|^2 + |\alpha^{-}_{\mathbf{q}}|^2\right)} \\ & \times \left[\cos\theta_{+}\cos\theta_{-}\,\mathrm{L}_{n_{-}}\!\left(|\alpha^{-}_{\mathbf{q}}|^2\right) + \sin\theta_{+}\sin\theta_{-}\,\mathrm{L}_{n_{-}+1}\!\left(|\alpha^{-}_{\mathbf{q}}|^2\right)\right], \end{aligned} \tag{3.53}$$

with the Laguerre polynomials L_n and complex phonon wave vectors $\alpha^{\pm}_{\mathbf{q}} := \pm\tilde{l}(q_y \pm i q_x)/2$. For the ease of computation we concentrate on the lowest qubit, $n_{+} = n_{-} = 0$. Generalisation to higher qubits is straightforward. With $\mathrm{L}_0(x) = 1$ and $\mathrm{L}_1(x) = 1 - x$ we have

$$\begin{aligned}\langle\Psi^{+}_{0}|V_{\mathrm{ep}}(\mathbf{q})|\Psi^{-}_{0}\rangle = {}& \lambda_{\mathbf{q}}\, e^{-\frac{1}{2}\left(|\alpha^{+}_{\mathbf{q}}|^2 + |\alpha^{-}_{\mathbf{q}}|^2\right)}\Big[\cos\theta_{+}\cos\theta_{-} + \sin\theta_{+}\sin\theta_{-} \\ & - |\alpha^{-}_{\mathbf{q}}|^2 \sin\theta_{+}\sin\theta_{-}\Big]. \end{aligned} \tag{3.54}$$

The $\mathbf{q}$-independent summand on the right vanishes because of the orthogonality of $\Psi^{\pm}_{0}$,

$$\cos\theta_{+}\cos\theta_{-} + \sin\theta_{+}\sin\theta_{-} = \langle\Psi^{+}_{0}|\Psi^{-}_{0}\rangle = 0, \tag{3.55}$$

leading to

$$\langle\Psi^{+}_{0}|V_{\mathrm{ep}}(\mathbf{q})|\Psi^{-}_{0}\rangle = -\lambda_{\mathbf{q}}\sin\theta_{+}\sin\theta_{-}\,\frac{(\tilde{l}q_{\parallel})^2}{4}\, e^{-\frac{1}{4}(\tilde{l}q_{\parallel})^2}, \tag{3.56}$$

[§] An introduction to electron-phonon interaction is given in chapter 5.

with $q_\parallel = (q_x^2 + q_y^2)^{1/2}$. The phonon-induced transition rate can be calculated in first order by Fermi's golden rule,

$$\Gamma_{\text{ep}} = \frac{2\pi}{\hbar} \sum_{\mathbf{q}} \left| \langle \Psi_0^+ | V_{\text{ep}}(\mathbf{q}) | \Psi_0^- \rangle \right|^2 \delta(E_+ - E_- - \hbar\omega_{\mathbf{q}}) \tag{3.57}$$

$$= \frac{\mathcal{V}}{(2\pi)^2 \hbar} \int d^3\mathbf{q} \left| \langle \Psi_0^+ | V_{\text{ep}}(\mathbf{q}) | \Psi_0^- \rangle \right|^2 \delta(\Delta - \hbar\omega_{\mathbf{q}}), \tag{3.58}$$

with $\Delta = E_+ - E_-$, the volume of the system $\mathcal{V}$, and the phonon frequency $\omega_{\mathbf{q}}$.

For low temperatures the electron-phonon interaction is dominated by the piezo-electric coupling to long-wavelength bulk (3D) acoustic phonons, see chapter 5. We follow Ref. [111, 140] and apply an angular average of the anisotropic piezo-electric modulus for zinc blende crystal structures, leading to the coupling parameter [141]

$$|\lambda_{\mathbf{q}}|^2 = \frac{1}{\mathcal{V}} \frac{\lambda_{\text{ph}}^2}{cq}, \quad \lambda_{\text{ph}}^2 = \frac{\hbar P}{2\rho_M}, \tag{3.59}$$

where c is the longitudinal velocity of sound, $\omega_{\mathbf{q}} = cq = c(q_\parallel^2 + q_z^2)^{1/2}$ is the phonon dispersion, ρ_M the mass density of the semiconductor, and P the averaged piezo-electric coupling [140]

$$P = (eh_{14})^2 \left(\frac{12}{35} + \frac{1}{x} \frac{16}{35} \right), \tag{3.60}$$

with the piezo-electric constant eh_{14} and the sound velocity ratio $x = c_{\text{trans}}/c_{\text{long}}$.

With this model of the electron-phonon interaction, the phonon-induced relaxation rate Eq. (3.58) can be written as (see appendix C)

$$\frac{\Gamma_{\text{ep}}}{\omega_0} = \frac{mP}{8\pi(\hbar\omega_s)^2 l_0 \rho_{\text{M}}} \frac{\sqrt{2} l_0}{\tilde{l}} \sin^2\theta_+ \sin^2\theta_- \xi^5 I(\xi), \tag{3.61}$$

with the characteristic acoustic frequency $\omega_s = c/l_0$ and the ratio $\xi = 2^{-1/2}(\tilde{l}/l_0)(\Delta/\hbar\omega_s)$. The function $I(\xi) = \int_0^1 dt \, \exp[-(\xi t)^2] t^5/(1-t^2)^{1/2}$ is evaluated in appendix C and can be estimated by $I(\xi) \leq 8/15$ for $\xi < 1$.

The rotating-wave approximation (RWA) which is applied to derive the effective model in Sec. 3.2.3 requires the SO coupling to be small compared to the confinement. In addition, to observe coherent oscillations the system needs to be driven close to resonance (see Sec. 3.2.4). In this regime, the energy ratio is $\Delta/\hbar\omega_s \ll 1$, leading to $\xi \ll 1$, and thus suppressing the phonon-induced relaxation due to $\Gamma_{\text{ep}} \propto \xi^5$, see Eq. (3.61). On the contrary, for $\xi \gg 1$ (corresponding

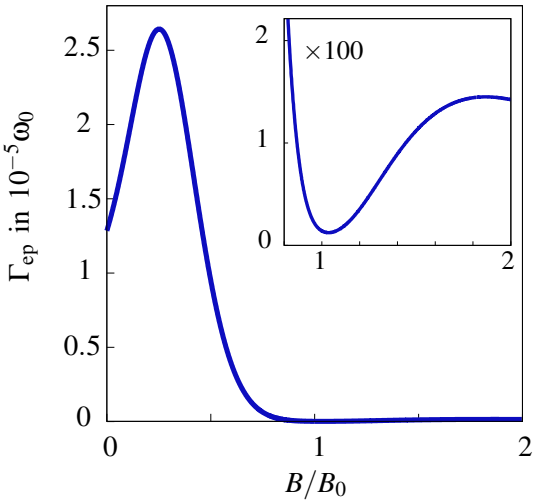

Figure 3.7: Phonon-induced relaxation rate for InAs quantum dot. Close to $B = B_0$ the rate is strongly suppressed to $\Gamma_{ep} < 10^{-7}\omega_0 \approx 10^4\,\mathrm{s}^{-1}$.

to a strongly detuned system) the exponential decay of $I(\xi)$ also suppresses the rate (see appendix C).

The suppression of the relaxation rate close to the resonance can be traced back to the factor ξ^5 in Eq. (3.61) which in turn originates from the $\mathbf{q}$-dependence of the matrix element (3.56). In a physical sense, this matrix element is a measure for how the coupling to phonons modifies the overlap of previously orthogonal states. Equations (B.4) and (B.5) in App. B show that the interaction with phonons leads to a displacement of the Fock–Darwin states in the QD. The effectiveness of this displacement on the orbital overlap manifests itself in the aforementioned $\mathbf{q}$-dependence of Eq. (3.56), showing the overlap to be maximal at $\tilde{l}q_{\|} \approx 1$. Thus, phonons couple most strongly to electrons if their wavelength is comparable to the size of the QD, or in terms of energy, if the typical phonon energy is of order $\hbar\omega_s$.

Close to resonance, however, the splitting of eigenstates Δ is given by the weak SO coupling, leading to $\Delta \ll \hbar\omega_s$. In this regime phonons couple very inefficiently to the electrons of the QD – thus causing the relaxation rate to be suppressed.

The factor $\sin\theta_+ \sin\theta_-$ in Eq. (3.56) corresponds to the misalignment of spin. Since the electron-phonon interaction (3.51) does not lead to direct spin flips, transitions between $\psi_\pm$ are only possible due to the spin admixture of the JCM eigenstates. This admixture is maximal at resonance with $\sin^2\theta_\pm = 1/2$. Far from resonance $\psi_{+(-)}$ are approximately spin-up(down) like, suppressing the transition rate by the factor $\sin^2\theta_+ \sin^2\theta_-$.

For a quantitative analysis we introduce acousto-mechanical parameters of bulk InAs [142], $\rho_M = 5.7 \cdot 10^3\,\mathrm{Kg/m}^3$, $c_{\mathrm{long}} = 3.8 \cdot 10^3\,\mathrm{m/s}$, $c_{\mathrm{trans}} = 2.6 \cdot 10^3\,\mathrm{m/s}$,

$eh_{14} = 3.5 \cdot 10^6\, e\mathrm{V/cm}$, leading to a piezo-electric coupling $P = 3.0 \cdot 10^{-21}\,\mathrm{J^2/m^2}$ by Eq. (3.60).[¶] For our QD size of $l_0 = 150\,\mathrm{nm}$ (corresponding to $\omega_0 = 10^{11}\,\mathrm{Hz}$) the characteristic acoustic frequency is $\omega_s = c/l_0 = 2.5 \cdot 10^{10}\,\mathrm{Hz}$. The dimensionless prefactor in Eq. (3.61) can be evaluated to $mP/8\pi(\hbar\omega_s)^2 l_0 \rho_\mathrm{M} \approx 10^{-3}$.

The magnetic field dependence of the phonon-induced relaxation rate is shown in Fig. 3.7 (see Fig. 3.3c for log-scale plot) for a SO coupling strength $\alpha = 1.5 \times 10^{-12}\, e\mathrm{Vm}$. Close to the resonance the rate is strongly suppressed, $\Gamma_\mathrm{ep} < 10^{-7}\omega_0 \approx 10^4\,\mathrm{s^{-1}}$. Comparison with the Rabi frequency of 2 GHz (see Sec. 3.2.4) shows that the robustness of pure spin qubits is not significantly weakened by the SO-induced hybridisation to the orbital degree of freedom.

There are, of course, further sources of decoherence in any experimental realisation. For example, background charge fluctuations and noise in the gate voltages of the device affect the electrostatic definition of the quantum dot and hence the detuning δ. In addition, higher order (co-tunnelling) processes may scatter the states during the coherent evolution period.

These additional mechanisms were also present in the experiment of Hayashi *et al.* [7], which demonstrated the general feasibility of observing coherent oscillations in quantum dots on a nanosecond time scale. The feasibility of our proposal is enhanced over and above this by the following considerations. Firstly, we work with a perpendicular magnetic field, and thus the confinement of the electron is not wholly electrostatic and thus more robust against charge/voltage fluctuations. Also, in the Hayashi experiment, a rather strong coupling to the leads is applied. Since we use weak coupling, the effects of co-tunnelling are further reduced.

Finally, we point out that the counter-rotating terms which are neglected in the rotating-wave approximation in section 3.2.3, do not induce additional first order relaxation transitions. This is because counter-rotating terms couple to states which are beyond the two levels in a JCM-subspace.

[¶]For comparison, the value for bulk GaAs is $P_\mathrm{GaAs} = 5.4 \cdot 10^{-20}\,\mathrm{J^2/m^2}$.

Chapter 4

Conclusion

In this part of the thesis we have investigated the effect of Rashba spin-orbit coupling on parabolically confined nanostructures for the example of quantum wires and few-electron quantum dots. In these systems the orbital motion is strongly restricted due to the confinement which leads to characteristic spectral properties. Since the spin-orbit interaction couples spin and orbital degrees of freedom, the question arises, how the confinement induced modification of the orbital motion affects the spin state of electrons in the nanostructure. This is of special interest in the context of spintronics, where the spin is envisioned as an extension of even substitute of the electron charge in future electronic devices.

In chapter 2, we investigated the combined effect of geometric confinement, spin-orbit coupling, and magnetic field in quantum wires. In this interplay, the calculated one-electron spectral and spin properties show a rich variety of characteristics. These properties are governed by a compound spin orbital-parity symmetry. Without magnetic field this spin parity – which is a characteristic property of any symmetrically confined quasi-1D system with Rashba effect – is shown to replace the quantum number of spin. It is also responsible for the well-known degeneracy at $k = 0$ in symmetrically confined systems with Rashba effect. A non-vanishing magnetic field breaks the spin-parity symmetry, thus lifting the corresponding degeneracy at $k = 0$. We show that this magnetic field induced energy splitting can become much larger than the Zeeman splitting and should be experimentally accessible by means of optical or transport measurements. In addition, hybridisation effects of the spin density go along with the symmetry breaking.

The one-electron spectrum is shown to be very sensitive to weak magnetic fields. Spin-orbit induced modifications of the subband structure of the quantum wire are strongly altered when the magnetic length becomes comparable to the confinement. In the context of spintronics, this might imply consequences for spin-field-effect-transistor designs which depend on spin injection from ferromagnetic contacts because of magnetic stray fields.

Instancing the quantum wire, we showed that for parabolically confined nanostructures, it is helpful to map the underlying one-electron model onto a bosonic representation, which highlights the effects of spin-orbit coupling in confined systems and shows many similarities to models of quantum optics. Following this reasoning, in chapter 3, we discussed the effect of spin-orbit coupling in few-electron quantum dots. Starting from standard Fock–Darwin theory for one-electron dots and including the Rashba Hamiltonian, an approximate model is derived by making an analogy with quantum optics. When the spin-orbit coupling becomes weaker than the dot confinement, the effective model is shown to be formally identical to the Jaynes–Cummings model (JCM) of atom-light interaction, and its integrability provides valuable insight into the coupling between spin and orbital degrees of freedom in the quantum dot. In comparison to the JCM of quantum optics, here the roles of atomic pseudo-spin and quantised light field are played by the spin and orbital angular momentum of the same electron.

The excitation spectrum of the dot exhibits anticrossings as a characteristic signature of spin-orbit coupling, which goes along with a decomposition into two-level systems, any of which can be considered as a novel compound spin-angular momentum qubit degree of freedom. We predict that the width of the anticrossing is proportional to $\alpha\sqrt{n+1}$ with the strength of the spin-orbit coupling α and the index of crossing n. The measurement of this relation would be verification of our effective model and opens a unique way to determine the spin-orbit parameter in quantum dots.

By applying the constant-interaction model we have translated results from the single to the few-electron dot case. In addition, an experimentally feasible proposal for the observation of coherent oscillations in the electron transport through the quantum dot is outlined. The oscillations within the new qubit degree of freedom are spin-orbit driven by utilising that the strength of the spin-orbit coupling can be changed non-adiabatically by applying a voltage pulse to the system. For parameters corresponding to an InGaAs dot, a Rabi frequency of 2 GHz and an amplitude of current oscillations of up to 45% are calculated, both being within accessible ranges of state-of-the-art experimental technique.

Due to the incorporation of the spin-orbit coupling into the dynamics of the dot, the dominating spin relaxation mechanisms in quantum dots are suppressed. In addition, it is shown that the hybridisation of spin and orbital wavefunction in the eigenstates of the qubit does not increase the fragility of the system in the case of dissipation to phonons. Due to the design of the qubit states, the coupling to long wavelength acoustic phonons is shown to be strongly suppressed, leading to a relaxation rate $\Gamma_{\mathrm{ep}} \leq 10^{-4}\omega_0$ with dot energy $\hbar\omega_0$. Thus, the residual relaxation time is expected to be sufficiently long to observe the coherent evolution of the qubit in the time domain.

Tuneable quantum dots connected to leads are still to be realised in material systems with substantial Rashba effect (e.g. InGaAs). However, the steady progress in the field of nanotechnology suggests that this goal might be reached in the near future. In such systems, the interwoven nature of eigenstates, being hybrids of spin and orbital degree of freedom, will open an appealing perspective on measuring how the transport and dephasing properties of quantum dots change when the Hilbertspace cannot be separated into two subsystems.

Part II

Phonon confinement in nanostructures

Chapter 5

Introduction to electron-phonon interaction

In a solid, vibrational excitations of the crystal lattice are describes as the creation of phonons. These quasi-particles have, like electrons, a definite energy dispersion $E_s(\mathbf{q}) = \hbar\omega_s(\mathbf{q})$, where $\mathbf{q}$ is the wave vector of the phonon, ω is its frequency, and s denotes the different phonon branches (acoustic or optical), and polarisations (longitudinal or transversal). Electron scattering by crystal lattice vibrations is then described by emission and absorption of phonons.

In the following, we are interested in the low-energy and low-temperature properties of electron-phonon scattering. Therefore, we restrict ourselves to single-phonon scattering events with long wavelength acoustic phonons. Excitation energies of optical phonons are typically on a much higher energy scale, e.g. in GaAs the lowest optical phonon excitation has an energy of more than 30 meV [142]. In this introduction we follow the presentation of Ref. [139]. A discussion of the scattering by optical phonons and the effect of multi-phonon processes, which we omit in this context, can also be found there.

In general, any deformation of the crystal lattice may induce a perturbation $\delta V(\mathbf{r},t)$ of the potential in which the electron moves. Independent of the actual microscopic mechanisms, this perturbation can be written in linear order in the deformation as

$$\delta V(\mathbf{r},t) = \sum_{\mathbf{a}} \mathbf{V}_{\mathbf{a}}(\mathbf{r}) \cdot \mathbf{u}_{\mathbf{a}}(t), \tag{5.1}$$

where $\mathbf{u}_{\mathbf{a}}(t)$ is the displacement of the atom at lattice site $\mathbf{a}$ in the crystal. The vector components $V^i_{\mathbf{a}}(\mathbf{r})$ describe the change in lattice potential at site $\mathbf{r}$ for a unit displacement of atom $\mathbf{a}$ along the i-direction. If we denote the eigenmodes of

vibrations of atom **a** of the crystal with $(\mathbf{u_a})_{s\mathbf{q}}$, we can write the displacement as

$$\mathbf{u_a}(t) = \sum_{s,\mathbf{q}} \left[a_{s\mathbf{q}} \, (\mathbf{u_a})_{s\mathbf{q}} \, e^{-i\omega_{s\mathbf{q}} t} + \text{c.c.} \right]. \tag{5.2}$$

After quantisation of the acoustical problem which determines $(\mathbf{u_a})_{s\mathbf{q}}$, the coefficients in expansion (5.2) correspond to creation and annihilation operators, $a_{s\mathbf{q}}$ and $a^{\dagger}_{s\mathbf{q}}$, of a phonon in mode $(s\mathbf{q})$. Combining Eqs. (5.2) and (5.1) yields

$$\delta V(\mathbf{r},t) = \sum_{s,\mathbf{q}} \left[a_{s\mathbf{q}} \sum_{\mathbf{a}} \mathbf{V_a}(\mathbf{r}) \cdot (\mathbf{u_a})_{s\mathbf{q}} \, e^{-i\omega_{s\mathbf{q}} t} + \text{h.c.} \right] \tag{5.3}$$

$$=: \sum_{s,\mathbf{q}} \left[V_{s\mathbf{q}}(\mathbf{r}) \, a_{s\mathbf{q}} \, e^{-i\omega_{s\mathbf{q}} t} + \text{h.c.} \right]. \tag{5.4}$$

We can regard $V_{s\mathbf{q}}(\mathbf{r})$ as the perturbation which an electron experiences when a phonon in mode $(s\mathbf{q})$ is present. With this understanding, phonon induced transition probabilities between different electron states $(l\mathbf{k})$ can be calculated by Fermi's golden rule

$$W^{\pm s\mathbf{q}}_{l\mathbf{k}\to l'\mathbf{k}'} = \frac{2\pi}{\hbar} \left| M^{\pm s\mathbf{q}}_{l\mathbf{k}\to l'\mathbf{k}'} \right|^2 \left(N_{s\mathbf{q}} + \frac{1}{2} \pm \frac{1}{2} \right) \delta\left(\varepsilon_{l\mathbf{k}} - \varepsilon_{l'\mathbf{k}'} \mp \hbar\omega_{s\mathbf{q}} \right), \tag{5.5}$$

with matrix elements

$$M^{-s\mathbf{q}}_{l\mathbf{k}\to l'\mathbf{k}'} = \int_{\mathcal{V}} d^3\mathbf{r} \, \psi^*_{l'\mathbf{k}'}(\mathbf{r}) V_{s\mathbf{q}}(\mathbf{r}) \psi_{l\mathbf{k}}(\mathbf{r}) = \left(M^{+s\mathbf{q}}_{l'\mathbf{k}'\to l\mathbf{k}} \right)^*. \tag{5.6}$$

The Bose factors $N_{s\mathbf{q}} = 1/[\exp(\hbar\omega_{s\mathbf{q}}/K_{\mathrm{B}}T) - 1]$ mark the different probabilities for phonon absorption ($W^{-s\mathbf{q}}_{l\mathbf{k}\to l'\mathbf{k}'} \propto N_{s\mathbf{q}}$) and emission ($W^{+s\mathbf{q}}_{l\mathbf{k}\to l'\mathbf{k}'} \propto N_{s\mathbf{q}} + 1$) [induced and spontaneous emission]. From Eq. (5.5) follows that spontaneous emission of phonons leads to electron scattering even at $T = 0$, provided that the electrons are not in equilibrium.

To evaluate Eqs. (5.5) and (5.6) we need to know the electron wavefunctions $\psi_{l\mathbf{k}}(\mathbf{r})$ and the potential $V_{s\mathbf{q}}(\mathbf{r})$. The latter depends on the eigenmodes of vibration and their induced interaction potential, see Eqs. (5.3) and (5.4). So far we explicitly paid attention to the lattice structure of the solid. When we average δV over an area of the crystal which is larger than the lattice constant a_0 but smaller than the phonon wavelength $\lambda \sim 1/q$, we can decompose δV into

$$\delta V = \delta\bar{V} + \delta\tilde{V}. \tag{5.7}$$

Here, $\delta\bar{V}$ is the averaged potential and $\delta\tilde{V}$ describes the fluctuations which average to zero. The physical effect of both terms on the electron is different: $\delta\tilde{V}$ is a

microscopically fluctuating field which leads to a change in the band structure of the electron, whereas the *macroscopic* $\delta\bar{V}$ changes the energy on a larger length scale [139]. In piezo-electric materials the macro-field $\delta\bar{V} =: e\varphi$ is determined by the polarisation via Poission's equation

$$\boldsymbol{\nabla}^2\varphi(\mathbf{r}) = 4\pi\boldsymbol{\nabla}\cdot\mathbf{P}(\mathbf{r}). \tag{5.8}$$

The polarisation $\mathbf{P}$, on the other hand, is given in lowest order in the strain tensor u_{ij} by

$$P_\nu = \beta_{\nu,ij}\,u_{ij}, \quad u_{ij} = \frac{1}{2}\left(\frac{\partial u_i}{\partial r_j} + \frac{\partial u_j}{\partial r_i}\right), \tag{5.9}$$

with the piezo-electric modulus β. Here, we have introduced the displacement field $\mathbf{u}(\mathbf{r})$ as a substitute for $\mathbf{u_a}$ in the limit of a homogenous solid. This limit is certainly fulfilled when considering long wavelength phonons with $\lambda \gg a_0$.

In addition to the piezo-electric potential φ which depends on the polarisation as a macroscopic quantity, the effect of the microscopically fluctuating $\delta\tilde{V}$ can be parametrised by the deformation potential

$$V_{\text{def}}(\mathbf{r}) = \sum_{ij}\Xi_{ij}u_{ij}(\mathbf{r}), \tag{5.10}$$

with the tensor of deformation potential constants Ξ. For cubic crystals, which we consider for simplicity, this tensor becomes highly symmetric [139], $\Xi_{ij} = \delta_{ij}\Xi$, leading to

$$V_{\text{def}}(\mathbf{r}) = \Xi\,\boldsymbol{\nabla}\cdot\mathbf{u}(\mathbf{r}). \tag{5.11}$$

In the theory of elasticity [143], the divergence of the displacement field is shown to be equivalent to the relative local change of the volume of the solid, $\Delta\mathcal{V}/\mathcal{V} = \boldsymbol{\nabla}\cdot\mathbf{u}(\mathbf{r})$. Thus, phonons which correspond to an equivoluminal deformation of the solid do not interact with electrons via the deformation potential coupling.

The piezo-electric and deformation potential Eqs. (5.8) and (5.11) are the dominating sources of electron-phonon scattering at low energies. Here, we treat β and Ξ as phenomenological constants which are to be determined in experiment.

For calculating the interaction potentials (5.8) and (5.11) we need to know the displacement fields $\mathbf{u}(\mathbf{r})$ for the eigenmodes of vibration. In the classical theory of elasticity, for a homogenous medium these modes are determined by a 'generalised wave equation' [144]

$$\frac{\partial^2}{\partial t^2}\mathbf{u}(\mathbf{r},t) = c_t^2\boldsymbol{\nabla}^2\mathbf{u}(\mathbf{r},t) + \left(c_l^2 - c_t^2\right)\boldsymbol{\nabla}(\boldsymbol{\nabla}\cdot\mathbf{u}(\mathbf{r},t)), \tag{5.12}$$

with the transversal and longitudinal velocities of sound c_t and c_l, respectively. For bulk media follows that the eigenmodes are given by plane waves ($s\mathbf{q}$),

$$\mathbf{u}(\mathbf{r},t) = \sum_{s,\mathbf{q}} \hat{\mathbf{u}}_s(\mathbf{q})\, e^{i\left(\mathbf{q}\cdot\mathbf{r}-\omega_{s\mathbf{q}}t\right)}, \tag{5.13}$$

where $s = \{l,t\}$ denotes the different longitudinal and transversal polarisations, and $\hat{\mathbf{u}}_s(\mathbf{q})$ is the corresponding polarisation vector. With proper normalisation one can show that the bulk matrix elements (5.6) for the absorption of a phonon ($s\mathbf{q}$) via deformation and piezo-electric potentials are given by [139]

$$M^{\mathrm{def}}_{l\mathbf{k}\to l'\mathbf{k}'} = \delta_{\mathbf{k}',\mathbf{k}+\mathbf{q}} \frac{1}{\sqrt{\mathcal{V}}} \left[\frac{\hbar}{2\rho_{\mathrm{M}} c_s}\right]^{\frac{1}{2}} i\Xi\sqrt{q}, \tag{5.14}$$

$$M^{\mathrm{pz}}_{l\mathbf{k}\to l'\mathbf{k}'} = \delta_{\mathbf{k}',\mathbf{k}+\mathbf{q}} \frac{1}{\sqrt{\mathcal{V}}} \left[\frac{\hbar}{2\rho_{\mathrm{M}} c_s}\right]^{\frac{1}{2}} \frac{e\beta}{\sqrt{q}}. \tag{5.15}$$

We mention two important points. (i) The phase difference of $\pi/2$ between the matrix elements shows that the piezo-electric and deformation potentials are indeed independent scattering mechanisms, hence they do not interfere. (ii) Comparison of the amplitudes of the matrix elements yields,

$$\frac{|M_{\mathrm{pz}}|^2}{|M_{\mathrm{def}}|^2} = \left(\frac{e\beta}{\Xi q}\right)^2. \tag{5.16}$$

Thus, in piezo-electric bulk materials, the scattering of electrons by long wavelength ($q \to 0$) acoustic phonons is typically dominated by the piezo-electric coupling potential.

Chapter 6

Coupled quantum dots in a phonon cavity

Quantum coherence has become a major issue in the study of electronic transport of low-dimensional artificial structures. It can be observed on length scales of the order of or smaller than the dephasing distance. The latter is the mean distance an electron can propagate within the dephasing time which is determined by scattering processes that destroy the quantum phase.

Generally, the dephasing time depends on temperature. For high temperatures, phase breaking scatterings are so frequent that quantum signatures are completely absent in the electron transport. Only at sufficiently low temperature, scattering events become rare. Then, quantum coherence is maintained over long periods of time such that interference effects can be observed in the current transport. An important fundamental question is whether or not one can control the coupling to phase breaking modes "coherently" such that interference effects due to the coupling itself become experimentally accessible.

Recently, the coupling of semiconductor quantum dots [145–148] has turned out to be a promising method for preparing and controlling superpositions of electronic states. If two dots are coupled to each other and to external leads, Coulomb blockade guarantees that only one additional electron at a time can tunnel between the dots and the leads. Dephasing at very low temperature then is energetically possible only by bosonic low-energy excitations of the environment. It has turned out that the coupling to low-energetic phonons governs the dynamics of double quantum dots (DQDs) [147, 148] since they are essentially realisations of two-level systems within a semiconductor host material [149].

Therefore, a logical step towards the control of dephasing in DQDs is the control of the vibrational properties of such structures. Enormous progress has been made in the fabrication of partly suspended or free-standing nanostructures ("phonon cavities") [150–153]. These considerably differ in their mechanical

properties from bulk material [13]. For example, phonon modes split into several subbands, and quantisation effects become important for the thermal conductivity [154–159]. The observation of coherent phonons in quantum dots [160] or phonons in nanotubes [161] are other examples of low-dimensional systems where phonons are no longer a mere source of dissipation but rather become controllable and the subjects of research themselves.

As bosonic excitations, phonons are also candidates for the realisation of mechanical counterparts of quantum optical phenomena [162], for instance the generation of non-classical squeezed states [163–166] by time-dependent or non-linear interactions with electrons.

Double quantum dots have been found to spontaneously emit phonons that can be traced by non-linear electron transport measurements [147, 148]. They have also been suggested as detectors for high-frequency noise [167]. Furthermore, the successful fabrication of double dots in partly free-standing material was achieved [168], and Coulomb blockade measurements in single quantum dots embedded in a free-standing membrane were reported [169, 170].

In the present part of this thesis, we investigate the effect of phonon confinement on the electron transport properties of DQDs. It turns out that DQDs in phonon cavities can act as very sensitive detectors of the vibrations in the cavity. In particular, we identify typical features of the mechanical confinement such as subband quantisation and van–Hove singularities in the phonon density of states in the inelastic electron current. Therefore, standard transport experiments can be used for phonon spectroscopy. As an instructive example, we calculate quantitatively the current through a DQD which is coupled to the vibrational modes of a homogeneous plate of finite thickness that serves as a model for a nano-size planar phonon cavity. In the following section we present the publication which comprises our main results. In Sec. 6.2 we provide more background information by delineating the models for the double dot and the phonon cavity. Chapter 7 gives the conclusion of the this part of the thesis.

6.1 Control of dephasing and phonon emission in coupled quantum dots*

Abstract: We predict that phonon subband quantisation can be detected in the non-linear electron current through double quantum dot qubits embedded into

*This section has been published as a Rapid Communication in Physical Review B **66**, 041301(R) (2002). E-print: S. Debald, T. Brandes, and B. Kramer, cond-mat/0204444 at www.arxiv.org. This publication has been selected for the 15th July 2002 issue of the Virtual Journal of Nanoscale Science & Technology.

nano-size semiconductor slabs, acting as phonon cavities. For particular values of the dot level splitting Δ, piezo-electric or deformation potential scattering is either drastically reduced as compared to the bulk case, or strongly enhanced due to phonon van Hove singularities. By tuning Δ via gate voltages, one can either control dephasing, or strongly increase emission into phonon modes with characteristic angular distributions.

Coupled semiconductor quantum dots are candidates for controlling quantum superposition and entanglement of electron states. The feasibility of such 'qubits' depends on the control of dephasing due to the coupling to low-energy bosonic excitations of the environment. For example, the electronic transport through double quantum dots is determined by the spontaneous emission of phonons even at very low temperatures [147, 148]. If two dots are coupled to each other and to external leads, Coulomb blockade guarantees that only one electron at a time can tunnel between the dots and the leads. Dephasing in such a 'pseudo spin'-boson system [149, 171] is dominated by the properties of the phonon environment.

As a logical step towards the control of dephasing, the control of vibrational properties of quantum dot qubits has been suggested [147, 148]. Recently, considerable progress has been made in the fabrication of nano-structures that are only partly suspended or even free-standing [152, 153]. They considerably differ in their mechanical properties from bulk material. For example, phonon modes are split into subbands, and quantisation effects become important for the thermal conductivity [154–156]. The observation of coherent phonons in dots [160] in nanotubes [161] are other examples of low dimensional mesoscopic systems where phonons become experimentally controllable and are the objects of interest themselves.

Double quantum dots are not only tunable phonon emitters [147, 148] but also sensitive high-frequency noise detectors [167]. Together with their successful fabrication within partly free-standing nanostructures [168], this suggests that they can be used to control both electrons and phonons on a microscopic scale. This opens a path for realising mechanical counterparts of several quantum optical phenomena, as for instance the generation of non-classical squeezed phonon states [164] by time-dependent or non-linear interactions with the electrons.

In this paper, we demonstrate that phonon confinement can be used to gain control of dissipation in double quantum dots, leading to a considerable reduction of phonon-induced decoherence. More precisely, we show that inelastic scattering and the inelastic current channel for electron transport in the Coulomb blockade regime can be drastically reduced as compared to a bulk environment when double dots are hosted by a semiconductor slab that acts as a phonon cavity. This suppression occurs at specific phonon energies $\hbar\omega_0$ when the level splitting is tuned to $\Delta = \hbar\omega_0$. Furthermore, for larger energy differences ε between the two dot ground

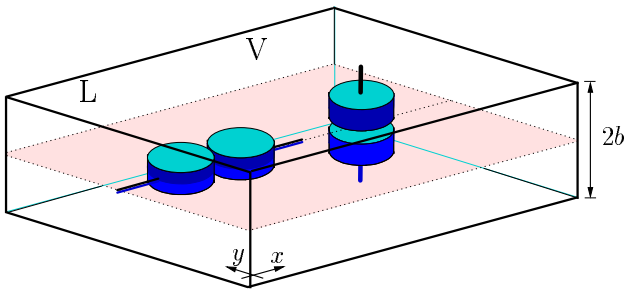

Figure 6.1: Scheme for *lateral* (L) and *vertical* (V) configurations of a double quantum dot in a phonon nano-cavity.

states, typical properties [144, 172] of a nano-size slab such as phonon-subband quantisation can be detected in the staircase-like electronic current $I(\varepsilon)$ though the dots. In addition, and very strikingly, for certain wave vectors we find negative phonon group velocities and phonon van Hove singularities close to which one can strongly excite characteristic phonon modes with specific emission patterns.

The controlled enhancement or reduction of spontaneous light emission from atoms is well-known in cavity QED [173]. Here a single, confined photon mode can be tuned on or off resonance with an atomic transition frequency. In contrast to cavity QED, the vanishing of spontaneous emission in phonon cavities is due to real zeros in the *phonon deformation potential or polarisation fields* rather than gaps in the density of states. This is a peculiar consequence of the boundary conditions for vibration modes which lead to complicated nonlinear dispersions even for homogeneous slabs. As a result, phonon cavities confined in only one spatial direction support a continuous spectrum, and yet suppression of spontaneous emission is possible.

As a model, we consider two tunnel-coupled quantum dots embedded in an infinite semiconductor slab of thickness $2b$ in a vertical or a lateral configuration, Fig. 6.1. The dots are weakly coupled to external leads, and we assume that both the energy difference ε and the coupling strength T_c between the dots can be externally tuned by gate voltages. In the Coulomb blockade regime, we adopt the usual description in terms of three many body ground states [149, 174] $|0\rangle$, $|L\rangle$, and $|R\rangle$ that have no or one additional electron in either of the dots, respectively. The coupling to the phonon environment of the slab is described by an effective spin-boson Hamiltonian

$$\begin{aligned} H &= \frac{\varepsilon}{2}\sigma_z + T_c\sigma_x + \sum_{\mathbf{q}} \hbar\omega_{\mathbf{q}} a^\dagger_{\mathbf{q}} a_{\mathbf{q}} \\ &+ \sum_{\mathbf{q}} (\alpha_{\mathbf{q}} n_L + \beta_{\mathbf{q}} n_R)\left(a_{\mathbf{q}} + a^\dagger_{-\mathbf{q}}\right), \end{aligned} \tag{6.1}$$

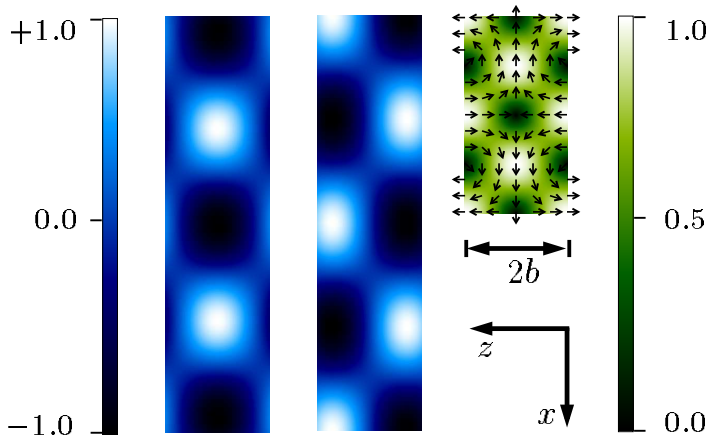

Figure 6.2: Deformation potential induced by dilatational (left) and flexural modes (centre) at $q_\parallel b = \pi/2$ ($n = 2$ subbands). Right: displacement field $\mathbf{u}(x,z)$ of $n = 0$ dilatational mode at $\Delta = \hbar\omega_0$. Greyscale: moduli of deformation potentials (left) and displacement fields (right) (arb. units).

with $\sigma_z = |L\rangle\langle L| - |R\rangle\langle R|$, $\sigma_x = |L\rangle\langle R| + |R\rangle\langle L|$, $n_i = |i\rangle\langle i|$ and $\alpha_\mathbf{q}(\beta_\mathbf{q})$ the coupling matrix element between electrons in dot $L(R)$ and phonons with dispersion $\omega_\mathbf{q}$.

The stationary current can be calculated by using a master equation [149] and considering T_c as a perturbation. We consider weak electron-phonon coupling and calculate the inelastic scattering rate

$$\gamma(\omega) = 2\pi \sum_\mathbf{q} T_c^2 \frac{|\alpha_\mathbf{q} - \beta_\mathbf{q}|^2}{\hbar^2\omega^2} \delta(\omega - \omega_\mathbf{q}). \tag{6.2}$$

For $\hbar\omega = (\varepsilon^2 + 4T_c^2)^{1/2}$ this is the rate for spontaneous emission at zero temperature due to electron transitions from the upper to the lower hybridised dot level.

On the other hand, in lowest order in T_c, the total current $I(\varepsilon)$ can be decomposed into an elastic Breit-Wigner type resonance and an inelastic component $I_\mathrm{in}(\varepsilon) \approx -e\gamma(\varepsilon)$, where $-e$ is the electron charge. The double dot, supporting an inelastic current $I_\mathrm{in}(\varepsilon)$, therefore can be regarded as an analyser of the phonon system [147, 148]. One can also consider the double dot as an emitter of phonons of energy $\hbar\omega$ at a tunable rate $\gamma(\omega)$. We show below how the phonon confinement within the slab leads to steps in $I_\mathrm{in}(\varepsilon)$ and tunable strong enhancement or nearly complete suppression of the electron-phonon coupling.

We describe phonons by a displacement field $\mathbf{u}(\mathbf{r})$ which is determined by the vibrational modes of the slab [143]. For the following, it is sufficient to consider dilatational and flexural modes (Lamb waves). The symmetries of their displacement fields differ with respect to the slab's mid-plane. They either yield a

symmetric elongation and compression (dilatational mode, Fig. 2 left) or a periodic bending associated with an antisymmetric field (flexural mode, Fig. 2 centre). The confinement leads to phonon quantisation into subbands. For each in-plane component $\mathbf{q}_\parallel$ of the wave vector there are infinitely many subbands, denoted by n, related to a discrete set of transversal wave vectors in the direction of the confinement. Since there are two velocities of sound in the elastic medium associated with longitudinal and transversal wave propagation, c_l and c_t, there are also two transversal wave vectors q_l and q_t. This is in contrast to the isotropic bulk where one can separate the polarisations. For a slab, the boundary conditions at the surface lead to coupling between longitudinal and transversal propagation [144, 172].

We have numerically determined the solutions $q_{l,n}(q_\parallel)$ and $q_{t,n}(q_\parallel)$ of the Rayleigh-Lamb equations that describe the dynamics of the confined phonons,

$$\begin{aligned} \frac{\tan q_{t,n}b}{\tan q_{l,n}b} &= -\left[\frac{4q_\parallel^2 q_{l,n}q_{t,n}}{(q_\parallel^2 - q_{t,n}^2)^2}\right]^{\pm 1} \\ \omega_{n,q_\parallel}^2 &= c_l^2(q_\parallel^2 + q_{l,n}^2) = c_t^2(q_\parallel^2 + q_{t,n}^2), \end{aligned} \tag{6.3}$$

together with the dispersion relations $\omega_{n,q_\parallel}$ and the displacement field [175, 176] associated with a confined phonon in mode $(n, \mathbf{q}_\parallel)$. The exponents ± 1 correspond to dilatational and flexural modes, respectively.

The contribution γ_n of subband n to the rate (6.2) is

$$\gamma_n(\omega) = \sum_{\mathbf{q}_\parallel} \frac{|\lambda^\pm_{\mathrm{dp/pz}}(\mathbf{q}_\parallel, n)|^2}{\hbar^2\omega^2} \left|\alpha \pm e^{i\mathbf{q}_\parallel\cdot\mathbf{d}}\right|^2 \delta(\omega - \omega_{n,q_\parallel}) \tag{6.4}$$

where the vector $\mathbf{d}$ connects the dots and λ is the coupling strength of the electron-phonon interaction. We assume that the electron density is sharply peaked near the dot centres and that the dots are located symmetrically within the slab. We consider both the deformation potential (DP), $\alpha = -1$ in (6.4), and piezo-electric (PZ) interaction, $\alpha = +1$. The coupling strength for DP is

$$\lambda^\pm_{\mathrm{dp}}(q_\parallel, n) = B_n^{\mathrm{dp}}(q_\parallel)(q_{t,n}^2 - q_\parallel^2)(q_{l,n}^2 + q_\parallel^2)\,\mathrm{tsc}\, q_{t,n}b\,, \tag{6.5}$$

where $B_n^{\mathrm{dp}} = F_n(\hbar\Xi^2/2\rho\,\omega_{n,q_\parallel}A)^{1/2}$, $\mathrm{tsc}\,x = \sin x$ or $\cos x$ for dilatational and flexural modes, respectively, Ξ is the DP constant, ρ the mass density, A the area of the slab, and F_n normalises the n^{th} eigenmode.

First, we discuss the deformation potential interaction in the vertical configuration (Fig. 6.1), $\mathbf{q}_\parallel \cdot \mathbf{d} = 0$, where only flexural modes couple to the electrons, whereas dilatational modes lead to a symmetrical deformation field (Fig. 6.2 left)

and yield the same energy shift in both of the dots which does not affect the electron tunnelling.

Figure 6.3 (top) shows $\gamma_{\mathrm{dp}}(\omega)$ in units of the nominal scattering rate $\gamma_0 \equiv T_c^2\Xi^2/\hbar\rho c_l^4 b$ for $b = 5d$. The phonon subband quantisation appears as a staircase in $\gamma_{\mathrm{dp}}(\omega)$, with the steps corresponding to the onsets of new phonon subbands. Most strikingly, a van Hove singularity (arrow) occurs due to *zero phonon group velocity* at that frequency. This corresponds to a minimum in the dispersion relation $\omega_{n,q_\parallel}$ for finite $q_\parallel$ with preceding *negative* phonon group velocity due to the complicated non-linear structure of the Rayleigh-Lamb equations for the planar cavity. Additional van Hove singularities occur at higher frequencies (not shown here) as an irregular sequence that can be considered as 'fingerprints' of the phonon-confinement in a mechanical nanostructure.

In the lateral configuration (Fig. 6.1), DP couples only to dilatational modes, in contrast to the vertical case. This is a trivial consequence of the symmetry of the DP of flexural modes (Fig. 6.2 centre) and the fact that in the lateral configuration the dots are aligned mid-plane. The inelastic rate including the lowest 4 modes is shown in Fig. 6.3 (bottom) in comparison to the bulk rate. The phonon-subband quantisation appears as cusps in $\gamma_{\mathrm{dp}}(\omega)$ for $\omega \gtrsim 2\omega_b$. Again, we observe van Hove singularities as fingerprints of the phonon confinement.

Most strikingly, we find a suppression of the inelastic rate at small energies $\hbar\omega$, and even its *complete vanishing* at the energy $\hbar\omega_0 \approx 1.3\hbar\omega_b$ for the lateral configuration. As can be seen from (6.4) and (6.5), the rate γ_0 vanishes for the frequency ω_0 defined by the condition $q_t = q_\parallel$. This is due to a vanishing divergence of the displacement field $\mathbf{u}$ (Fig. 6.2 right) that implies vanishing of DP $\propto \nabla\cdot\mathbf{u}$. Near ω_0, the remaining contribution of the $n = 0$-subband mode is drastically suppressed compared with 3d phonons (Fig. 6.3 bottom, inset).

We checked that this decoupling of electrons and phonons is a generic feature due to the slab geometry, as are the steps and van Hove singularities in γ. For the piezo-electric interaction, our results also reveal a complete vanishing of the inelastic rate γ_{pz} from dilatational phonons at the energy $\hbar\omega_0' \approx 0.7\hbar\omega_b$ where the induced *polarisation field* is zero [177]. Due to the symmetry of the latter, in the vertical and lateral configurations only dilatational and flexural phonons, respectively, couple to the electrons via PZ interaction. Thus, the angular dependence is reversed as compared to the DP case.

An important consequence of these results is that one can 'switch off' either PZ scattering in the vertical configuration, or DP scattering in the lateral configuration at a certain energy. Then, the only remaining electron-phonon scattering is mediated by the other interaction mechanism that couples the electrons to the flexural modes. For other frequencies ω, the ratio $\gamma_{\mathrm{pz}}/\gamma_{\mathrm{dp}} \propto b^2$ can be varied by changing the slab width. Thus, for very small b the DP interaction dominates and the proper choice to 'switch off' the scattering would be the lateral config-

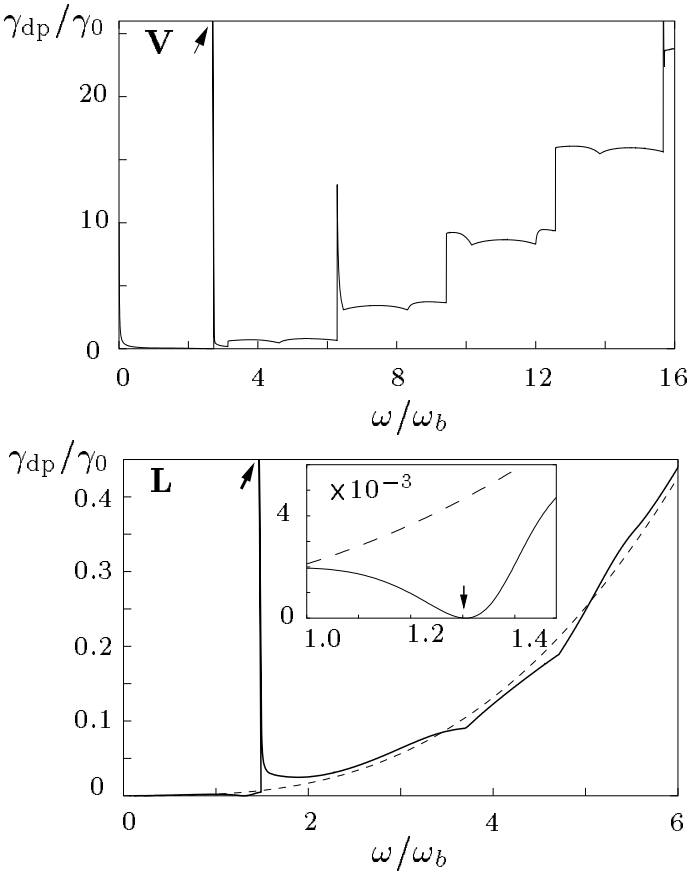

Figure 6.3: Inelastic phonon emission rate $\gamma_{dp}(\omega)$ of vertical (V) and lateral (L) double dots in a phonon cavity of width $2b$ due to deformation potential. Phonon-subband quantisation effects appear on an energy scale $\hbar\omega_b = \hbar c_l/b$ with the longitudinal speed of sound c_l; γ_0 nominal scattering rate (see text). Coupling to *flexural* (top) and *dilatational* modes (bottom, dashed: bulk rate). Inset: Suppression of $\gamma_{dp}(\omega)$ from slab phonons at $\omega = \omega_0$ (arrow).

uration, with a small contribution remaining if the material is piezo-electric, and vice versa. For a GaAs slab of width $2b = 1\mu$m and a tunnel coupling $T_c = 10\mu$eV in the lateral configuration tuned to $\hbar\omega \approx 0.7\hbar\omega_b$ (no PZ coupling), we obtain a residual scattering rate of $\gamma_{dp} = 8 \times 10^4$ s^{-1} from DP-coupling to flexural modes.

The characteristic energy scale for phonon quantum size effects is $\hbar\omega_b \equiv \hbar c_l/b$. Using the same parameters as above, we have $\hbar\omega_b = 7.5\mu$eV in GaAs which is within the limit of energy resolution of recent transport experiments in double dots [147, 148]. A finite slab of lateral dimension L will lead to a broadening of the structures predicted above since the phonons will aquire a life time

$\propto L/c_{l,t}$ which leads to a smearing of fine structures in $\gamma(\omega)$ on an energy scale $\hbar c_{l,t}/L \sim 1\mu$eV for $L = 10b$. Finite temperatures yield a similar broadening on a scale $k_B T$. Therefore, low temperatures (20 mK $\approx 2\mu$eV) are required to resolve the step-like features and the van Hove singularities in the inelastic current I_{in}. We mention that vertically polarised shear waves (which are also eigenmodes of the slab) do not couple to electrons via the DP because the induced local change in volume ($\propto \nabla \cdot \mathbf{u}$) is zero. Fortunately, shear waves also do not change the low frequency decoupling discussed above because the only mode that is accessible at low enough energies is the massless mode (linear dispersion) that does not lead to any piezo-electric polarisation field. However, at higher frequencies shear subbands can contribute to the electron scattering.

The existence of an energy $\hbar\omega_0$ where the electron-phonon interaction vanishes could be used to suppress decoherence in double dot qubit systems with the energy difference $\Delta = \sqrt{\varepsilon^2 + 4T_c^2}$ tuned to $\Delta = \hbar\omega_0$. For example, using gate voltages to tune $T_c(t) = \Delta/2\sin(\Omega t)$, $\varepsilon(t) = \Delta\cos(\Omega t)$ as a function of time defines a one-qubit rotation ('electron from left to right') free of phonon interaction $\propto \gamma(\Delta) = 0$. The condition $\Delta = \hbar\omega_0$ therefore defines a one dimensional 'dissipation-free manifold' (curve) in the T_c–ε parameter space. In particular, a suppression of decoherence could then be exploited in adiabatic electron transfers [178] or adiabatic swapping operations [179] in coupled quantum dots.

We recall, however, that corrections to γ of 4th and higher order in the coupling constant (virtual processes) can lead to a small but final phonon-induced dephasing rate even at $\Delta = \hbar\omega_0$. Moreover, the dephasing due to spontaneous emission of photons, although negligible with respect to the phonon contribution in second order [147, 148], is not altered unless the whole system is embedded into a photon cavity. Similarly, plasmons and electron-hole pair excitations in the leads can lead to dephasing. We suppose that the latter can affect the inter-dot dynamics of the coupled dots only indirectly via coupling to the leads and only weakly contribute to dephasing, as is the case for interactions between dot and lead electrons beyond the Coulomb blockade charging effect.

Alternatively to suppressing dissipation from phonons at certain energies, the van Hove singularities of the same system could be used to enormously enhance the spontaneous emission rate of phonons. The electron current $I_{\text{in}} \approx -e\gamma(\varepsilon)$ at those energies is due to strong inelastic transitions. The term $\left|\alpha \pm e^{i\mathbf{q}_\parallel \cdot \mathbf{d}}\right|^2$ in (6.4) determines the angular phonon emission characteristic of the double dot. Therefore, as a function of energy and orientation, the double dot can be used as an energy selective phonon emitter with well defined emission characteristics.

In conclusion, we have found that phonon confinement is a promising tool for gaining control of dephasing in double quantum dots via phonons. Once this was achieved, it would be possible to study systematically dephasing due to other

mechanisms such as coupling to electronic excitations in the leads. In contrast to cavity QED, where a single, confined photon mode can be tuned on or off resonance with an atomic transition frequency, the vanishing of spontaneous emission in phonon cavities is due to zeros in the *phonon deformation potential or polarisation fields* rather than gaps in the density of states. In addition, we found that phonon emission into characteristic modes can be enormously enhanced due to van Hove singularities that could act as strong fingerprints of the phonon confinement if experimentally detected.

This work was supported by the EU via TMR and RTN projects FMRX-CT98-0180 and HPRN-CT2000-0144, DFG projects Kr 627/9-1, Br 1528/4-1, and project EPSRC R44690/01. Discussions with R. H. Blick, T. Fujisawa, W. G. van der Wiel, and L. P. Kouwenhoven are acknowledged.

6.2 Details*

6.2.1 Model

In this section, we derive the low-temperature current-voltage characteristic of a double quantum dot (DQD) which interacts with a bath of confined phonons in the non-linear transport regime.

We assume that the DQD is weakly coupled to leads. The parameters are chosen such that the transport is dominated by Coulomb blockade. Following Ref. [149], we describe the DQD as a two-level system consisting of one additional electron in either the left, $|L\rangle = |N+1, M\rangle$, or the right dot, $|R\rangle = |N, M+1\rangle$, associated with the energies E_L and E_R. The state $|0\rangle = |N, M\rangle$ denotes the $N+M$ electrons many body ground state of the double dot. Using this basis set for the electron states and defining the operators

$$n_L = |L\rangle\langle L|, \quad n_R = |R\rangle\langle R|, \quad p = |L\rangle\langle R|, \tag{6.6}$$

$$s_L = |0\rangle\langle L|, \quad s_R = |0\rangle\langle R|, \tag{6.7}$$

the Hamiltonian is

$$H = H_0 + H_{\mathrm{T}} + H_{\mathrm{ld}} + H_{\mathrm{ep}}, \tag{6.8}$$

*Parts of the following results have been published in:

S. Debald, T. Vorrath, T. Brandes, and B. Kramer, *Phonons and Phonon Confinement in Transport through Double Quantum Dots*, Proc. 25th Int. Conf. Semicond., Osaka (2000);

T. Vorrath, S. Debald, B. Kramer, and T. Brandes, *Phonon Cavity Models for Quantum Dot Based Qubits*, Proc. 26th Int. Conf. Semicond., Edinburgh (2002);

S. Debald, T. Brandes, and B. Kramer, *Nonlinear Electron Transport through Double Quantum Dots Coupled to Confined Phonons*, Int. Journal of Modern Physics B **17**, 5471 (2003).

with the Hamiltonian of the decoupled components

$$H_0 = E_L n_L + E_R n_R + H_\mathrm{p} + H_\mathrm{leads}, \tag{6.9}$$

the tunnelling Hamiltonian between the dots

$$H_\mathrm{T} = T_c(p + p^\dagger), \tag{6.10}$$

the phonon system

$$H_\mathrm{p} = \sum_{\mathbf{q}} \hbar\omega_{\mathbf{q}} a^\dagger_{\mathbf{q}} a_{\mathbf{q}}, \tag{6.11}$$

the Hamiltonian of the leads

$$H_\mathrm{leads} = \sum_{\mathbf{k}} (\varepsilon^L_{\mathbf{k}} c^\dagger_{\mathbf{k}} c_{\mathbf{k}} + \varepsilon^R_{\mathbf{k}} d^\dagger_{\mathbf{k}} d_{\mathbf{k}}), \tag{6.12}$$

the electron-phonon coupling

$$H_\mathrm{ep} = \sum_{\mathbf{q}} (\alpha_{\mathbf{q}} n_L + \beta_{\mathbf{q}} n_R)(a_{\mathbf{q}} + a^\dagger_{-\mathbf{q}}), \tag{6.13}$$

and the coupling between the leads and the dots

$$H_\mathrm{ld} = \sum_{\mathbf{k}} (V_{\mathbf{k}} c^\dagger_{\mathbf{k}} s_L + W_{\mathbf{k}} d^\dagger_{\mathbf{k}} s_R + \mathrm{h.c.}). \tag{6.14}$$

The coupling between the two dots is parametrised with the tunnel matrix element T_c. The electronic reservoirs of the leads (H_leads) and the phonon environment (H_p) are assumed to be in thermal equilibrium. H_ep describes the interaction[†] of the electrons in the dots with acoustic phonons, $\alpha_{\mathbf{q}}$ and $\beta_{\mathbf{q}}$ are the matrix elements of the interaction potential in the representation of $|L\rangle$ and $|R\rangle$ (see appendix D). Introduction of pseudo-spin operators σ_x and σ_z leads to the effective spin-boson Hamiltonian (6.1) with $\varepsilon = E_L - E_R$.

Applying a dc bias between source and drain, the current through the DQD is determined by the expectation value of the current operator $\hat{I} = ieT_c(p - p^\dagger)$. The current as a function of the energy difference of the dot levels consists of two parts [147, 148], $I = I_\mathrm{el} + I_\mathrm{inel}$. The elastic contribution I_el which arises from resonant tunnelling [181] is dominating the transport around $\varepsilon = 0$. For $\varepsilon > 0$, the current is determined by inelastic contributions due to spontaneous emission of acoustic phonons [147, 148].

[†]The influence of the non-diagonal part of the electron-phonon interaction has been shown to be negligible [149, 180].

Following Ref. [149], for $T = 0$ the stationary inelastic current in lowest order in T_c is given by the frequency-depending inelastic scattering rate, $I_{\text{inel}} \approx -e\gamma$, with

$$\gamma(\omega) \approx 2\pi T_c^2 \rho_{\text{eff}}(\omega), \tag{6.15}$$

$$\rho_{\text{eff}}(\omega) = \sum_{\mathbf{q}} \frac{|\alpha_{\mathbf{q}} - \beta_{\mathbf{q}}|^2}{\hbar^2\omega^2} \delta(\omega - \omega_{\mathbf{q}}), \tag{6.16}$$

where ρ_{eff} is an effective density of states (DOS) of the phonon environment. Every state is weighted by the electron-phonon interaction through the interference term $|\alpha_{\mathbf{q}} - \beta_{\mathbf{q}}|^2/\hbar^2\omega^2$. Brandes & Kramer [149] utilised the interference in the coupling of the individual dots in Eq. (6.15) to explain the oscillatory behaviour of the inelastic current which was found in Ref. [147].

Equation (6.15) shows the direct relation between inelastic current and DOS of the phonon environment. Therefore, a DQD is an ideal tool to investigate peculiar phonon systems like e.g. nanomechanical resonators by means of electron transport. In this section we investigate the influence of a mechanical confinement of the elastic medium on the transport characteristics of an embedded DQD.

Scattering rates for electron-phonon interaction in phonon cavities have been investigated by Stroscio *et al.* [175, 176, 182]. One of the systems they considered was a free-standing quantum well (FSQW) in a slab geometry (see Fig. 6.4) which is confined in the z-direction and widely extended in x- and y-directions. In the following, we use a FSQW with area $A \gg b^2$ as a model for a phonon cavity. We describe vibrations by a displacement field $\mathbf{u}(\mathbf{r},t)$. Assuming a homogenous, isotropic and linear medium of the FSQW, the general solution for the displacement field $\mathbf{u}(\mathbf{r},t)$ is determined by four families of modes – two families of shear waves (vertically and longitudinally polarised), and two families of Lamb waves[‡] (dilatational and flexural waves). Stroscio *et al.* showed that electron scattering by shear waves can be neglected since these modes do not interact with electrons via the deformation potential interaction which is the dominant coupling mechanism in small FSQW [176]. Therefore, in the following, we restrict ourselves to the coupling to dilatational and flexural modes.

A further effect of the phonon confinement is the spectral quantisation in subbands familiar from other confined systems. For each fixed in-plane wave vector $\mathbf{q}_\parallel$ there are infinitely many modes related to a discrete set of transversal wave vectors pointing in the direction of the confinement. Since there are two velocities of sound in the elastic medium, related to longitudinal and transversal wave propagation, c_l and c_t, there are also two transversal wave vectors which we will denote as q_l and q_t. This is in contrast to the unconfined bulk case where one can

[‡]See Ref. [176] and references therein.

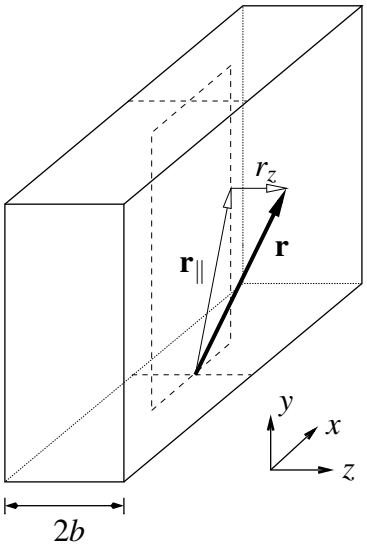

Figure 6.4: Free-standing quantum well (FSQW) as a model for a phonon cavity. The slab is confined in z-direction and widely extended in x- and y-direction.

separate both polarisations. In the confined geometry of the FSQW, the boundary conditions at the surface of the slab lead to a coupling between longitudinal and transversal propagation [172].

The relation between the in-plane wave vector component $\mathbf{q}_\parallel$ and the transversal components q_l and q_t for Lamb waves is determined by the so-called Rayleigh–Lamb equations,

$$\frac{\tan q_{t,n} b}{\tan q_{l,n} b} = -\left[\frac{4 q_\parallel^2 q_{l,n} q_{t,n}}{(q_\parallel^2 - q_{t,n}^2)^2}\right]^{\alpha}, \tag{6.17}$$

$$[\omega_n(q_\parallel)]^2 = c_l^2 (q_\parallel^2 + q_{l,n}^2) = c_t^2 (q_\parallel^2 + q_{t,n}^2), \tag{6.18}$$

where $\alpha = +1$ for dilatational modes and $\alpha = -1$ for flexural modes. The integer $n = 0, 1, 2, \ldots$ denotes the phonon subband index. The second Rayleigh–Lamb equation is the dispersion relation of confined phonons. An analytical solution of the Eqs. (6.17) and (6.18) is in general not feasible, thus a numerical approach has to be applied [172, 175, 182, 183]. Once the solutions $q_{l,n}(q_\parallel)$ and $q_{t,n}(q_\parallel)$ are known, one can calculate the displacement field associated with a confined phonon in a Lamb mode $(n, \mathbf{q}_\parallel)$ that propagates in the x-direction [176],

$$\mathbf{u}_n(q_\parallel, z) = (u_{n,x}, 0, u_{n,z}), \tag{6.19}$$

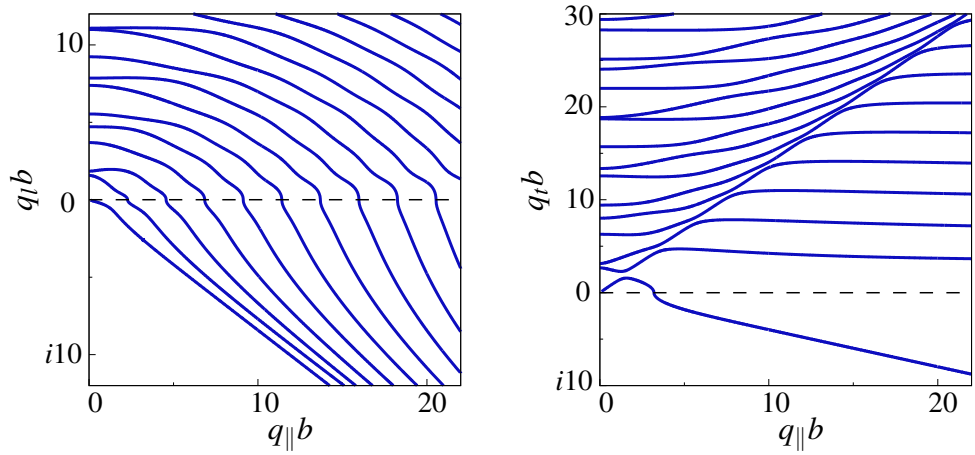

Figure 6.5: Numerical solution of the Rayleigh–Lamb equations for the 16 lowest dilatational modes. Solutions above the abscissae are real, below imaginary.

where

$$u_{n,x} = iq_\parallel \left[(q_\parallel^2 - q_{t,n}^2)\,\mathrm{tsc}\, q_{t,n} b\ \mathrm{tcs}\, q_{l,n} z + 2q_{l,n} q_{t,n}\,\mathrm{tsc}\, q_{l,n} b\ \mathrm{tcs}\, q_{t,n} z \right], \qquad (6.20)$$

$$u_{n,z} = (-\alpha) \left[(q_\parallel^2 - q_{t,n}^2)\,\mathrm{tsc}\, q_{t,n} b\ \mathrm{tsc}\, q_{l,n} z - 2q_\parallel^2\,\mathrm{tsc}\, q_{l,n} b\ \mathrm{tsc}\, q_{t,n} z \right], \qquad (6.21)$$

with $\mathrm{tsc}\, a = \sin a$ for dilatational modes and $\mathrm{tsc}\, a = \cos a$ for flexural modes, $\mathrm{tcs}\, a$ is defined by exchanging sin and cos.

6.2.2 Results

The solutions of the Rayleigh–Lamb Eqs. (6.17) and (6.18) determine the physical properties of Lamb modes which we address in the following.

Assuming that the elastic medium of the cavity is loss free, the solutions $q_{l,n}(q_\parallel)$ and $q_{t,n}(q_\parallel)$ are either real or imaginary as shown in Fig. 6.5. The numerical solutions for flexural modes look similar, see e.g. Ref. [175, 183].

From these solutions and the second Rayleigh–Lamb equation the dispersion relations of confined phonons follow directly,

$$\omega_n(q_\parallel) = \omega_b \sqrt{(q_\parallel b)^2 + (q_{l,n} b)^2}, \quad \omega_b = c_l / b, \qquad (6.22)$$

where ω_b gives the typical energy scale for phonon quantum size effects. The dispersion relations of Lamb modes are shown in Fig. 6.6. It has been shown [172] that the non-linearity (anticrossings) of the dispersion is caused by the coupling of longitudinal and transversal propagation through the boundary conditions at the

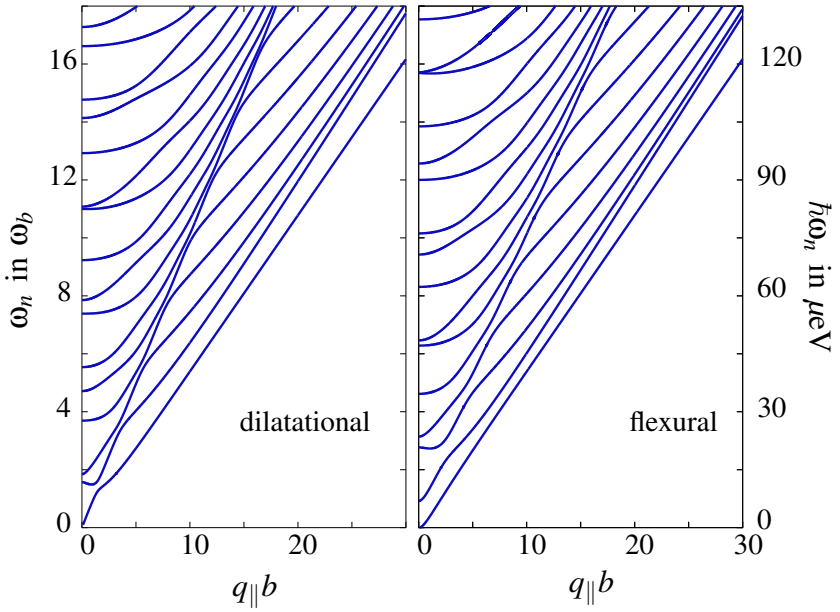

Figure 6.6: Dispersion relations of the 16 lowest dilatational and flexural modes. Energies in units of the characteristic phonon energy scale $\omega_b = c_l/b$ (left) and for a GaAs cavity of width $2b = 1\,\mu$m corresponding to $\hbar\omega_b = 7.5\,\mu$eV (right scale).

surface. For large $q_\parallel$ the dispersion approaches a linear slope as the Lamb modes converge against vertically polarised shear waves.[§]

From the dispersions we obtain the thermodynamical DOS

$$\nu(\omega) = \sum_n \nu_n(\omega) = \sum_n \sum_{\mathbf{q}_\parallel} \delta\big(\omega - \omega_n(q_\parallel)\big)\,, \tag{6.23}$$

which is shown in Fig. 6.7 for flexural and dilatational modes. The subband quantisation manifests itself in the staircase like increase of the curve. Each step corresponds to the onset of a new subband which starts to contribute to the DOS. At the onset of some of the subbands (marked with arrows in Fig. 6.7) *van–Hove singularities* occur, which arise from a vanishing phonon group velocity at finite $\mathbf{q}_\parallel$ – clearly visible as the minima of the dispersions in Fig. 6.6. Since the dispersions of the individual subbands asymptotically approach a linear slope, the total DOS increases super-linearly, converging against the parabolic energy dependence of bulk phonons in the limit of weak confinement.

In the following, we assume that the DQD it is symmetrically placed with respect to the mid-plane of the FSQW (see Fig. 6.1). The interference term $|\alpha_n(\mathbf{q}_\parallel) - \beta_n(\mathbf{q}_\parallel)|^2/\hbar^2\omega^2$ in the effective DOS (6.16) is calculated in appendix D

[§] Vertically polarised means that all displacements are transversal.

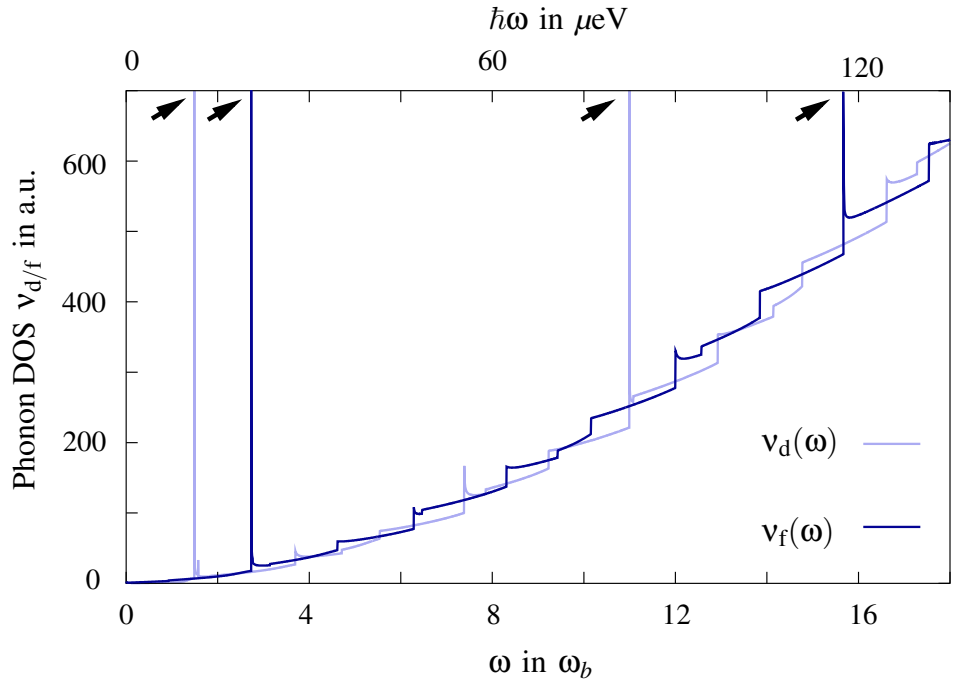

Figure 6.7: Thermodynamical density of states $\nu_{\mathrm{d/f}}$ of dilatational and flexural phonons. The arrows mark van–Hove singularities. Upper energy scale corresponds to a GaAs cavity of width $2b = 1\,\mu$m, leading to $\hbar\omega_b = \hbar c_l/b = 7.5\,\mu$eV.

for electron-confined phonon interaction via deformation potential (DP) and piezoelectric (PZ) coupling. The interference is influenced by the orientation of the DQD in the phonon cavity. From Eqs. (D.6) and (D.11) follows the orientation dependence for coupling to Lamb modes

$$|\alpha_n(\mathbf{q}_\parallel) - \beta_n(\mathbf{q}_\parallel)|^2 \propto \begin{cases} \left|\mathrm{tcs}\left(\frac{1}{2}q_{l,n}\,d\sin\Theta\right)\left(1 \mp e^{i\mathbf{q}_\parallel\cdot\mathbf{d}}\right)\right|^2 & \text{for DP,} \\ \left|\mathrm{tsc}\left(\frac{1}{2}q_{l/t,n}\,d\sin\Theta\right)\left(1 \pm e^{i\mathbf{q}_\parallel\cdot\mathbf{d}}\right)\right|^2 & \text{for PZ,} \end{cases} \tag{6.24}$$

where the upper (lower) sign, and $\mathrm{tcs}\,x = \cos x$ (or $\sin x$), holds for dilatational (flexural) modes; $\mathrm{tsc}\,x$ follows by exchanging $\sin x$ and $\cos x$. The vector $\mathbf{d}$ connects both dots (see Fig. 6.8), Θ gives the orientation of the dots in the cavity with $\Theta = 0, (\pi/2)$ corresponding to the lateral (vertical) configurations in Fig. 6.1. The different symmetries of the DP and PZ potentials with respect to the mid-plane of the cavity (appendix D) manifest themselves in the $\mathrm{tcs}\,x$ and $\mathrm{tsc}\,x$ terms in Eq. (6.24). For instance, dilatational modes lead to a symmetric DP potential (shown in Fig. 6.2) while inducing an antisymmetric PZ potential.

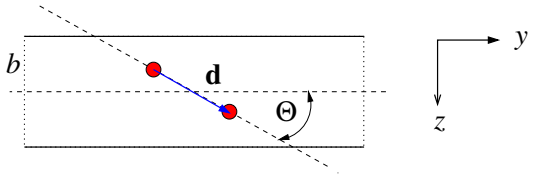

Figure 6.8: Orientation of the quantum dots in the phonon cavity.

In bulk GaAs systems without phonon confinement, PZ interaction normally dominates the coupling to long wavelength acoustic phonons because typical matrix elements relate to the DP coupling as $|V_{\rm pz}/V_{\rm dp}|^2 \propto (e\beta/\Xi)^2 q^{-2}$, with the DP constant Ξ and the PZ modulus β, see chapter 5. Thus, for long wavelength phonons ($q \to 0$) the PZ coupling prevails. In a phonon cavity, however, one can argue that the confinement-induced quantisation of the transverse wave vector gives a lower bound for the wavelength $q_{\rm min} \propto 1/b$. Therefore, for small FSQWs the DP coupling dominates.

We now turn to the discussion of the orientation dependence of the DP induced inelastic current for the examples of lateral and vertical configurations. We start with the vertical configuration ($\Theta = \pi/2$) in which the dot vector is orthogonal to the propagation of the phonons, $\mathbf{q}_{\|} \cdot \mathbf{d} = 0$. Thus, from Eq. (6.24) follows that only flexural modes contribute to the inelastic current through the DQD via DP scattering. This can be understood by a simple symmetry consideration. Dilatational modes induce a symmetrical DP interaction potential (see Fig. 6.2) which affects both dots equally, hence not changing the electron transport. On the other hand, the antisymmetric potential induced by the flexural modes strongly alters the dot levels. A numerical evaluation of Eq. (6.15) leads to the inelastic scattering rate which is shown in Fig. 6.3 (top). In spite of the modifications due to the electron-phonon interaction, the main features of phonon confinement, subband quantisation and van-Hove singularities, clearly remain visible.

On the contrary, for the lateral configuration ($\Theta = 0$), Eq. (6.24) predicts that the effective DOS (6.16) vanishes for flexural modes. Thus, all phonons which are spontaneously emitted from the DQD correspond to dilatational modes. Flexural modes induce an antisymmetric interaction potential (Fig. 6.2) which vanishes at the location of the dots in the mid-plane of the FSQW ($z = 0$). On the other hand, dilatational modes strongly couple to the DQD since they induce a non-zero potential and lead to a phase shift in the renormalisation of the dot levels due to the finite time a phonon needs to propagate from one dot to the next. The calculated inelastic scattering rate for the lateral configuration is shown in Fig. 6.3 (bottom). As for the lateral case, the van-Hove singularities remain visible in the transport.

When comparing the inelastic rates with the thermodynamic DOS, the most obvious difference between the two configurations is seen in the behaviour at the

onset of higher subbands. In the vertical configuration the jumps of the DOS also appear in the inelastic rate whereas for the lateral orientation continuous cusps are seen only. Although the microscopic coupling between electrons and confined phonons is the same in both configurations, the effect on the DQD depends on the orientation. Apart from the modes that lead to van–Hove singularities, the subband minimum is at $\mathbf{q}_{\parallel} = 0$. These modes correspond to non-propagating excitations of the elastic medium which nevertheless lead to displacement patterns with a non-vanishing local change in volume, and thus induce a DP potential. In contrast to the vertical configuration, the lateral setup with both dots in the middle of the cavity ($\Theta = 0$) is not sensitive to non-propagating excitations because the displacement for such modes is constant at the locations of the dots; only propagating modes lead to a finite phase shift in the interaction potentials between the dots and thus affect the transport.

Although being of minor relevance in small FSQWs, the PZ coupling also contributes to the inelastic scattering rate. The orientation dependence and the corresponding decoupling of individual Lamb modes is reversed as compared to the DP case, see Eq. (6.24).

6.2.3 Discussion

From the inelastic rates, which are shown in Fig. 6.3, for the example of DP electron-confined phonon interaction, we can see that in addition to the generic subband quantisation also the van–Hove singularities of the phonon DOS show up in the current through the DQD, acting as clear fingerprints of phonon confinement. Close to the singularity, the application of the perturbative derivation which led to the inelastic rate for weak electron-phonon coupling, Eqs. (6.15) and (6.16), is questionable. However, led by the numerical results for the phonon DOS, we can investigate the influence of the van–Hove singularity in a non-perturbative way by decomposing the phonon spectral density (6.16) to find an approximate analytical model

$$\rho_{\mathrm{eff}}(\omega) = \rho_{\mathrm{Ohm}} + \rho_0\,\delta(\omega - \omega_{\mathrm{v}}), \tag{6.25}$$

consisting of a van–Hove singularity at $\hbar\omega_{\mathrm{v}}$ and a background of lower order subbands which are assumed to form an ohmic bath. Following Ref. [149], the inelastic current at zero temperature can be written as

$$I_{\mathrm{inel}} \approx 2\pi T_c^2 \sum_n w_n\,\delta(\omega - n\omega_{\mathrm{v}}). \tag{6.26}$$

Thus, in addition to the main peak a $\hbar\omega_{\mathrm{v}}$, the van–Hove singularity leads to non-perturbative satellite peaks at harmonics of the frequency ω_{v} with oscillator

strength w_n – similar to DQD systems under monochromatic microwave irradiation [174]. The influence of the ohmic bath background amounts to a power law divergence [149] instead of the former delta-like singularities at energies $n\hbar\omega_{\mathrm{v}}$.

Furthermore, by utilising the orientation dependence which was discussed in the previous section, the DQD can be used as a tuneable energy-selective phonon emitter [147, 148] with well defined emission characteristics because transport is mediated by spontaneous emission. This is particularly interesting in the low energy regime where only the lowest phonon subband contributes to the inelastic scattering rate. For instance, when tuning the energy difference of the DQD levels to $\Delta = (\varepsilon^2 + 4T_c^2)^{1/2} < 1.4\,\hbar\omega_b$ in the lateral configuration only the lowest dilatational mode is accessible via the dominating DP coupling, see Fig. 6.3. Thus, when driving a current through the DQD only phonons belonging to this single mode are emitted from the DQD with energy $\hbar\omega = \Delta$.

As a peculiarity of the planar cavity, for certain energies $\hbar\omega_0$ the dilatational phonons evolve a displacement field $\mathbf{u}(\mathbf{r})$ that does not induce any interaction potential (DP *or* PZ) acting on the electrons. In the single phonon subband regime this corresponds to a *complete decoupling* of dot electrons and cavity phonons, leading to the possibility to suppress phonon induced dephasing in DQD qubit systems. This decoupling manifests in a vanishing inelastic rate which is shown in the inset of Fig. 6.3 for $\omega_0 \approx 1.3\,\omega_b$. At this energy the displacement field is free of divergence and therefore it does not lead to any deformation potential. (Similarly, at $\omega_0 \approx 0.7\,\omega_b$ the displacement field induces no PZ polarisation.)

To estimate a possible experimental realisation we consider a DQD fabricated in a GaAs/GaAlAs heterostructure as in [146]. The cavity has a width $2b = 1\mu$m. The characteristic energy scale for phonon quantum size effects in such a FSQW is $\hbar\omega_b = 7.5\,\mu$eV. This is within the limits of energy resolution of recent electron transport measurements [147, 148], and could even be increased by further reducing the width of the cavity.

The dominant cutoff energy for the contribution of a single phonon subband to the total inelastic scattering rate is connected to the fact that for large wave vectors $q_\parallel$ the phonon induced displacement field in the cavity becomes similar to the field of vertically polarised shear waves, which are equivoluminal excitations of the FSQW and induce no DP interaction potential. This convergence leads to an intrinsic exponential cutoff $\exp(-\omega/\omega_{\mathrm{co}})$ in the contribution of individual phonon subbands to the total inelastic rate [183]. In addition, the finite extension of the electron densities in the dots leads to a reduction of the coupling to short wavelength phonons. This can be easily seen in the form factor (D.7) in appendix D. A Gaussian envelope of the electron density would lead to an exponential cutoff with exponent $\omega_e \approx c_l/l_0$ where l_0 is the width of the density profile. For our configuration we may estimate $\omega_e \approx 10\omega_{\mathrm{co}}$ which means that the intrinsic cutoff ω_{co} is the relevant one.

The energy that limits the current spectrum is given by the source-drain voltage V_{SD} since $\varepsilon = E_L - E_R \leq eV_{SD}$. For $V_{SD} = 140\,\mu$V as in [146], 16 phonon subbands contribute to the current.

Since every real experimental system is finite, we expect structures in the current which were derived for an infinitely extended system to be broadened due the finite area of the cavity A. This broadening should be on an energy scale $\hbar c_l/L$, where $A = L^2$. Thus, for a setup with $c_l/L \approx 0.1\omega_b \approx 1\,\mu$eV ($L \approx 10b$) the broadening is negligible. Finite temperatures yield a similar effect. Since Eq. (6.16) is strictly valid only at $T = 0$, structures in the I–V characteristic should be broadened on a scale of $\hbar\omega \approx k_B T \approx 2\,\mu$eV (at 20 mK). In addition, phonon absorption may become relevant at higher temperatures.

Besides the transport that is mediated by the DP, there is also an influence of the PZ electron-phonon coupling. In a phonon cavity, the PZ effect couples all mode families, shear and Lamb waves, to the dot electrons. Moreover, the anisotropy of the piezo-electric tensor leads to a highly non-trivial $\mathbf{q}_\parallel$ dependence of the matrix elements [176], and thus to anisotropic transport properties. However, this anisotropy is expected to be a minor correction since the PZ coupling yields only a small contribution to the inelastic scattering rate in small FSQWs. From the above arguments we conclude that there is no fundamental obstacle to measure the predicted features of phonon confinement in electron transport.

Recently, the electron transport through a Coulomb blockaded quantum dot in a free-standing 130 nm thick GaAs/AlGaAs membrane was measured [170]. At zero bias, a complete suppression of single-electron tunnelling was found. The authors attributed the associated energy gap in the transport spectrum to the excitation of a localised cavity phonon. The observed energy gap of $\varepsilon_0 \approx 100\,\mu$eV matches reasonably well with the lowest dilatational ($73\,\mu$eV) or flexural ($145\,\mu$eV) van–Hove singularity in the DOS of a 130 nm thick planar cavity. Although, a detailed microscopic explanation of the experimental findings is to our knowledge still missing, this experiment clearly highlights the feasibility to built artificial structures with well controlled electro-mechanical properties.

Chapter 7

Conclusion

In this part we have investigated the non-linear electron transport through a double quantum dot which is placed in a phonon cavity. A free-standing quantum well is used as a model for a nano-size planar phonon cavity. Phonons are quantised lattice vibrations. Therefore, their properties are determined by the acousto-mechanical characteristics of the elastic medium. Mechanical confinement is known to strongly affect the vibrational properties of the system. For instance, confinement leads to a splitting of the phonon spectrum in several subbands, and non-linearities in the dispersion may lead to van–Hove singularities in the phonon density of states by modes with zero phonon group velocity at a finite wavelength.

We show that in the Coulomb–blockade regime, such features of mechanically confined phonons produce clear signatures in the I–V characteristics of the double quantum dot. Therefore, it is a useful tool to detect phonon quantum size effects in the electron-phonon interaction via electron transport measurements.

We find that the coupling to the different phonon mode families of a free-standing quantum well (two families of shear and Lamb waves each) depends on the orientation of the dots with respect to the cavity. This is due to different symmetries of the phonon induced interaction potential and holds for both piezo-electric and deformation potential electron-phonon coupling. For certain orientations, the double dot decouples from all phonon mode families except one. Thus, one can tune the coupling between double dot and phonons by changing the orientation of the dots in the cavity. Since, at low temperatures, the inelastic transport is mediated by spontaneous emission of phonons, double quantum dots can be used as an energy-selective phonon emitter which orientation dependent emission characteristic.

At low energies, which are determined by small splittings of the double quantum dot levels Δ, only the lowest phonon subbands contribute to inelastic scattering and hence to transport through the double dot. For particular values of Δ, deformation potential or piezo-electric scattering is either drastically enhanced

due to phonon van–Hove singularities, or completely suppressed by decoupling the double dot from the phonon environment. The latter decoupling is caused by zeros in the electron-phonon interaction potentials for certain energies rather than gaps in the phonon density of states.

Thus, by tuning the level splitting Δ via gate voltages, one can either control electron dephasing in double dot qubit systems, or strongly increase emission into phonon modes with characteristic angular distribution. Both cases are desirable in a possible future quantum computation setup, where the strong phonon dissipation would allow an accelerated relaxation of the qubit during initialisation. On the other hand, the suppressed coupling to phonons could provide a reasonably long phase coherence time for subsequent quantum gate operations.

Appendices

Appendix A

Jaynes–Cummings model

The Jaynes–Cummings model (JCM) is defined as [32]

$$H_{\mathrm{JC}} = \omega\left(a^{\dagger}a + \frac{1}{2}\right) + \frac{1}{2}\varepsilon\sigma_z + \lambda\left(a\sigma_+ + a^{\dagger}\sigma_-\right), \quad \sigma_{\pm} = \frac{1}{2}(\sigma_x \pm i\sigma_y), \quad \text{(A.1)}$$

consisting of a pseudo-spin with energy splitting ε which is coupled to a harmonic oscillator with characteristic energy ω. The ground state $|\psi_0\rangle = |0\rangle|\downarrow\rangle$ with energy $-\varepsilon/2$ is the only state which is independent on the coupling strength λ. Here, we use the basis of eigenstates of harmonic oscillator $\{|n\rangle\}$ and σ_z $\{|\uparrow\rangle, |\downarrow\rangle\}$. Due to the type of coupling, the system decomposes into a set of subspaces formed by two-level systems which suggests the following ansatz for the excited eigenstates

$$|\psi_n\rangle = \gamma_{\uparrow n}|n,\uparrow\rangle + \gamma_{\downarrow n}|n+1,\downarrow\rangle, \quad n \geq 0. \quad \text{(A.2)}$$

Simple calculation yields

$$\frac{\gamma_{\downarrow n}}{\gamma_{\uparrow n}} = \frac{1}{2\lambda\sqrt{n+1}}\left(\delta \pm \sqrt{\delta^2 - 4\lambda^2(n+1)}\right), \quad \text{(A.3)}$$

with the detuning of pseudo-spin and oscillator mode $\delta = \omega - \varepsilon$. This leads to the eigenstates and eigenenergies

$$|\psi_n^{\pm}\rangle = \cos\theta_n^{\pm}|n,\uparrow\rangle + \sin\theta_n^{\pm}|n+1,\downarrow\rangle, \quad \text{(A.4)}$$

$$E_n^{\pm} = \left(n + \frac{1}{2}\right)\omega \pm \frac{\Delta_n}{2}, \quad \text{(A.5)}$$

with $\Delta_n = [\delta^2 + 4\lambda^2(n+1)]^{1/2}$ and $\tan\theta_n^{\pm} = (\delta \pm \Delta_n)/2\lambda(n+1)^{1/2}$.

If the oscillator mode is strongly detuned from the pseudo-spin splitting, the coupling is only a small perturbation to the eigenstate of the uncoupled system

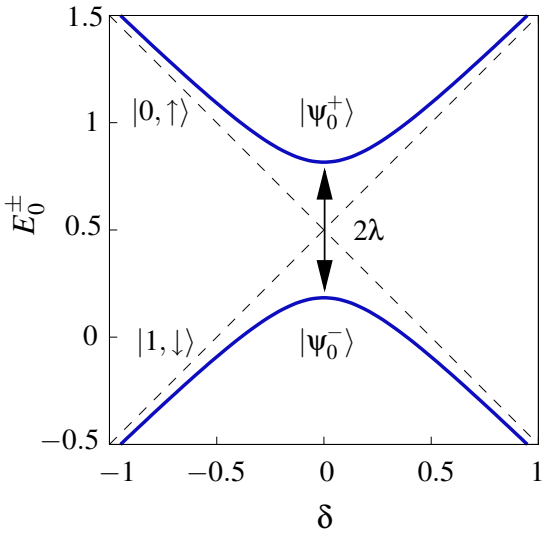

Figure A.1: Eigenenergies of lowest JCM-subspace ($n=0$) as function of detuning δ. Energies in units of ω (dashed lines: eigenenergies for the uncoupled system).

(see Fig. A.1). For the resonant JCM ($\delta=0$) eigenstates are given by the symmetric and (anti-)symmetric superposition

$$|\psi_n^{\pm}\rangle_{\delta=0} = \frac{1}{\sqrt{2}}\big(|n,\uparrow\rangle \pm |n+1,\downarrow\rangle\big). \tag{A.6}$$

Appendix B

Fock–Darwin representation of electron-phonon interaction

For representing the electron-phonon interaction Eq. (3.51),

$$V_{\mathrm{ep}}(\mathbf{q}) = \lambda_{\mathbf{q}}\, e^{i\mathbf{q}\cdot\mathbf{r}}\left(b_{\mathbf{q}} + b^{\dagger}_{-\mathbf{q}}\right),$$

in the Fock–Darwin basis of the quantum dot, we rewrite the coordinate operators in terms of creation and annihilation operators of the $\omega_{\pm}$ fields [see Eq. (3.14)],

$$x = \frac{\tilde{l}}{2}\left(a_- + a_-^{\dagger} + a_+ + a_+^{\dagger}\right), \quad y = \frac{\tilde{l}}{2i}\left(a_- - a_-^{\dagger} - a_+ + a_+^{\dagger}\right). \tag{B.1}$$

It is convenient to introduce complex phonon wave vectors

$$\alpha_{\mathbf{q}}^{+} = \frac{\tilde{l}}{2}(q_y + iq_x), \quad \alpha_{\mathbf{q}}^{-} = -\frac{\tilde{l}}{2}(q_y - iq_x), \tag{B.2}$$

and define *displacement operators*

$$D_{\pm}(\alpha) = e^{\alpha a_{\pm}^{\dagger} - \alpha^{*} a_{\pm}}, \tag{B.3}$$

leading to

$$V_{\mathrm{ep}}(\mathbf{q}) = \lambda_{\mathbf{q}}\, e^{iq_z z} D_+(\alpha_{\mathbf{q}}^{+}) D_-(\alpha_{\mathbf{q}}^{-})\left(b_{\mathbf{q}} + b^{\dagger}_{-\mathbf{q}}\right). \tag{B.4}$$

Thus, the matrix elements for spontaneous emission of a phonon in the Fock–Darwin basis $\{|n_+, n_-, \sigma\rangle\}$ factorise to

$$\langle n'_+, n'_-, \sigma' | V_{\mathrm{ep}}(\mathbf{q}) | n_+, n_-, \sigma\rangle = \delta_{\sigma\sigma'}\lambda_{\mathbf{q}} \langle n'_+ | D_+(\alpha_{\mathbf{q}}^{+}) | n_+\rangle \langle n'_- | D_-(\alpha_{\mathbf{q}}^{-}) | n_-\rangle. \tag{B.5}$$

Here, we have omitted the effect of the operator $\exp(iq_z z)$ because it solely leads to a form factor (basically the Fourier transform of the z-component of the wavefunction). For 2D systems with strong confinement in the growth direction this factor is of order unity.

The matrix elements of the displacement operator with number states of a harmonic oscillator have been derived (see e.g. Eq. (32) in Ref. [184]),

$$\langle n'|D(\alpha)|n\rangle = \sqrt{\frac{n!}{n'!}}\alpha^{n'-n}\,\mathrm{L}_n^{n'-n}\left(|\alpha|^2\right), \quad n' > n, \tag{B.6}$$

with the generalised Laguerre polynomial $\mathrm{L}_\mathrm{n}^\mathrm{m}$. This leads to the matrix elements of the electron-phonon interaction in the Fock–Darwin basis,

$$\begin{aligned}\langle n'_+, n'_-, \sigma'|V_\mathrm{ep}(\mathbf{q})|n_+, n_-, \sigma\rangle = \delta_{\sigma\sigma'}\lambda_\mathbf{q}\sqrt{\frac{n_+!\,n_-!}{n'_+!\,n'_-!}}\left(\alpha_\mathbf{q}^+\right)^{n'_+-n_+}\left(\alpha_\mathbf{q}^-\right)^{n'_--n_-}\\ \times e^{-\frac{1}{2}\left(|\alpha_\mathbf{q}^+|^2+|\alpha_\mathbf{q}^-|^2\right)}\,\mathrm{L}_{n_+}^{n'_+-n_+}\left(|\alpha_\mathbf{q}^+|^2\right)\,\mathrm{L}_{n_-}^{n'_--n_-}\left(|\alpha_\mathbf{q}^-|^2\right).\end{aligned} \tag{B.7}$$

The introduction of displacement operators in Eq. (B.4) provides an illustrative sight on the effect of electron-phonon interaction in the quantum dot. In the Fock–Darwin basis, the scattering with phonons leads to a displacement of the electron wavefunction. The extend of this displacement is determined by the phonon wavelength.

Appendix C

Evaluation of the phonon-induced relaxation rate

In Sec. 3.3.2 the transition rate from the upper to the lower eigenstate of the lowest JCM-subspace was introduced using Fermi's golden rule Eq. (3.58),

$$\Gamma_{\mathrm{ep}} = \frac{\mathcal{V}}{(2\pi)^2\hbar}\int d^3\mathbf{q}\,\left|\langle\Psi_0^+|V_{\mathrm{ep}}(\mathbf{q})|\Psi_0^-\rangle\right|^2\delta(\Delta-\hbar\omega_{\mathbf{q}}), \tag{C.1}$$

leading [by Eq. (3.56) and (3.59)] to

$$\Gamma_{\mathrm{ep}} = \frac{\tilde{l}^4\lambda_{\mathrm{ph}}^2}{16(2\pi)^2\hbar c}\sin^2\theta_+\sin^2\theta_-\int d^3\mathbf{q}\,\frac{q_\parallel^4}{q}\,e^{-\frac{1}{2}(\tilde{l}q_\parallel)^2}\,\delta(\Delta-\hbar cq)\,, \tag{C.2}$$

$$= F\int_0^\infty dq_\parallel\int_0^\infty dq_z\,\frac{q_\parallel^5}{\sqrt{q_\parallel^2+q_z^2}}\,e^{-\frac{1}{2}(\tilde{l}q_\parallel)^2}\,\delta\Big(\Delta-\hbar c\sqrt{q_\parallel^2+q_z^2}\Big)\,, \tag{C.3}$$

$$= \frac{F}{\hbar c}\int_0^{\Delta/\hbar c} dq_\parallel\,\frac{q_\parallel^5}{\sqrt{\left(\frac{\Delta}{\hbar c}\right)^2-q_\parallel^2}}\,e^{-\frac{1}{2}(\tilde{l}q_\parallel)^2}, \tag{C.4}$$

with $F = \sin^2\theta_+\sin^2\theta_-\tilde{l}^4\lambda_{\mathrm{ph}}^2/16\pi\hbar c$. Finally, this can be rewritten as

$$\Gamma_{\mathrm{ep}} = \frac{F}{\hbar c}\left(\frac{\Delta}{\hbar c}\right)^5\int_0^1 dt\,\frac{t^5}{\sqrt{1-t^2}}\,e^{-(\xi t)^2}, \tag{C.5}$$

with the ratio $\xi = 2^{-1/2}\Delta\tilde{l}/\hbar c = 2^{-1/2}(\tilde{l}/l_0)(\Delta/\hbar\omega_s)$, and the time a phonon needs to propagate through the quantum dot $\omega_s^{-1} = l_0/c$. Applying Eq. (3.59) we reach the final result for the phonon induced relaxation rate,

$$\frac{\Gamma_{\mathrm{ep}}}{\omega_0} = \frac{mP}{8\pi(\hbar\omega_s)^2 l_0\rho_{\mathrm{M}}}\,\frac{\sqrt{2}l_0}{\tilde{l}}\sin^2\theta_+\sin^2\theta_-\,\xi^5 I(\xi), \tag{C.6}$$

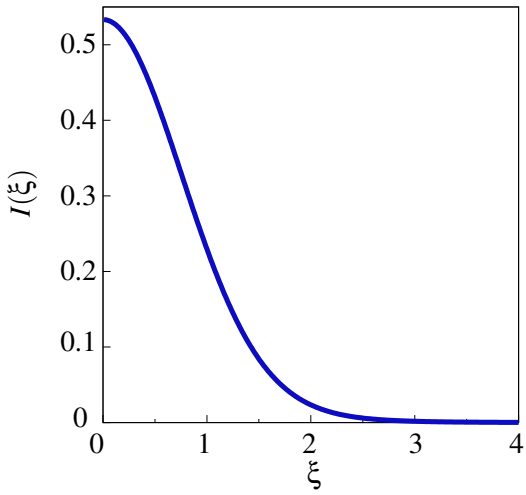

Figure C.1: Numerical evaluation of the integral $I(\xi)$.

with the characteristic frequency $\omega_0 = \hbar/ml_0^2$ and the integral

$$I(\xi) = \int_0^1 dt \frac{t^5}{\sqrt{1-t^2}} e^{-(\xi t)^2}. \tag{C.7}$$

For the numerical evaluation of the integral (C.7) a quickly converging series expression is derived. The integral can be rewritten as

$$I(\xi) = \frac{1}{\xi^4}\frac{\partial^2}{\partial\varepsilon^2} \int_0^1 dt \, \frac{t}{\sqrt{1-t^2}} e^{-\varepsilon(\xi t)^2}\Big|_{\varepsilon\to 1}, \tag{C.8}$$

$$= \frac{1}{\xi^4}\frac{\partial^2}{\partial\varepsilon^2} \left[1 - 2\varepsilon\xi^2 \int_0^1 dt\, t\sqrt{1-t^2} e^{-\varepsilon(\xi t)^2}\right]_{\varepsilon\to 1}, \tag{C.9}$$

by partial integration. Successive N-fold partial integration leads to

$$I(\xi) = \frac{1}{\xi^4}\frac{\partial^2}{\partial\varepsilon^2} \left[\sum_{n=0}^{N} \frac{\left(-2\varepsilon\xi^2\right)^n}{(2n+1)!!} + \frac{\left(-2\varepsilon\xi^2\right)^{N+1}}{(2N+1)!!} \int_0^1 dt\, t(1-t^2)^{N+\frac{1}{2}} e^{-\varepsilon(\xi t)^2}\right]_{\varepsilon\to 1} \tag{C.10}$$

with the double factorial $(2n+1)!! = 1\cdot 3\cdot 5\cdot \ldots \cdot (2n-1)\cdot(2n+1)$. In the limit $N\to\infty$ the last summand in Eq. (C.10) vanishes, leading to

$$I(\xi) = \frac{1}{\xi^4} \sum_{n=2}^{\infty} \frac{n(n-1)}{(2n+1)!!} \left(-2\xi^2\right)^n, \tag{C.11}$$

$$= \frac{\sqrt{\pi}}{2\xi^4} \sum_{n=2}^{\infty} (-1)^n \frac{n(n-1)}{\Gamma\left(n+\frac{3}{2}\right)} \xi^{2n}, \tag{C.12}$$

with the Gamma function Γ. This, for reasonably small ξ, quickly converging result for $I(\xi)$ is shown in Fig. C.1.

Appendix D

Matrix elements of dot electron-confined phonon interaction

Deformation potential coupling

The dominating electron-phonon scattering mechanism in a small free-standing quantum well (FSQW) is the deformation potential (DP) interaction [176] which is proportional to the relative change in volume induced by a deformation of the medium, see Eq. (5.11),

$$V_{\mathrm{def}}(\mathbf{r}) = \Xi \nabla \cdot \mathbf{u}(\mathbf{r}), \tag{D.1}$$

where Ξ is the DP constant. Shear waves do not change the volume of the cavity. Therefore, they do not couple to electrons via DP interaction. Stroscio *et al.* [176] derived the deformation potential for a confined phonon in Lamb mode $(n, \mathbf{q}_{\|})$,

$$V_{\mathrm{def}} = \lambda^{\pm}_{\mathrm{dp}}(q_{\|})\, e^{i\mathbf{q}_{\|}\cdot\mathbf{r}_{\|}}\, \mathrm{tcs}\, q_{l,n} z \, \left[a_n(\mathbf{q}_{\|}) + a_n^{\dagger}(-\mathbf{q}_{\|}) \right], \tag{D.2}$$

where

$$\lambda^{\pm}_{\mathrm{dp}}(q_{\|}) = B^{\mathrm{dp}}_n(q_{\|}) \left(q^2_{t,n} - q^2_{\|} \right) \left(q^2_{l,n} + q^2_{\|} \right) \mathrm{tsc}\, q_{t,n} b \, , \tag{D.3}$$

with $B^{\mathrm{dp}}_n(q_{\|}) = F_n[\hbar \Xi^2 / 2\rho_M \omega_n(q_{\|}) A]^{1/2}$, giving the coupling strength of the DP interaction. The sign $\pm$, and $\mathrm{tsc}\, x = \sin x$ or $\cos x$, correspond to dilatational and flexural Lamb modes, respectively. The density of the elastic medium is given by ρ_M. The FSQW covers an area A which is assumed to be much larger than b^2. Eigenmodes of the displacement field Eq. (6.19) are normalised, leading to the normalisation constants F_n. From Eq. (D.2) the different symmetries of the

induced potential with respect to the confinement direction can be understood as standing waves in the DP interaction potential.

The matrix elements of the interaction with the localised dot states $|L\rangle$ and $|R\rangle$ can be written as

$$\alpha_n(\mathbf{q}_\parallel) = \lambda^{\pm}_{\mathrm{dp}}(q_\parallel) \int d^3\mathbf{r}\, \rho_L(\mathbf{r})\, \mathrm{tcs}\,(q_{l,n} z)\; e^{i\mathbf{q}_\parallel \cdot \mathbf{r}_\parallel}. \tag{D.4}$$

The matrix element $\beta_n(\mathbf{q}_\parallel)$ follows from replacing ρ_L with ρ_R which are the local electron densities in the left and right dot, respectively

$$\rho_i(\mathbf{r}) = \langle i|\Psi^\dagger(\mathbf{r})\Psi(\mathbf{r})|i\rangle. \tag{D.5}$$

Making the assumption that these densities are smooth functions ρ_e centred around the middle of the dots, $\rho_i(\mathbf{r}) \approx \rho_e(\mathbf{r}-\mathbf{r}_i)$, we can calculate the interference term

$$|\alpha_n(\mathbf{q}_\parallel) - \beta_n(\mathbf{q}_\parallel)|^2 = |P_e(\mathbf{q}_\parallel, q_{l,n})|^2 \left|\lambda^{\pm}_{\mathrm{dp}}(q_\parallel)\, \mathrm{tcs}\left(\frac{1}{2} q_{l,n} d \sin\Theta\right)\left(-1 \pm e^{i\mathbf{q}_\parallel \cdot \mathbf{d}}\right)\right|^2 \tag{D.6}$$

The vector $\mathbf{d}$ and the angle Θ are related to the dot orientation in the FSQW (see Fig. 6.8 on page 105), and $P_e(\mathbf{q}_\parallel, q_{l,n})$ is a form factor of the electron density,

$$P_e(\mathbf{q}) = \int d^3\mathbf{r}\, \rho_e(\mathbf{r}) e^{i\mathbf{q}\cdot\mathbf{r}}, \tag{D.7}$$

which can be approximated by unity for sharply localised wavefunctions.

Piezo-electric coupling

The microscopic calculation of the piezo-electric (PZ) potential caused by a confined phonon is more complicated than the previous derivation for the DP case. As seen in chapter 5, the potential V_{pz} is related to the polarisation $\mathbf{P}$, which is induced by the PZ effect, via Poisson's equation $\boldsymbol{\nabla}^2 V_{\mathrm{pz}} = 4\pi e\, \boldsymbol{\nabla}\cdot\mathbf{P}$, see Eq. (5.8).

In general, all four modes families of confined phonons couple to electrons via PZ interaction. A further complication is the anisotropy of the PZ modulus. Stroscio *et al.* [176] calculated the interaction potential for Lamb modes $[n, \mathbf{q}_\parallel = (q_x, q_y)]$ by using an averaged expression for the PZ modulus, leading to

$$V_{\mathrm{pz}}(\mathbf{r}) = \pm q_x q_y q_l \left(\lambda^{\pm}_l(q_\parallel)\, \mathrm{tsc}\, q_l z + \lambda^{\pm}_t(q_\parallel)\, \mathrm{tsc}\, q_t z\right) e^{i\mathbf{q}_\parallel \cdot \mathbf{r}_\parallel} \left[a_n(\mathbf{q}_\parallel) + a^\dagger_n(\mathbf{q}_\parallel)\right] \tag{D.8}$$

with

$$\lambda_l^{\pm}(q_\parallel) = F_n B_n^{\mathrm{pz}}(q_\parallel)\frac{3(q_\parallel^2 - q_t^2)}{q_\parallel^2 + q_l^2}\,\mathrm{tsc}\,q_t b\,, \tag{D.9}$$

$$\lambda_t^{\pm}(q_\parallel) = -F_n B_n^{\mathrm{pz}}(q_\parallel)\frac{2(q_\parallel^2 - 2q_t^2)}{q_\parallel^2 + q_t^2}\,\mathrm{tsc}\,q_l b\,, \tag{D.10}$$

and $B_n^{\mathrm{pz}}(q_\parallel) = (8\pi e\beta/\varepsilon)[\hbar/2A\rho_M\omega_n(q_\parallel)]^{1/2}$. Here ε is the low frequency permittivity constant. The sign $\pm$ and $\mathrm{tsc}\,x$ correspond to dilatational and flexural modes as in the previous section.

When comparing Eqs. (D.8) and (D.2) the different symmetries of the DP and PZ potentials become apparent. The DP potential for dilatational and flexural modes is shown in Fig. 6.2. By extending the calculation of the matrix elements from the previous section to the anisotropic case we find for the interference term

$$\begin{aligned}\left|\alpha_n(\mathbf{q}_\parallel) - \beta_n(\mathbf{q}_\parallel)\right|^2 &= q_x^2 q_y^2 |q_l|^2 \left|\left(1 \pm e^{i\mathbf{q}_\parallel\cdot\mathbf{d}}\right)\right|^2 \\ &\times \left|\left[\lambda_l^{\pm}(q_\parallel)\,\mathrm{tsc}\left(\frac{1}{2}q_l d\sin\Theta\right) + \lambda_t^{\pm}(q_\parallel)\,\mathrm{tsc}\left(\frac{1}{2}q_t d\sin\Theta\right)\right]\right|^2. \end{aligned}\tag{D.11}$$

Bibliography

[1] G. Bergmann, Phys. Rep. **107**, 1 (1984).

[2] D. Y. Sharvin and Y. V. Sharvin, JETP Lett. **34**, 272 (1981).

[3] D. K. Ferry and S. M. Goodnick, in *Transport in nanostructures*, Vol. 6 of *Cambridge Studies in Semiconductor Physics and Microelectronic Engineering*, edited by H. Ahmed, M. Pepper, and A. Broers (Cambridge University Press, Cambridge, 1997).

[4] B. J. van Wees, H. van Houten, C. W. J. Beenakker, J. G. Williamson, L. P. Kouwenhoven, D. van der Marel, and C. T. Foxon, Phys. Rev. Lett. **60**, 848 (1988).

[5] D. A. Wharam, T. J. Thornton, R. Newbury, M. Pepper, H. A. J. E. F. Frost, D. G. Hasko, D. C. Peacock, D. A. Ritchie, and G. A. C. Jones, J. Phys. C: Solid State Phys. **21**, L209 (1988).

[6] Y. Nakamura, Y. A. Pashkin, and J. S. Tsai, Nature **398**, 786 (1999).

[7] T. Hayashi, T. Fujisawa, H. D. Cheong, Y. H. Jeong, and Y. Hirayama, Phys. Rev. Lett. **91**, 226804 (2003).

[8] G. A. Prinz, Physics Today **48**, 58 (1995).

[9] S. A. Wolf, D. D. Awschalom, R. A. Buhrman, J. M. Daughton, S. von Molnár, M. L. Roukes, A. Y. Chtchelkanova, and D. M. Treger, Science **294**, 1488 (2001).

[10] M. N. Baibich, J. M. Broto, A. Fert, F. N. V. Dau, F. Petroff, P. Eitenne, G. Creuzet, A. Friederich, and J. Chazelas, Phys. Rev. Lett. **61**, 2472 (1988).

[11] Y. A. Bychov and E. I. Rashba, JETP Lett. **39**, 78 (1984).

[12] Y. A. Bychov and E. I. Rashba, J. Phys. C **17**, 6039 (1984).

[13] M. Blencowe, Phys. Rep. **395**, 159 (2004).

[14] K. Schwab, E. A. Henriksen, J. M. Worlock, and M. L. Roukes, Nature **404**, 974 (2000).

[15] E. M. Höhberger, T. Krämer, W. Wegscheider, and R. H. Blick, Appl. Phys. Lett. **82**, 4160 (2003).

[16] L. D. Landau and E. M. Lifshitz, *Relativistic quantum theory*, Vol. 4 of *Course of theoretical physics* (Pergamon Press, Oxford, 1971).

[17] J. C. Phillips, *Bonds and bands in semiconductors*, *Materials science and technology* (Academic Press, New York, 1973).

[18] R. Winkler, *Spin-Orbit Coupling Effects in Two-Dimensional Electron and Hole Systems*, Vol. 191 of *Springer Tracts in Modern Physics* (Springer, Berlin, 2003).

[19] T. Ando, A. B. Fowler, and F. Stern, Rev. Mod. Phys. **54**, 437 (1982).

[20] C. Kittel, *Quantum theory of solids* (Wiley, New York, 1963).

[21] G. Dresselhaus, Phys. Rev. **100**, 580 (1955).

[22] W. Kohn, Phys. Rev. **105**, 509 (1957).

[23] G. H. Chen and M. E. Raikh, Phys. Rev. B **60**, 4826 (1999).

[24] J. Nitta, T. Akazaki, H. Takayanagi, and T. Enoki, Phys. Rev. Lett. **78**, 1335 (1997).

[25] T. Koga, J. Nitta, T. Akazaki, and H. Takayanagi, Phys. Rev. Lett. **89**, 046801 (2002).

[26] S. J. Papadakis, E. P. D. Poortere, H. C. Manoharan, M. Shayegan, and R. Winkler, Science **283**, 20556 (1999).

[27] D. Grundler, Phys. Rev. Lett. **84**, 6074 (2000).

[28] W. Shubnikov and W. J. de Haas, Proc. Netherlands Roy. Acad. Sci. **33**, 130 (1930).

[29] S. Hikami, A. I. Larkin, and Y. Nagaoka, Prog. Theor. Phys. **63**, 707 (1980).

[30] B. Das, D. C. Miller, S. Datta, R. Reifenberger, W. P. Hong, P. K. Bhattacharya, J. Singh, and M. Jaffe, Phys. Rev. B **39**, 1411(R) (1989).

[31] M. Pletyukhov and O. Zaitsev, J. Phys. A: Math. Gen. **36**, 5181 (2003).

[32] E. T. Jaynes and F. W. Cummings, Proc. IEEE **51**, 89 (1963).

[33] L. Allen and J. H. Eberly, *Optical Resonance and Two-level Atoms* (Wiley, New York, 1975).

[34] A. Yacoby, H. L. Stormer, N. S. Wingreen, L. N. Pfeiffer, K. W. Baldwin, and K. W. West, Phys. Rev. Lett. **77**, 4612 (1996).

[35] S. Iijima, Nature **354**, 56 (1991).

[36] C. T. White and T. N. Todorov, Nature **393**, 240 (1998).

[37] I. Žutić, J. Fabian, and S. D. Sarma, Rev. Mod. Phys. **76**, 323 (2004), and references therein.

[38] J. C. Egues, G. Burkard, and D. Loss, Phys. Rev. Lett. **89**, 176401 (2002).

[39] E. I. Rashba and A. L. Efros, Phys. Rev. Lett. **91**, 126405 (2003).

[40] E. I. Rashba, Fiz. Tverd. Tela (Leningrad) **2**, 1224 (1960), sov. Phys. Solid **2**, 1109 (1960).

[41] G. Engels, J. Lange, T. Schäpers, and H. Lüth, Phys. Rev. B **55**, 1958(R) (1997).

[42] S. Datta and B. Das, Appl. Phys. Lett. **56**, 665 (1990).

[43] J. Nitta, F. E. Meijer, and H. Takayanagi, Appl. Phys. Lett. **75**, 695 (1999).

[44] X. F. Wang, P. Vasilopoulos, and F. M. Peeters, Appl. Phys. Lett. **80**, 1400 (2002).

[45] X. F. Wang and P. Vasilopoulos, Phys. Rev. B **68**, 035305 (2003).

[46] U. Zülicke, Appl. Phys. Lett. **85**, 2616 (2004).

[47] D. Frustaglia and K. Richter, Phys. Rev. B **69**, 235310 (2004).

[48] E. A. de Andrada e Silva and G. C. L. Rocca, Phys. Rev. B **59**, 15583(R) (1999).

[49] M. Governale, D. Boese, U. Zülicke, and C. Schroll, Phys. Rev. B **65**, 140403(R) (2002).

[50] R. Ionicioiu and I. D'Amico, Phys. Rev. B **67**, 041307(R) (2003).

[51] C. M. Hu and T. Matsuyama, Phys. Rev. Lett. **87**, 066803 (2001).

[52] T. Matsuyama, C.-M. Hu, D. Grundler, G. Meier, and U. Merkt, Phys. Rev. B **65**, 155322 (2002).

[53] M. H. Larsen, A. M. Lunde, and K. Flensberg, Phys. Rev. B **66**, 033304 (2002).

[54] F. Mireles and G. Kirczenow, Phys. Rev. B **66**, 214415 (2002).

[55] M. G. Pala, M. Governale, J. König, U. Zülicke, and G. Iannaccone, Phys. Rev. B **69**, 045304 (2004).

[56] E. N. Bulgakov, K. N. Pichugin, A. F. Sadreev, P. Streda, and P. Seba, Phys. Rev. Lett. **83**, 376 (1999).

[57] A. A. Kiselev and K. W. Kim, Appl. Phys. Lett. **78**, 775 (2001).

[58] A. A. Kiselev and K. W. Kim, Appl. Phys. Lett. **94**, 4001 (2003).

[59] T. P. Pareek, Phys. Rev. Lett. **92**, 076601 (2004).

[60] J. Ohe, M. Yamamoto, T. Ohtsuki, and J. Nitta, cond-mat/0409161. (unpublished).

[61] E. N. Bulgakov and A. F. Sadreev, Phys. Rev. B **66**, 075331 (2002).

[62] M. Governale, F. Taddei, and R. Fazio, Phys. Rev. B **68**, 155324 (2003).

[63] S. A. Tarasenko and N. S. Averkiev, JETP Lett. **75**, 552 (2002).

[64] X. F. Wang and P. Vasilopoulos, Phys. Rev. B **67**, 085313 (2003).

[65] G. Usaj and C. A. Balseiro, Phys. Rev. B **70**, 041301(R) (2004).

[66] F. E. Meijer, A. F. Morpurgo, T. M. Klapwijk, T. Koga, and J. Nitta, cond-mat/0406106. (unpublished).

[67] A. V. Moroz and C. H. W. Barnes, Phys. Rev. B **60**, 14272 (1999).

[68] F. Mireles and G. Kirczenow, Phys. Rev. B **64**, 024426 (2001).

[69] M. Governale and U. Zülicke, Phys. Rev. B **66**, 073311 (2002).

[70] M. Governale and U. Zülicke, Solid State Commun. **131**, 581 (2004).

[71] M. G. Pala, M. Governale, U. Zülicke, and G. Iannaccone, cond-mat/0409580. (unpublished).

[72] T. Schäpers, J. Knobbe, and V. A. Guzenko, Phys. Rev. B **69**, 235323 (2004).

[73] J. Wang, H. B. Sun, and D. Y. Xing, Phys. Rev. B **69**, 085304 (2004).

[74] M. Cahay and S. Bandyopadhyay, Phys. Rev. B **69**, 045303 (2004).

[75] S. Bandyopadhyay, S. Pramanik, and M. Cahay, Superlat. Microstruct. **35**, 67 (2004).

[76] Y. V. Pershin, J. A. Nesteroff, and V. Privman, Phys. Rev. B **69**, 121306(R) (2004).

[77] S. Debald and C. Emary, cond-mat/0410714. (unpublished).

[78] R. Arvieu and P. Rozmej, Phys. Rev. A **50**, 4376 (1994).

[79] R. Arvieu and P. Rozmej, Phys. Rev. A **51**, 104 (1995).

[80] M. Chaichian and R. Hagedorn, *Symmetries in Quantum Mechanics – From Angular Momentum to Supersymmetry* (IOP Publishing, Bristol, 98).

[81] L. I. Glazman, G. B. Lesovik, D. E. Khmel'nitskii, and R. I. Shekter, JETP Lett. **48**, 239 (188).

[82] I. I. Rabi, Phys. Rev. **51**, 652 (1937).

[83] G. D. Mahan, *Many-Particle Physics*, 2 ed. (Plenum Press, New York, 1990).

[84] B. Kramer and A. MacKinnon, Rep. Prog. Phys. **56**, 1469 (1993).

[85] P. F. Bagwell, Phys. Rev. B **41**, 10354 (1990).

[86] H. Tamura and T. Ando, Phys. Rev. B **44**, 1792 (1991).

[87] L. W. Molenkamp, G. Schmidt, and G. E. W. Bauer, Phys. Rev. B **64**, 121202(R) (2001).

[88] E. Betzig and J. K. Trautman, Science **257**, 189 (1992).

[89] C. Girard and A. Dereux, Rep. Prog. Phys. **59**, 657 (1996).

[90] X. F. Wang, P. Vasilopoulos, and F. M. Peeters, Phys. Rev. B **65**, 165217 (2002).

[91] H. A. Carmona, A. K. Geim, A. Nogaret, P. C. Main, T. J. Foster, M. Henini, S. P. Beaumont, and M. G. Blamire, Phys. Rev. Lett. **74**, 3009 (1995).

[92] P. D. Ye, D. Weiss, R. R. Gerhardts, M. Seeger, K. von Klitzing, K. Eberl, and H. Nickel, Phys. Rev. Lett. **74**, 3013 (1995).

[93] R. Landauer, IBM J. Res. Dev. **1**, 223 (1957).

[94] R. Landauer, IBM J. Res. Dev. **32**, 306 (1988).

[95] D. Vion, A. Aassime, A. Cottet, P. Joyez, H. Potier, C. Urbina, D. Esteve, and M. H. Devoret, Science **296**, 886 (2002).

[96] I. Chiorescu, Y. Nakamura, C. J. P. M. Harmans, and J. E. Mooij, Science **299**, 1869 (2004).

[97] J. A. Folk, S. R. Patel, K. M. Birnbaum, C. M. Marcus, C. I. Duruöz, and J. S. Harris, Jr., Phys. Rev. Lett. **86**, 2102 (2001).

[98] B. I. Halperin, A. Stern, Y. Oreg, J. N. H. J. Cremers, J. A. Folk, and C. M. Marcus, Phys. Rev. Lett. **86**, 2106 (2001).

[99] I. L. Aleiner and V. I. Fal'ko, Phys. Rev. Lett. **87**, 256801 (2001).

[100] J. H. Cremers, P. W. Brouwer, and V. I. Fal'ko, Phys. Rev. B **68**, 125329 (2003).

[101] J. Köneman, R. J. Haug, D. K. Maude, V. I. Fal'ko, and B. L. Altshuler, cond-mat/0409054 (unpublished).

[102] T. Chakraborty and P. Pietiläinen, cond-mat/0410248 (unpublished).

[103] R. de Sousa and S. D. Sarma, Phys. Rev. B **68**, 155330 (2003).

[104] O. Voskoboynikov, O. Bauga, C. P. Lee, and O. Tretyak, J. Appl. Phys. **94**, 5891 (2003).

[105] M. Governale, Phys. Rev. Lett. **89**, 206802 (2002).

[106] M. Valín-Rodríguez, A. P. L. Serra, and E. Lipparini, Phys. Rev. B **66**, 235322 (2002).

[107] O. Voskoboynikov, C. P. Lee, and O. Tretyak, Phys. Rev. B **63**, 165306 (2001).

[108] L. P. Kouwenhoven, D. G. Austing, and S. Tarucha, Rep. Prog. Phys. **64**, 701 (2001).

[109] U. Merkt, J. Huser, and M. Wagner, Phys. Rev. B **43**, 7320 (1991).

[110] A. V. Khaetskii and Y. V. Nazarov, Phys. Rev. B **61**, 12639 (2000).

[111] M. Bruus, K. Flensberg, and H. Smith, Phys. Rev. B **48**, 11144 (1993).

[112] M. A. Kastner, Phys. Today **46**, 24 (1993).

[113] R. C. Ashoori, Nature **379**, 413 (1996).

[114] S. Tarucha, D. G. Austing, T. H. R. J. van der Hage, and L. P. Kouwenhoven, Phys. Rev. Lett. **77**, 3613 (1996).

[115] L. P. Kouwenhoven, T. H. Oosterkamp, M. W. S. Danoesastro, M. Eto, D. G. Austing, T. Honda, and S. Tarucha, Science **278**, 1788 (1997).

[116] W. G. van der Wiel, T. H. Oosterkamp, J. W. Janssen, L. P. Kouwenhoven, D. G. Austing, T. Honda, and S. Tarucha, Phyica B **256-258**, 173 (1998).

[117] D. Goldhaber-Gordon, H. Shtrikman, D. Mahalu, D. Abusch-Magder, U. Meirav, and M. A. Kastner, Nature **391**, 156 (1998).

[118] S. M. Cronenwett, T. H. Oosterkamp, and L. P. Kouwenhoven, Science **281**, 540 (1998).

[119] J. Schmid, J. Weis, K. Eberl, and K. v. Klitzing, Physica B **256-258**, 182 (1998).

[120] F. Simmel, R. H. Blick, J. P. Kotthaus, W. Wegscheider, and M. Bichler, Phys. Rev. Lett. **83**, 804 (1999).

[121] T. Tanamoto, Phys. Rev. A **61**, 022305 (2000).

[122] D. Loss and D. P. DiVincenzo, Phys. Rev. A **57**, 120 (1998).

[123] V. Fock, Z. Phys. **47**, 446 (1928).

[124] C. G. Darwin, Proc. Camb. Phil. Soc. **27**, 86 (1930).

[125] L. P. Kouwenhoven, C. M. Marcus, P. L. McEuen, S. Tarucha, R. M. Westervelt, and N. S. Wingreen, in *Mesoscopic electron transport*, Vol. 345 of *NATO ASI Series E*, edited by L. L. Sohn, G. Schön, and L. P. Kouwenhoven (Kluwer, Boston, 1997), Chap. Electron transport in quantum dots, pp. 105–214.

[126] H. Grabert and M. H. Devoret, *Single Charge Tunnelling* (Springer, Berlin, 1991).

[127] T. Chakraborty and P. Pietiläinen, cond-mat/0501642 (unpublished).

[128] T. P. S. III and F. F. Fang, Phys. Rev. B **35**, 7729 (1987).

[129] S. Brosig, K. Ensslin, A. G. Jansen, C. Nguyen, B. Brar, M. Thomas, and H. Kroemer, Phys. Rev. B **61**, 13045 (2000).

[130] M. Abramowitz and I. Stegun, *Handbook of mathematical functions*, 9 ed. (Dover Publications, New York, 1970).

[131] R. Hanson, B. Witkamp, L. M. K. Vandersypen, L. H. W. van Beveren, J. M. Elzerman, and L. P. Kouwenhoven, Phys. Rev. Lett. **91**, 196802 (2003).

[132] B. L. Altshuler, Y. Gefen, A. Kamenov, and L. S. Levitov, Phys. Rev. Lett. **78**, 2803 (1997).

[133] A. V. Khaetskii and Y. Nazarov, Phys. Rev. B **61**, 12639 (2001).

[134] V. N. Golovach, A. Khaetskii, and D. Loss, Phys. Rev. Lett. **93**, 016601 (2004).

[135] Y. B. Lyanda-Geller, I. L. Aleiner, and B. L. Altshuler, Phys. Rev. Lett. **89**, 107602 (2002).

[136] S. I. Erlingsson and Y. V. Nazarov, Phys. Rev. B **64**, 155327 (2002).

[137] A. Khaetskii, D. Loss, and L. Glazman, Phys. Rev. Lett. **88**, 186802 (2002).

[138] D. Frenkel, Phys. Rev. B **43**, 14228 (1991).

[139] V. F. Gantmaker and Y. B. Levinson, in *Carrier scattering in metals and semiconductors*, Vol. 19 of *Modern problems in condensed matter sciences*, edited by V. M. Agranovitch and A. A. Maradudin (North-Holland Physics Publishing, Amsterdam, 1987).

[140] J. D. Zook, Phys. Rev. **136**, A869 (1964).

[141] T. Brandes, *The Dicke Effect in Electronic Systems* (Habilitationsschrift, Universität Hamburg, 2000).

[142] H. Landolt and R. Börnstein, in *Landolt-Börnstein: Zahlenwerke und Funktionen aus Naturwissenschaften und Technik*, Vol. 17 and 18 of *Group III*, edited by O. Madelung (Springer, Berlin, 1985).

[143] L. D. Landau and E. M. Lifschitz, *Course of Theoretical Physics* (Butterworth–Heinemann, Oxford, 1986), Vol. 7.

[144] B. Auld, *Acoustic Fields and Waves* (Wiley, New York, 1973), Vol. 2.

[145] N. C. van der Vaart, S. F. Godjin, Y. V. Nazarov, C. J. P. M. Harmans, J. E. Mooij, L. W. Molenkamp, and C. T. Foxon, Phys. Rev. Lett. **74**, 4702 (1995).

[146] R. H. Blick, D. Pfannkuche, R. J. Haug, K. v. Klitzing, and K. Eberl, Phys. Rev. Lett. **80**, 4032 (1998).

[147] T. Fujisawa, T. Oosterkamp, W. van der Wiel, B. Broer, R. Aguado, S. Tarucha, and L. Kouwenhoven, Science **282**, 932 (1998).

[148] S. Tarucha, T. Fujisawa, K. Ono, D. G. Austin, T. H. Oosterkamp, and W. G. van der Wiel, Microelectr. Engineer. **47**, 101 (1999).

[149] T. Brandes and B. Kramer, Phys. Rev. Lett. **83**, 3021 (1999).

[150] T. S. Tighe, J. M. Worlock, and M. L. Roukes, Appl. Phys. Lett. **70**, 2687 (1997).

[151] D. E. Angelescu, M. C. Cross, and M. L. Roukes, Superlattices and Microstructures **23**, 673 (1998).

[152] R. H. Blick, M. L. Roukes, W. Wegscheider, and M. Bichler, Physica B **249**, 784 (1998).

[153] A. N. Cleland and M. L. Roukes, Nature **392**, 160 (1998).

[154] J. Seyler and M. N. Wybourne, Phys. Rev. Lett. **69**, 1427 (1992).

[155] A. Greiner, L. Reggiani, T. Kuhn, and L. Varani, Phys. Rev. Lett. **78**, 1114 (1997).

[156] L. G. C. Rego and G. Kirczenow, Phys. Rev. Lett. **81**, 232 (1998).

[157] A. Greiner, L. Reggiani, and T. Kuhn, Phys. Rev. Lett. **81**, 5037 (1998).

[158] C. L. Kane and M. P. A. Fisher, Phys. Rev. Lett. **76**, 3192 (1996).

[159] A. Kambili, V. I. Fal'ko, and C. J. Lambert, Phys. Rev. B **60**, 15593 (1999).

[160] T. D. Krauss and F. W. Wise, Phys. Rev. Lett. **79**, 5102 (1998).

[161] M. S. Dresselhaus and P. C. Eklund, Adv. Phys. **49**, 705 (2000).

[162] T. Brandes, Phys. Rep. **408**, 315 (2005).

[163] C. F. Lo and W. H. Wong, Phys. Rev. B **52**, 3333 (1995).

[164] X. Hu and F. Nori, Phys. Rev. Lett. **79**, 4605 (1997).

[165] X. Hu and F. Nori, Physica B **263**, 16 (1999).

[166] M. P. Blencowe and M. N. Wybourne, Physica **280**, 555 (2000).

[167] R. Aguado and L. Kouwenhoven, Phys. Rev. Lett. **84**, 1986 (2000).

[168] R. H. Blick, F. G. Monzon, W. Wegscheider, M. Bichler, F. Stern, and M. L. Roukes, Phys. Rev. B **62**, 17103 (2000).

[169] J. Kirschbaum, E. M. Hhberger, R. H. Blick, W. Wegscheider, and M. Bichler, Appl. Phys. Lett. **81**, 280 (2002).

[170] E. M. Weig, R. H. Blick, T. Brandes, J. Kirschbaum, W. Wegscheider, M. Bichler, and J. P. Kotthaus, Phys. Rev. Lett. **92**, 046804 (2004).

[171] A. J. Leggett, S. Chakravarty, A. T. Dorsey, M. P. A. Fisher, A. Garg, and W. Zwerger, Rev. Mod. Phys. **59**, 1 (1987).

[172] T. Meeker and A. Meitzler, *Physical Acoustics* (Academic, New York, 1964).

[173] G. S. Argawal, *Fundamentals of Cavity Quantum Electrodynamics* (World Scientific, Singapore, 1994).

[174] T. H. Stoof and Y. V. Nazarov, Phys. Rev. B **53**, 1050 (1996).

[175] N. Bannov, V. Aristov, V. Mitin, and M. A. Stroscio, Phys. Rev. B **51**, 9930 (1995).

[176] N. Bannov, V. Mitin, and M. A. Stroscio, Phys. Status Solidi B **183**, 131 (1994).

[177] S. Debald, T. Brandes, and B. Kramer (unpublished).

[178] F. Renzoni and T. Brandes, Phys. Rev. B **64**, 245301 (2001).

[179] J. Schliemann, D. Loss, and A. H. MacDonald, Phys. Rev. B **63**, 085311 (2001).

[180] L. I. Glazman and K. A. Matveev, Sov. Phys. JETP **67**, 1276 (1988).

[181] Y. Nazarov, Physica B **189**, 57 (1993).

[182] A. A. Kiselev, K. W. Kim, and M. A. Stroscio, Phys. Rev. B **59**, 10212 (1999).

[183] S. Debald, *Nichtlinearer Transport durch gekoppelte Quantenpunkte in einer Phononenkavität* (Diplomarbeit, Universität Hamburg, 2000).

[184] T. Brandes and N. Lambert, Phys. Rev. B **67**, 125323 (2003).

Acknowledgements

Finally, I would like to express my gratitude to the people who contributed to the progress of this work.

I am grateful to my supervisor Prof. B. Kramer for the opportunity to write my thesis in his group under excellent conditions. I appreciate various discussions with him and the chance to attend numerous workshops and conferences to present and discuss parts of this work.

I am indebted to PD Dr. Tobias Brandes for his continuous support, excellent guidance, and his hospitality in Manchester. Dr. Till Vorrath I thank for the steady company during lunches, coffee breaks, and other events. I enjoyed many entertaining discussions with him.

I am grateful to Dr. Clive Emary for the fruitful collaboration, his help with proofreading parts of the manuscript, and the Briton's protection. I acknowledge many interesting discussion with Dr. Eva Weig. I also thank Dr. Mathias de Riese for his expertise on symmetries and proofreading parts of the manuscript. Prof. D. Schwanitz I thank for his elucidating words.

I am also thankful to all the members of the I. Institut für Theoretische Physik for the unique atmosphere. In particular, I enjoyed many helpful discussions with PD Dr. Stefan Kettemann, Karel Výborný, Bernhard Wunsch, and Alexander Struck.